NASA Contractor Report 2812

Noise Characteristics of Upper Surface Blown Configurations - Analytical Studies

N. N. Reddy, J. G. Tibbetts, A. P. Pennock,
and C. K. W. Tam

CONTRACT NAS1-13870
JULY 1978

NASA

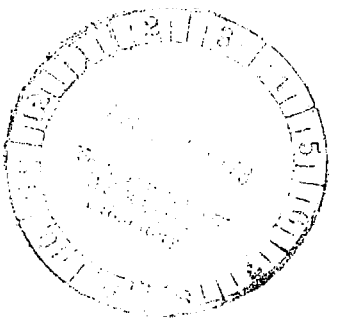

NASA Contractor Report 2812

Noise Characteristics of Upper Surface Blown Configurations - Analytical Studies

N. N. Reddy, J. G. Tibbetts, A. P. Pennock,
and C. K. W. Tam
Lockheed-Georgia Company
Marietta, Georgia

Prepared for
Langley Research Center
under Contract NAS1-13870

National Aeronautics
and Space Administration

**Scientific and Technical
Information Office**

1978

FOREWORD

This report is one of the three reports prepared by the Lockheed-Georgia Company, Marietta, Georgia, for NASA-Langley Research Center under Contract NAS1-13870, "Exploratory Studies of the Noise Characteristics of Upper Surface Blown Configurations." This document represents the analytical studies of the program to understand the noise characteristics of an upper surface blown flap system, and the development of a noise prediction program and aircraft design studies. The other reports under this contract are CR-145143 which covers the detailed experimental program and CR-2918, which is a complete program summary.

CONTENTS

NOISE CHARACTERISTICS OF UPPER SURFACE BLOWN CONFIGURATIONS - ANALYTICAL STUDIES

N. N. Reddy, J. G. Tibbetts, A. P. Pennock, and C. K. W. Tam*
Lockheed-Georgia Co., Marietta, Georgia

SUMMARY

A systematic experimental program was conducted to develop a data base for the far-field noise characteristics of upper surface blown (USB) powered-lift system configurations. The details of the experiments and the data are reported in reference 1. The tests and the data base were oriented towards (1) evaluating the basic noise characteristics of USB, (2) understanding the noise generating mechanisms and identifying the dominant noise source(s), and (3) studying the effect of various geometric and operational parameters on noise.

Spatial and spectral distributions of radiated sound and the flow characteristics from the static model tests were analyzed to determine the noise generating mechanisms of USB. These results and physical arguments suggested that a dominant noise source is located just downstream of the trailing edge where the velocity gradient is large. This noise source is particularly important for the noise radiated in the direction below the wing.

The experimental data from the static tests were used in deriving an empirical noise prediction model. The magnitude and spectral distribution of noise were normalized using various parameters. The spectral distribution is a function of flow length, jet exit velocity and flap angle. The noise level is a function of jet exit velocity, nozzle area, nozzle aspect ratio, flow length and hydraulic diameter. The effect of nozzle shape is incorporated in hydraulic diameter. It was found that the primary variables controlling

---

*Professor of Mathematics, Florida State University; Consultant to Lockheed

far-field noise were the nozzle exit area, jet exit velocity and the flow path length. The influence of other parameters such as flap angle and nozzle shape were generally small. The effects of individual geometric and operational parameters on noise characteristics are discussed in detail in reference 1.

The jet velocity exponent and the spectral distribution of the radiated noise were found to vary with the direction of propagation. The static test results were used in the empirical derivation of these directivities. Flight effects are included in the prediction as correction factors. Thus, this noise prediction model can be used to calculate one-third octave band sound pressure levels at any location, knowing the geometric and operational variables of an aircraft. The calculated results from this prediction method were compared with other experimental data.

USB aircraft compatibility studies were conducted (based on aircraft designs developed in the recent NASA short-haul studies) with the following basic goals: (1) cruise drag competitive with that of conventional installations, (2) satisfactory short-field characteristics, and (3) a 90 EPNdB noise footprint area of 2.59 km^2. The cruise performance data base developed under a separate parallel contract (NAS1-13871) and the noise prediction procedure described in this report were used in the compatibility studies. Effects of various feasible geometric and operational variables on aircraft noise were investigated. From these studies, a final modified design aircraft was selected and the noise characteristics of this final design were calculated.

A theory was developed for the noise from the trailing edge wake (shear layer). This theory, along with the measured turbulence characteristics were used in calculating the radiated noise for one USB model configuration and compared with the experimentally obtained far-field sound. Favorable agreement was found between the theory and experimental results.

1. INTRODUCTION

The operations of short takeoff and landing (STOL) or short haul aircraft impose several environmental problems, of which an important one is community noise. The additional lift augmentation required for the operation of STOL aircraft is generally obtained with an integrated powered-lift system. The noise generated by powered-lift systems is greater than that of the propulsion system used for a conventional takeoff and landing (CTOL) aircraft of the same size.

The upper surface blown flap (USB) is one of the integrated powered-lift concepts being considered for STOL aircraft. In this concept, the jet exhaust is discharged on the upper surfaces of the wing and is turned over the deflected flaps by the Coanda principle. Since the jet exhaust is discharged on the upper surface of the wing, some of the high frequency engine internal noise propagating through the jet exhaust is shielded by the wing and flap surfaces from the community. There are two basic exhaust flow noise generating mechanisms for this type of configuration: (1) the process of the turbulent jet flow mixing with the ambient air and (2) the turbulent jet flow interacting with the rigid surfaces. These noise sources may be further divided based on the geometric location of the source, e.g., the flow mixing noise generated between the nozzle exhaust and the trailing edge and the flow mixing noise generated downstream of the trailing edge. Similarly, the turbulent flow on the surface between the nozzle exit and the trailing edge generates fluctuating pressures on the surface which in turn may generate noise, and the turbulent flow interacting with the trailing edge may also either generate noise or modify the sound field.

Test results reported in references 2-9 were used previously in developing scaling laws and estimating USB noise levels. The results were also helpful in evaluating the feasibility of the USB concept for STOL aircraft from a noise point of view. The noise data obtained from these tests were also used in reference 10 to develop an empirical model to predict noise levels. The effects of some of the geometric parameters on USB noise reported in references 11-14 indicated that there are three dominant noise

sources, viz. fluctuating lift noise, trailing edge noise, and redirected jet mixing noise. However, the flow characteristics and the far-field sound measurements reported in references 15-18 indicated that the noise generated in the vicinity of the trailing edge is dominating from the community standpoint (i.e. radiating below the wing). Consequently, the current program emphasized the investigation of trailing edge related noise, as described in detail in Section 2.

The state of the art is not advanced enough to be able to develop a purely theoretical noise prediction scheme for USB systems. Thus, it is necessary to resort to empirical techniques. In the present study, therefore, systematic experiments were conducted to evaluate the effects of various geometric and operational parameters on USB noise characteristics (ref. 1). An empirical method to calculate USB noise at any point on the ground was then formulated using the acoustic and flow data from the static tests and is described in Section 3. This noise prediction program utilizes various pertinent USB geometric and operational variables. Favorable comparisons were made between the predicted results and the available static test data. A computer program was also developed to predict ground noise contours or footprints. These methods were then applied in a compatibility study of USB aircraft as discussed in Section 4.

Flow visualizations and mean flow velocity and turbulence intensity measurements reported in reference 1 indicated that the predominant noise contributing to the radiated sound field below the wing is generated in the shear layer just downstream of the trailing edge. Therefore, a theory was developed for the radiated sound field generated in the highly sheared flow of the trailing edge wake with particular emphasis on understanding the fundamental noise generating process and on identifying the relevant flow parameters. This theory, which utilizes the measured flow properties in the shear layer, is presented in Section 5.

2. NOISE MECHANISMS

The acoustic and flow characteristics of USB configurations were measured using scaled models in four different ground-based test facilities. The four facilities were: (1) the anechoic room, (2) the acoustics and performance test facility located outdoors, (3) the acoustic open-jet wind tunnel (free-jet facility), and (4) aeroacoustic flow facility. The scaled models with 20.25 and 10.125 cm^2 of nozzle exit areas were used in the acoustic room, acoustic free-jet facility, and aeroacoustic flow facility. Models with 113.8 cm^2 of nozzle exit area with appropriate wing and flaps were used in the acoustic and performance test facility. A schematic diagram of the experimental configuration used in these tests is shown in figure 1. The longitudinal location of the nozzle on the wing, nozzle angle, the radius of curvature, flap angle, and the length of the straight portion of the flap trailing edge were varied. In addition, different nozzle exit shapes — circular, rectangular with width-to-height ratio (aspect ratio) of 2, 4 and 8, elliptic, and D — were used in these experimental investigations. The detailed description of the facilities, the models, the experimental procedures and the acoustic and flow data are presented in reference 1. In this section, the general characteristics of far-field sound and the flow fields are derived from the experimental data in order to identify the noise source mechanisms and delineate the relative importance of each source.

The acoustic results used in this section were obtained for a USB configuration with a rectangular nozzle (aspect ratio 4), wing and flap with 7.62 cm radius of curvature, flap angle of 30° and 0°, and flow length of 21.8 and 22.1 cm. Flow length is defined as the length between the nozzle exit and the trailing edge measured along the surface. Figures 2 through 6 illustrate the radiated sound spectral distribution in various directions in the plane perpendicular to the wing surface and passing through the jet axis. The sound spectra shown in figure 2 were obtained below the wing. It may be seen in this figure that SPL increases at 12 dB/octave (based on third octave band spectra) in the low frequency range. This low frequency variation is equivalent of the mean square sound pressure being proportional to frequency raised to the power 3 ($\bar{p}^2 \sim f^3$). In the high frequency range, SPL decreases at a rate

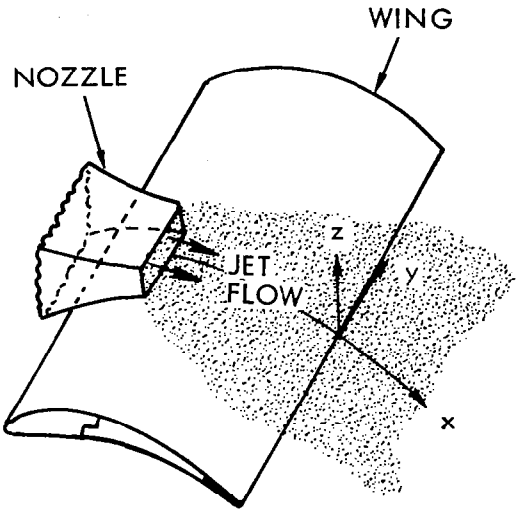

(a) COORDINATE SYSTEM USED IN FLOW AND TURBULENCE MEASUREMENTS

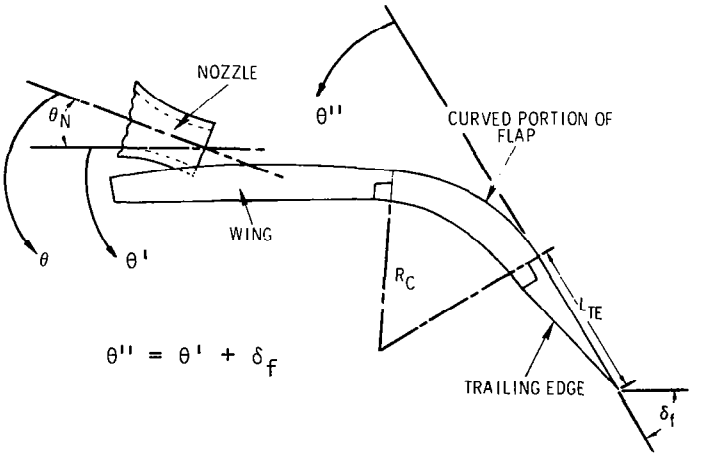

(b) SCHEMATIC DIAGRAM OF EXPERIMENTAL MODEL

FIGURE 1. UPPER SURFACE BLOWN FLAP CONFIGURATION

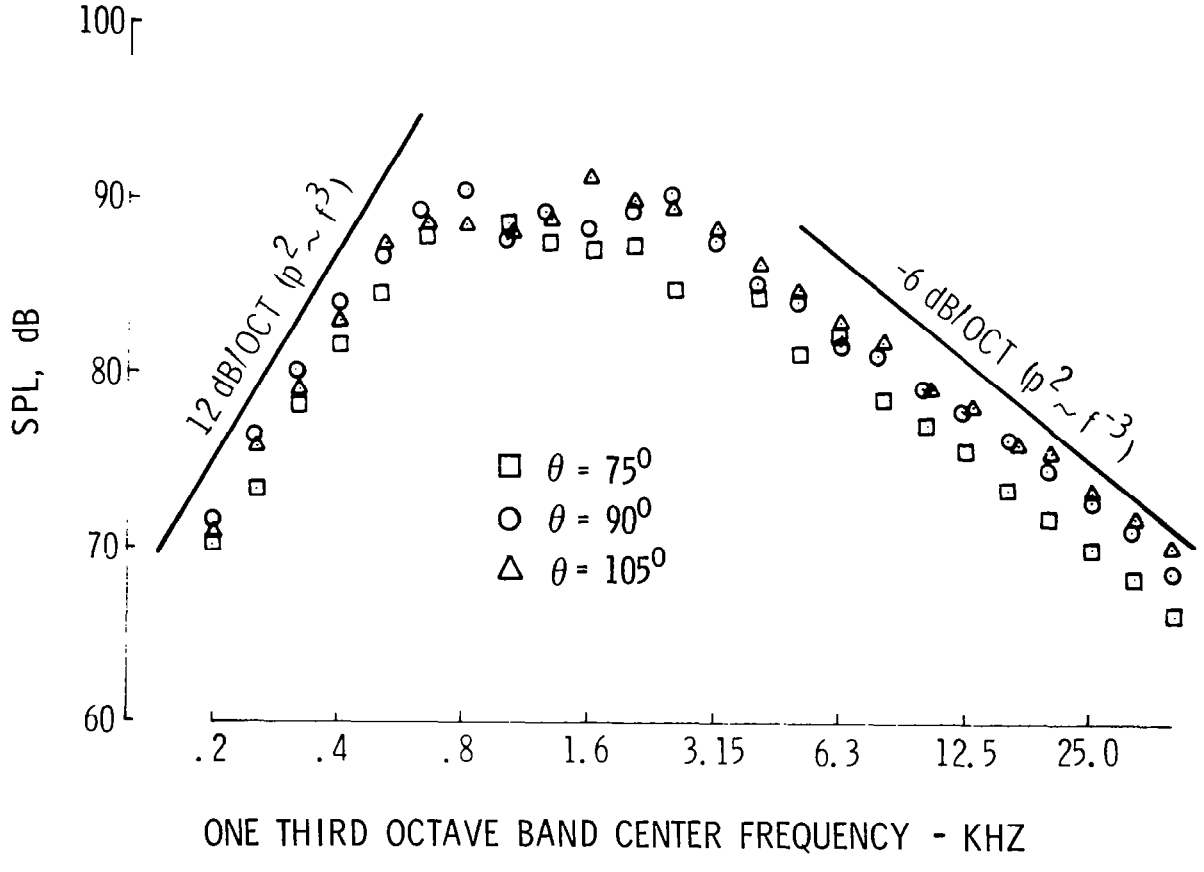

FIGURE 2. SPECTRAL DISTRIBUTION BELOW THE WING

(V_J = 215 m/s, δ_f = 30°, L_F = 21.8 cm

θ_N = 20°, AR_N = 4, R_c = 7.62 cm)

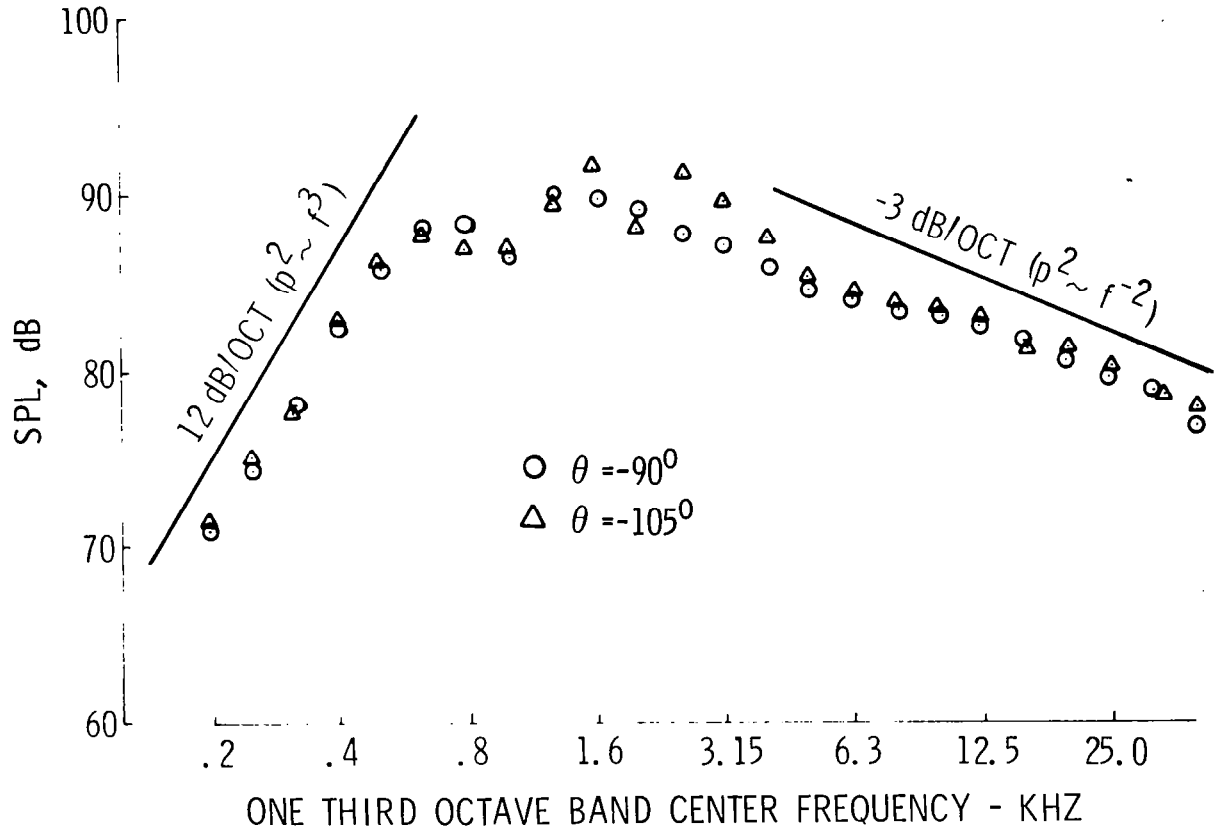

FIGURE 3. SPECTRAL DISTRIBUTION ABOVE THE WING
(V_J = 215 m/s, $\delta_f = 30^\circ$, L_F = 21.8 cm
$\theta_N = 20^\circ$, $AR_N = 4$, R_c = 7.62 cm)

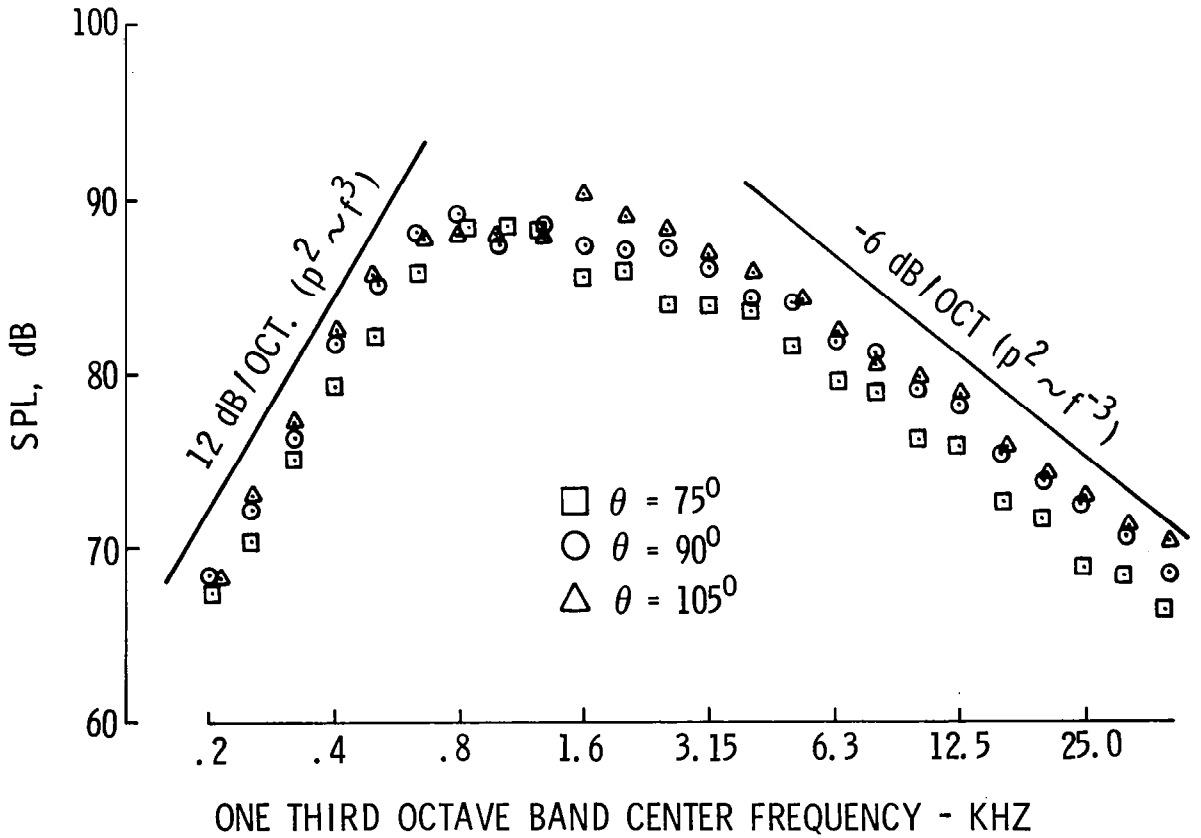

FIGURE 4. SPECTRAL DISTRIBUTION BELOW THE WING
(V_J = 215 m/s, $\delta_f = 0^\circ$, L_F = 22.1 cm
$\theta_N = 20^\circ$, AR_N = 4)

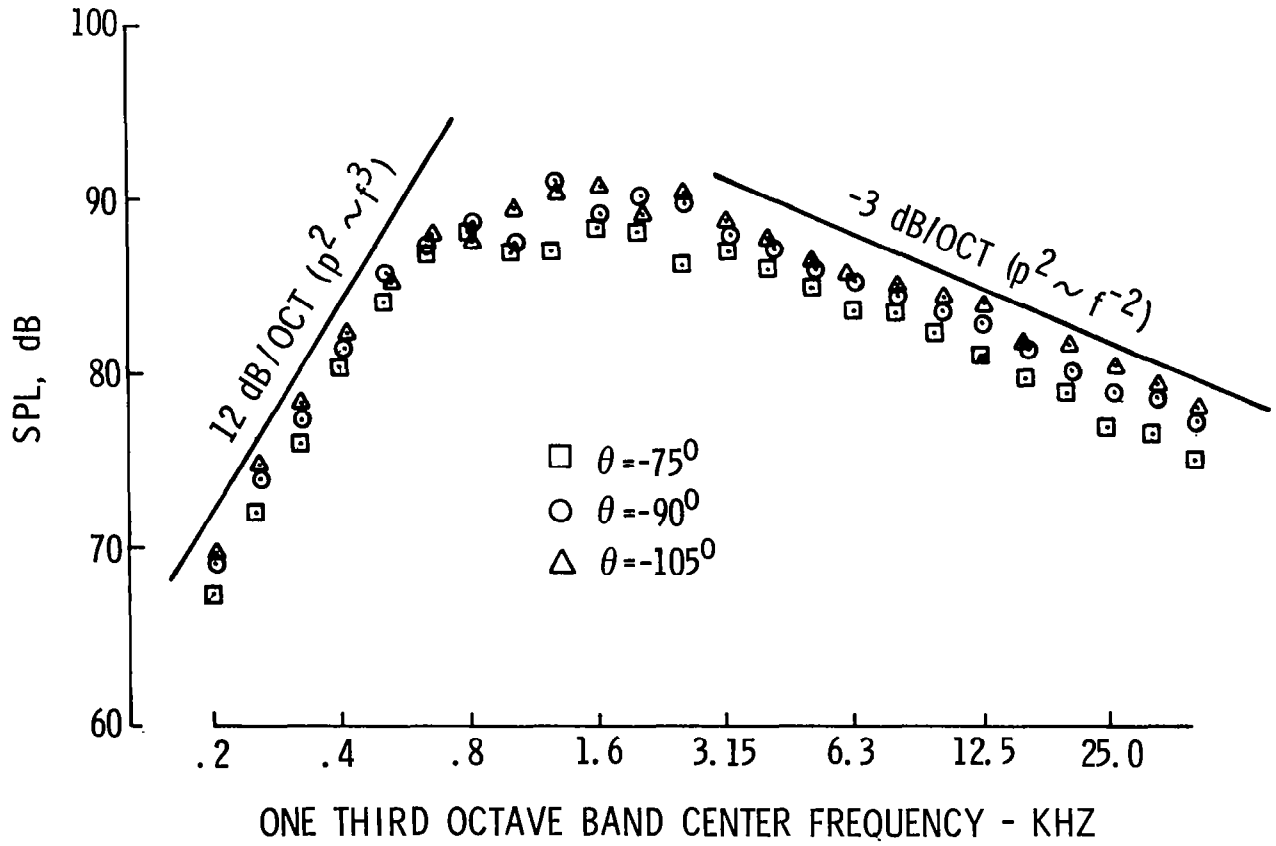

FIGURE 5. SPECTRAL DISTRIBUTION ABOVE THE WING
(V_J = 215 m/s, $\delta_f = 0°$, L_F = 22.1 cm
$\theta_N = 20°$, $AR_N = 4$)

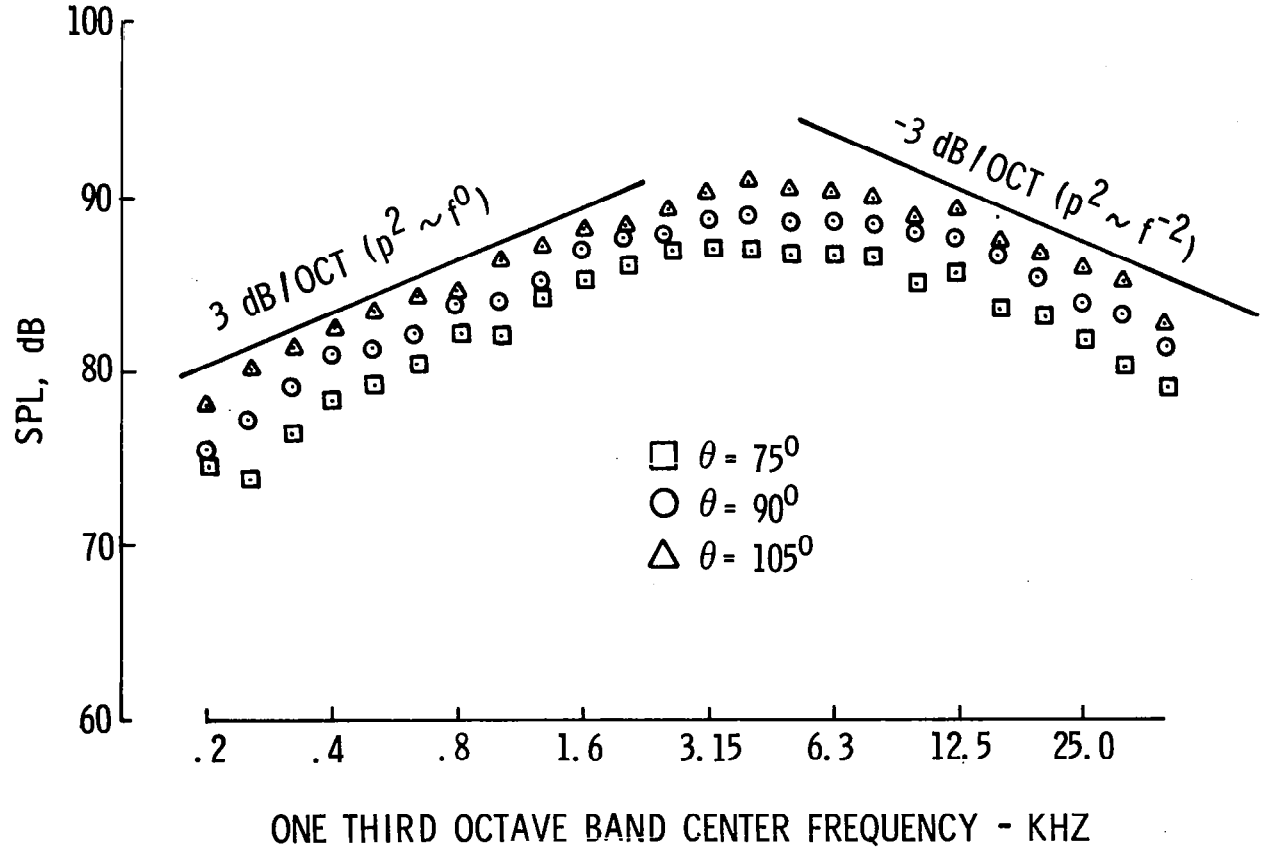

FIGURE 6. SPECTRAL DISTRIBUTION OF JET ALONE
(V_J = 215 m/s, AR_N = 4)

of 6 dB/octave (based on the third octave band spectra) which is equivalent to $\bar{p}^2 \sim f^{-3}$. Figure 3 shows one-third octave band spectra for the same configuration in the direction above the wing and indicates that the low frequency sound pressure increases at the same rate as below the wing ($\bar{p}^2 \sim f^3$) and the high frequency sound decreases as f^{-2}. Comparing these results with that given in figure 2, it may be observed that the variation of sound with frequency in the low frequency range is the same both above and below the wing. In the high frequency range, however, the variation with frequency is different in both directions. Figures 4 and 5 are the spectra below and above the wing, respectively, for a configuration with 0° flap angle. These results are similar to those shown in figures 2 and 3.

The spectral distribution of sound from a free jet (without wing/flap) is shown in figure 6. These results indicate that the SPL variation of 3 dB/octave increase and 3 dB/octave decrease in the low and high frequency ranges, respectively. Comparison of these free jet results with that of a typical spectra of USB shown in figures 2-5, indicates that the high frequency characteristics of sound in the direction above the wing are the same as that of a jet alone. High frequency characteristics of USB noise below the wing, however, are appreciably different from that of the free jet alone. The low frequency noise characteristics of USB are similar both above and below the wing; but different from that of a jet alone. Thus, it may be conjectured that the high-frequency sound radiating above the wing is generated from the area upstream of the flap trailing edge, and is similar to that of a free jet. The low-frequency noise radiating both above and below the wing is from the vicinity of or downstream of the trailing edge. In addition, the high frequency noise radiating below the wing is not similar to any other known noise source and therefore it is assumed to be from the vicinity of the trailing edge.

Figure 7 illustrates the variation of OASPL with the jet exit velocity above and below the wing. It is evident that the sound intensity varies as velocity raised to the power 5.5 in both directions, even though the magnitude is slightly higher above the wing.

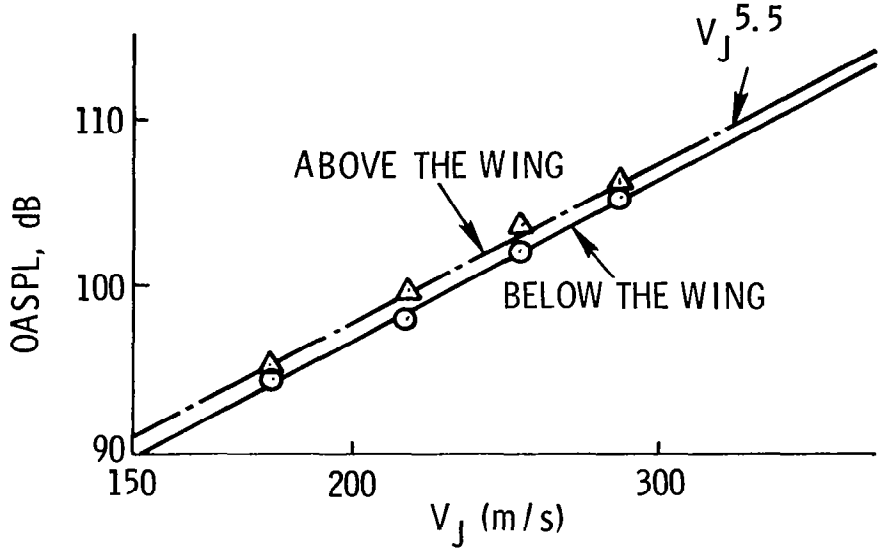

FIGURE 7. VARIATION OF OASPL WITH JET EXIT VELOCITY

($AR_N = 4, \theta_N = 20^\circ$, $L_F = 21.8$ cm, $R_c = 7.62$ cm, $\delta_f = 30^\circ$)

Figures 8 and 9 illustrate the spectral distribution in different directions (in the x-z plane) for flap angles of 30° and 0°, respectively. These results indicate that the sound levels — particularly in the high frequency range increased as the angle θ' from the forward axis of the wing plane increased. As the direction above the flap surface is approached (i.e. $\theta' > 150°$) the sound levels further increase and then decrease with the increase in θ'.

The general flow field of a jet exhaust of a practical USB configuration is shown in figure 10. The flow may be divided into several regions, depending on the geometry and the typical flow properties; for example, the mixing layer between the jet exit and the trailing edge, with a possible potential core close to the nozzle, the wall-jet boundary layer and the trailing edge wake. The flow measurements and the flow visualizations indicate that the characteristics (mean and fluctuating velocities) in the mixing layer are very similar to those of a free jet. Thus, it may be expected that the noise generated in this region is similar to that of a free jet. Also, it may be argued that the high frequency noise is generated close to the nozzle, where the length scale of turbulence is small, and the low frequency noise is generated downstream where the length scale is large. The geometric location of this noise is such that most of the sound would be reflected by the wing and flap surfaces and radiated above the wing. In the wall-jet boundary layer region, the entrainment of free air is inhibited by the presence of the wing and flap surfaces. Therefore, the velocity fluctuations produced by the mixing process are small compared to that in the upper free-mixing layer. The fluctuating pressures on the surface, however, need not be small, because the surface is under a strong influence of the pressure field by the upper free-mixing layer, especially when the jet thickness is small. In fact, the measurements reported in reference 20 show that the surface fluctuating pressures of a radial wall jet were many times more intense than that of a wind tunnel boundary layer or an aerofoil in a uniform stream. This fact perhaps led some investigators to consider the wall-jet boundary layer noise of blown flaps as a potentially important noise source, which is commonly known as "scrubbing noise." But the arguments presented earlier in this section suggest that the noise generated in the boundary layer region of the

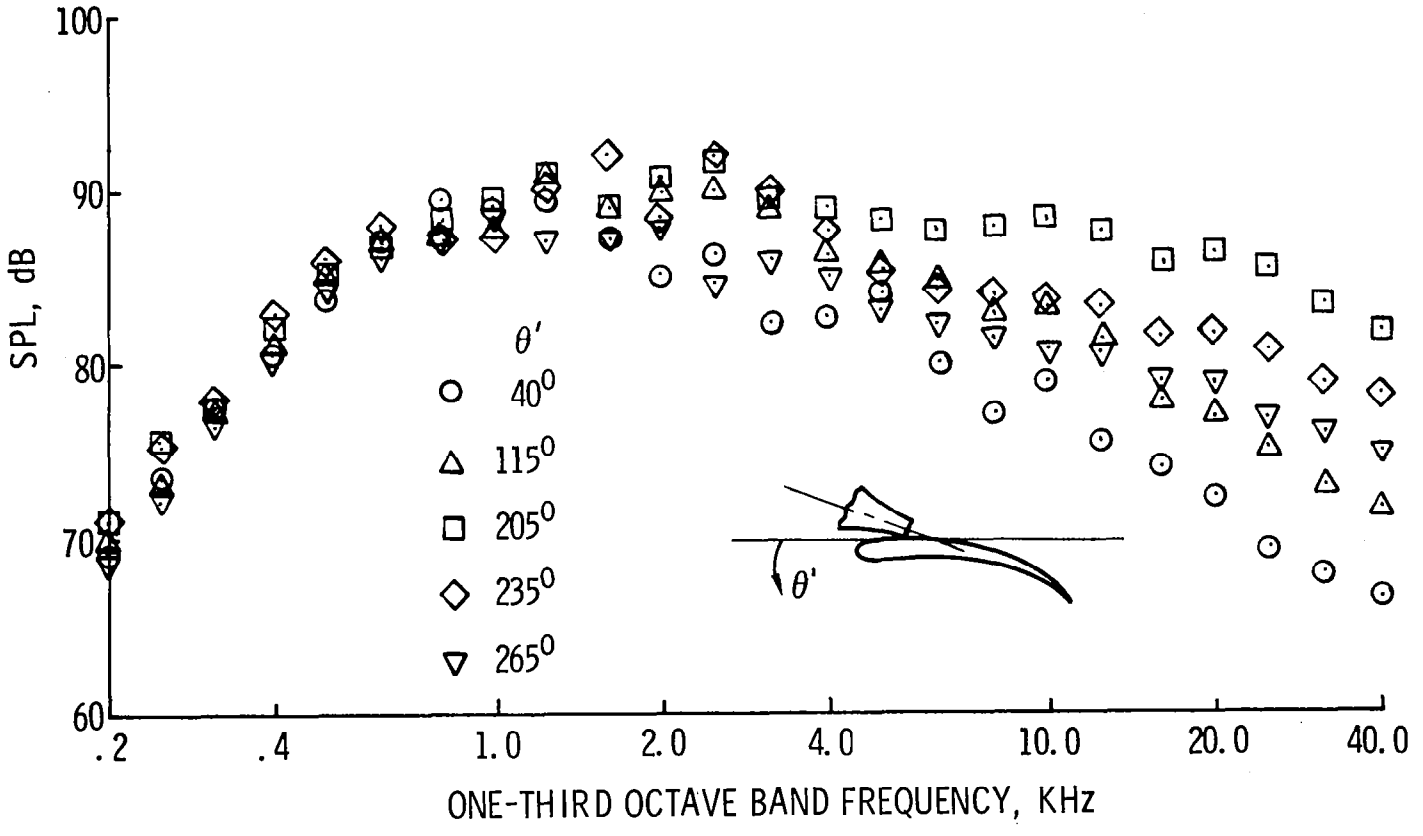

FIGURE 8. TYPICAL DIRECTIVITY DISTRIBUTION OF SOUND SPECTRA

($\delta_f = 30°$, $V_J = 215$ m/Sec, $\theta_N = 20°$, $AR_N = 4$, $L_F = 21.8$ cm, $R_c = 7.26$ cm)

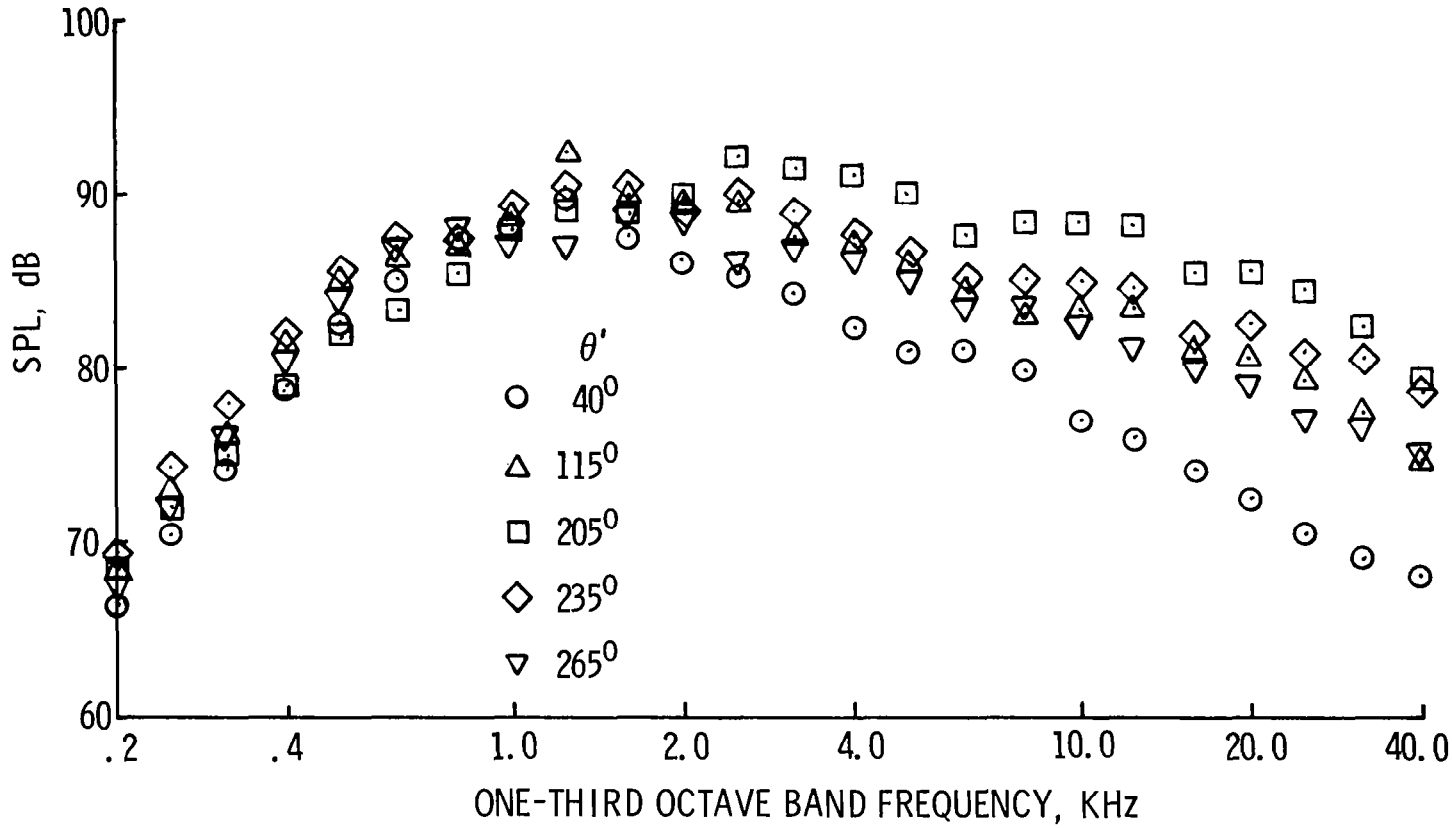

FIGURE 9. TYPICAL DIRECTIVITY DISTRIBUTION OF SOUND SPECTRA

($\delta_f = 0^\circ$, $V_J = 215$ m/Sec, $\theta_N = 20^\circ$, $AR_N = 4$, $L_F = 22.1$ cm)

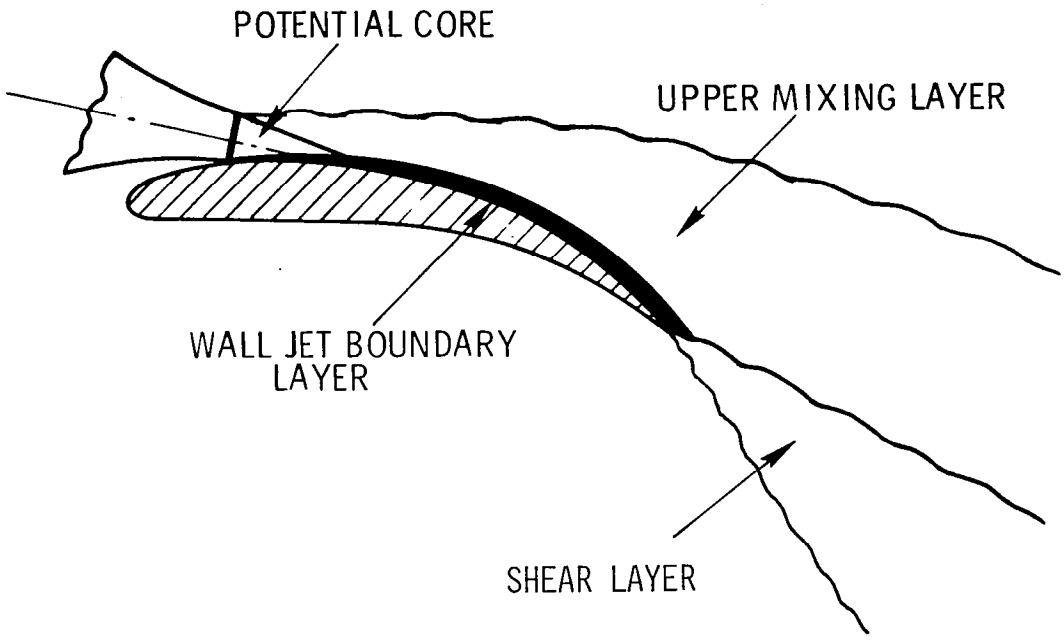

FIGURE 10. MAIN FEATURES OF THE FLOW FIELD OF USB CONFIGURATION

USB is negligible as compared to the other sources. In the trailing edge wake, which is downstream of the trailing edge, the sudden removal of the rigid surface constraint causes a large transverse velocity gradient and a new mixing process with an intense turbulence production. Further downstream, the trailing edge wake and the upper free-mixing layer will combine to form a fully developed flow. The noise generated by this turbulence and velocity gradient could be quite intense and can radiate equally above and below the wing.

The USB noise radiated below the wing typically exhibits peaks and valleys in the spectra as illustrated in figure 11. This type of spectral distribution led some investigators to speculate that there are two sources which could be distinguished by spectral peaks — one with low frequency dominance and the other with high frequency dominance (e.g. references 11-14). In fact, during the early stages of this study the present investigators also believed that the sources could be distinguished by the peaks of the spectra. However, closer examination of the experimental rig and the model configuration revealed that reflection and refraction effects of the rigid surfaces of the test setup could cause the reinforcement and cancellation of radiated sound at certain frequencies. These possibilities were explored experimentally by using sound absorbent material on several of the rigid surfaces. The power spectra of radiated sound, with and without sound absorbent material on the nozzle flange and other reflecting surfaces of the test rig, are shown in figure 12. The reinforcement and cancellations in the mid-frequencies were eliminated with the use of sound absorbent material. The preliminary conclusion from this simple test is that the reinforcement and cancellation of the sound intensities may be due to the presence of the rigid surfaces. But to confirm these results, more analytical and experimental investigations should be conducted. However, it is tentatively concluded that the USB noise generation (without reflection and refraction) is of the broadband type.

From the past discussion, it is hypothesized that the predominant portion of the low frequency noise radiating both above and below the wing and the high frequency noise radiating below the wing is generated in the vicinity of the trailing edge. The high frequency noise radiating in the direction above the wing is perhaps generated by the mixing process of the jet exhaust upstream

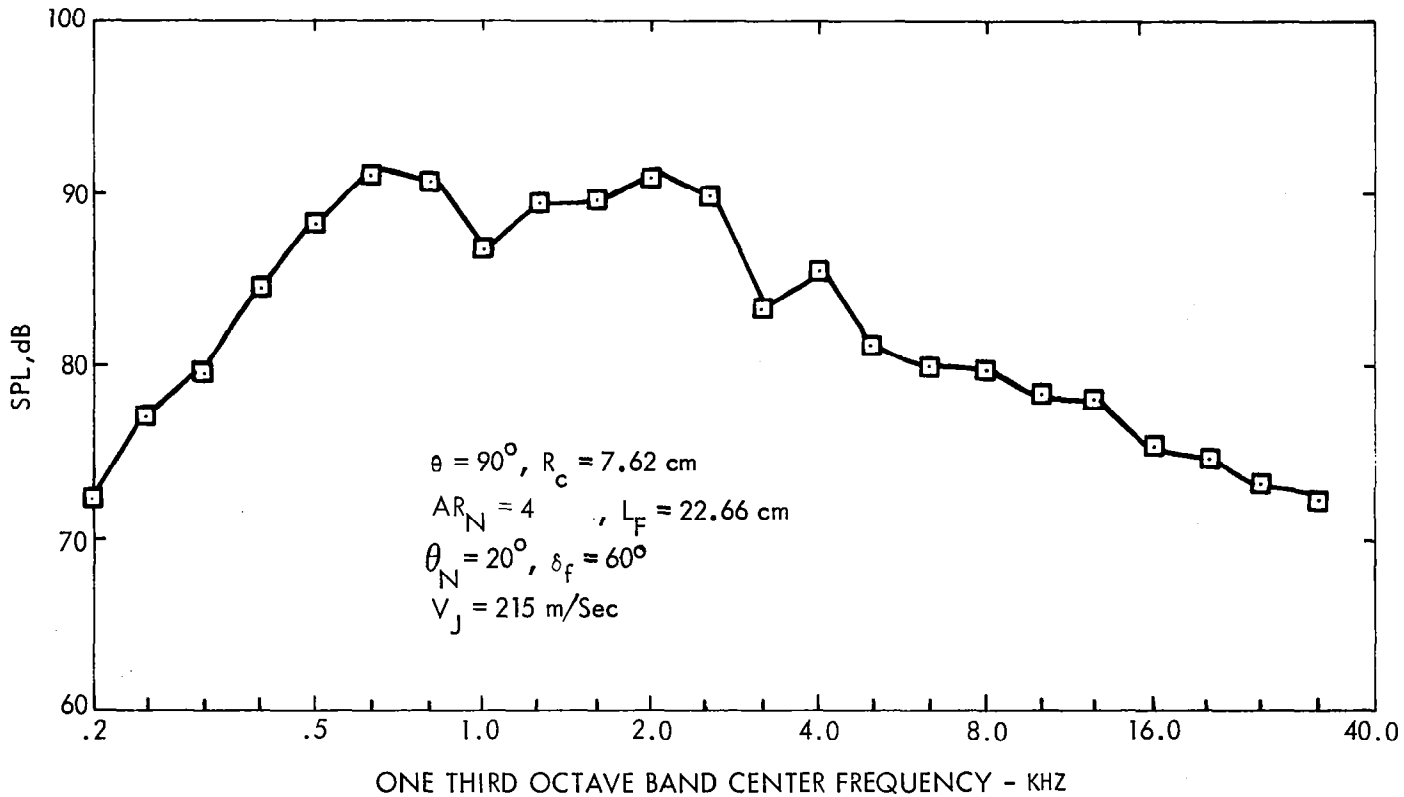

FIGURE 11. TYPICAL SOUND SPECTRA OF USB (BELOW THE WING)

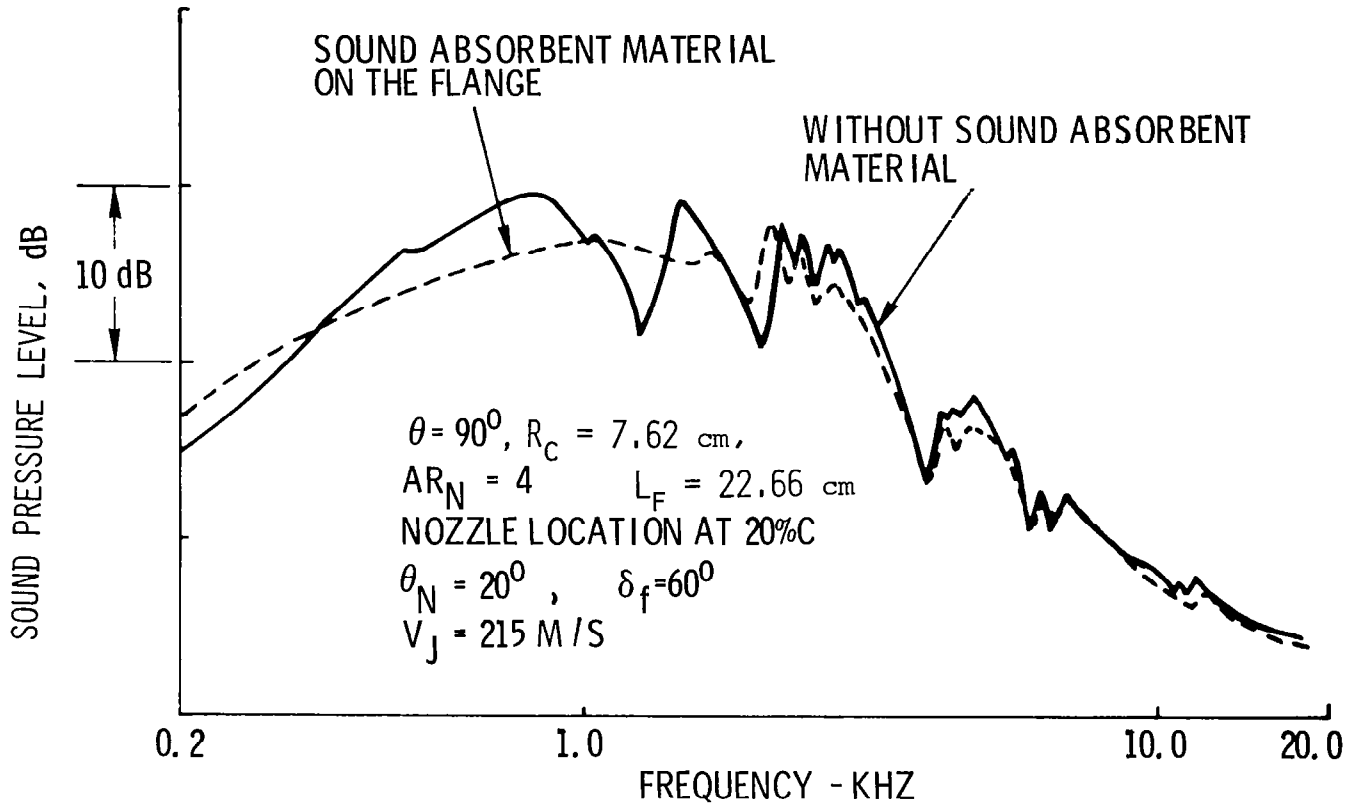

FIGURE 12. EFFECT OF REFRACTION BY EXPERIMENTAL RIG

of the trailing edge. Thus, in order to understand the characteristics of noise which can radiate towards the community, it is necessary to study the noise generation mechanism of the trailing edge wake flow.

A number of theories have been proposed on the noise generation of so-called "trailing edge noise." In references 21 and 22, theories were developed for the scattering of quadrupole noise sources in the vicinity of a trailing edge. In reference 23, it is assumed that the dipole type of noise was generated at the trailing edge for the turbulent flow leaving the trailing edge. In references 24-26, a theory is proposed in which noise is produced by the diffraction of downstream propagating evanescent waves at the trailing edge. The basic assumption of all these theories is that disturbances, regardless whether they are quadrupole or evanescent waves when flowing past the trailing edge, must adjust themselves to the sudden change in environment. During the process of adjustment, pressure disturbances are invariably released giving rise to acoustic radiation. However, the important question is whether this is the dominant source. The turbulent boundary layer of the wall-jet is rather thin at the trailing edge and the turbulence intensity is small compared to the intensity downstream of the trailing edge as shown in the previous experiment (ref. 17). Therefore, the disturbances convected past the trailing edge are not as important as were emphasized in these theories. With regard to the flow in the trailing edge wake, figure 13 illustrates the typical mean velocity and turbulence intensity profiles just downstream of the trailing edge in the mid-span plane. The mean velocity profile has a broad maximum and a large velocity gradient on the bottom side (close to the surface). Similar results were reported in references 17 and 27. The turbulence level shown in figure 13 is quite large over a substantial portion of the wake thickness. Since the velocity gradient is small away from the shear layer, the turbulence is not generated at this location; instead it is generated upstream and convected by the mean flow. But in the shear layer, close to the flap surface, intense turbulence is generated which can be associated with the large velocity gradients. Experience indicates that such intense turbulence production activities are always accompanied with the generation of intensified pressure fluctuations and noise.

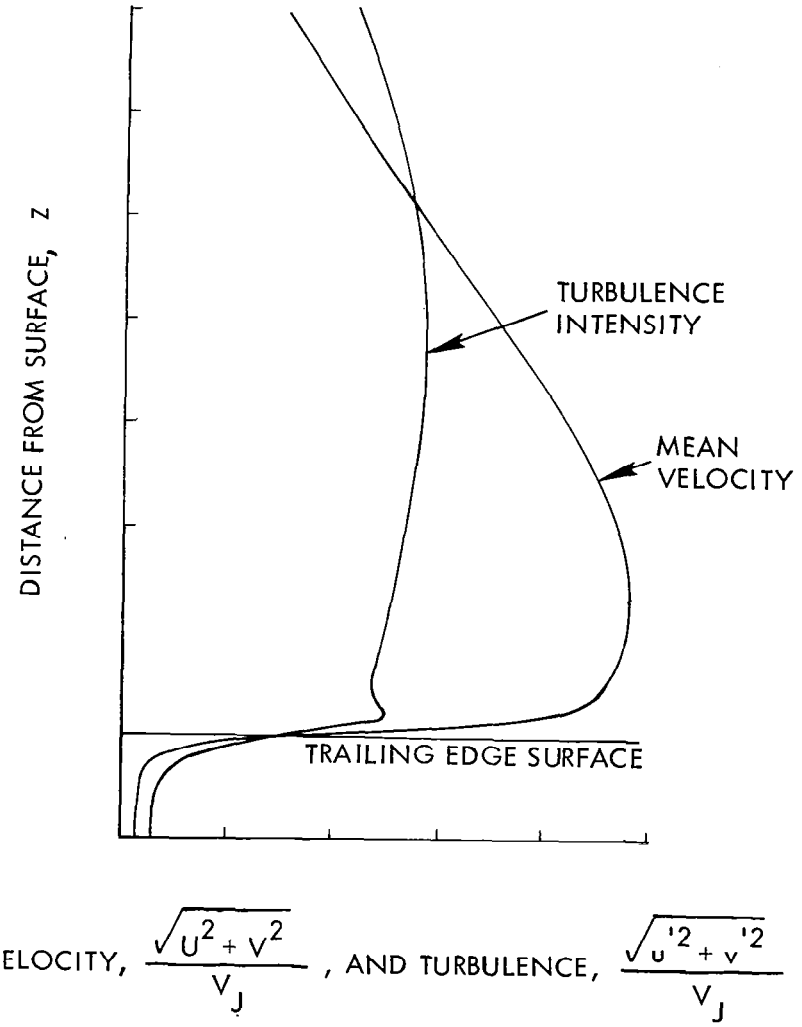

FIGURE 13. TYPICAL MEAN VELOCITY AND TURBULENCE INTENSITY PROFILE JUST DOWN STREAM OF TRAILING EDGE OF USB

All these arguments and observations led to a conclusion that the flow mixing noise in the trailing edge wake is a dominant noise generating mechanism in practical USB configurations. Since it is apparently the most important noise source, particularly from the community noise standpoint, it was therefore investigated further. Thus, a theory for USB trailing edge wake noise was developed as described in Section 5.

3. USB NOISE PREDICTION

One of the objectives of this program is to develop an analytical model and a far-field noise prediction program for an upper surface blown flap aircraft configuration. Available theoretical developments and the theory presented in Section 5 of this report are not adequate to formulate a prediction program for USB systems. Therefore, from the experimental data, empirical relations between the readily available engine and wing/flap parameters and noise are derived. The description of the tests and the data are presented in reference 1. Based on the theoretical background and past experience, the following parameters were evaluated in the test program:

1. Nozzle exit area
2. Nozzle exit shape
3. Nozzle exit velocity
4. Nozzle impingement angle
5. Flap radius of curvature
6. Flap length
7. Flap angle
8. Location of the nozzle with respect to wing and flap.

The general approach taken in developing the noise prediction program is illustrated in figure 14. The experimental program itself consists of two parts: (i) Acoustic tests and (ii) Flow tests. In the acoustic tests, the effects of various parameters on the sound field was investigated. In the flow tests, the flow characteristics of the jet over the wing and flap surfaces were measured to see that the propulsion performance was not deteriorated as the parameters were changed. Wherever changes in acoustic

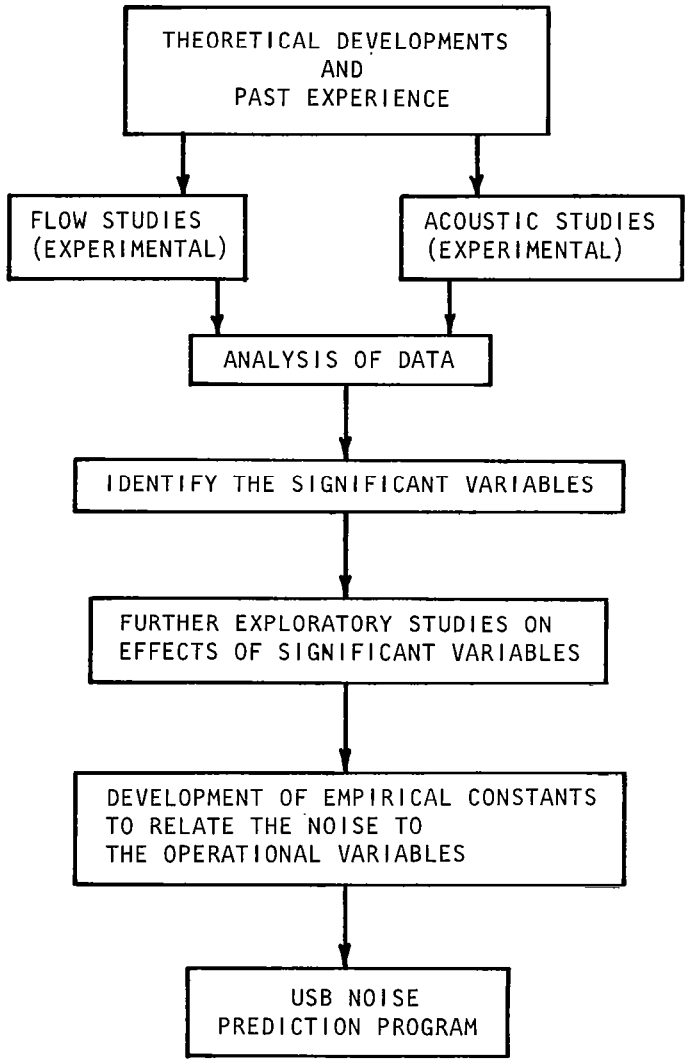

FIGURE 14. DEVELOPMENT OF NOISE PREDICTION PROGRAM

characteristics were observed, the turbulence structure and the mean flow properties were measured in addition to flow visualization. These results have been helpful in understanding the physics of the noise-generating mechanism.

The analysis of these data with the additional theoretical insight was used in identifying the variables having a major effect on noise. The effects of these important parameters were investigated by conducting further exploratory tests. Empirical constants were developed to relate noise to feasible aircraft variables. A USB noise prediction model was developed by using the acoustic data for a defined flight path.

In developing the noise prediction program, an attempt was made to generalize the observations made in the extensive flow and acoustic data bases and to incorporate them in the empirical prediction model. Implicit in the development of this model is the establishment of limitations and the determination of the level of agreement with other test data. This will also provide the way for further investigations to improve the model.

3.1 Derivation of the Noise Prediction Model

The prediction model was formulated by developing the relation between the OASPL or peak SPL and the various parameters. The primary considerations used in selecting the parameters were that these parameters were expected to significantly affect far-field USB noise, and they would be readily available to an airplane designer even in the early preliminary design stages. The empirical constants in the prediction model were derived using the experimental data generated in this program. It should be noted, however, that this prediction program has been verified with the other experimental data as discussed later in this section. The nondimensional spectra for the far-field sound was established using measured one-third octave band levels. Even though the nondimensional spectra distribution was derived empirically, physical reasons and explanations are provided. The directivity of the magnitude and the spectral distribution of sound were also derived from the measured data.

Overall Sound Pressure Levels. The effect of various parameters on the overall sound pressure levels or the magnitude of sound were determined using the experimental data. One of the obvious important parameters is jet exit velocity. If it is assumed that noise is generated from quadrupole or dipole sources, and using dimensional analysis, one may conclude that the far-field sound intensity is proportional to the mean velocity raised to the power 8 or 6 for quadrupole or dipole, respectively. In a complex system such as the USB configuration, however, use of such an approach is not appropriate. In fact, the total noise generated is a combination of many types of sources and probably each source is dominating in a particular general direction. Thus, it is assumed in general terms that sound intensity is proportional to the typical velocity raised to the power n. The jet exit velocity is taken as the typical velocity, since this velocity is the one which is known or can be easily calculated. It is observed from the experimental results that the velocity exponent, n is a function of a direction in which the sound propagates. This will be discussed further, later in this section.

Jet temperature effects are not included in the noise prediction. The limited experimental results obtained in this program indicated that the effects of mixed flow jet exhaust temperatures up to about 93°C (200°F) are not significant. However, exploratory investigations (experimental and analytical) should be conducted to find the effects of higher mixed flow temperatures and also the effects of various temperature distributions within the flow field. As more results are available, these effects should be incorporated.

The flight effects on the flow/surface-interaction noise are not included in developing the prediction formulas since experimental data were very limited. But these effects are incorporated as a correction in the program. This may be modified as more results are developed.

The jet exhaust nozzle exit shape and area are other parameters which could influence the sound levels. The nozzle shape has a very minor effect on sound. The variation of OASPL for different shapes of nozzles is shown in figure 15 which indicates that the OASPL increases as the nozzle aspect ratio

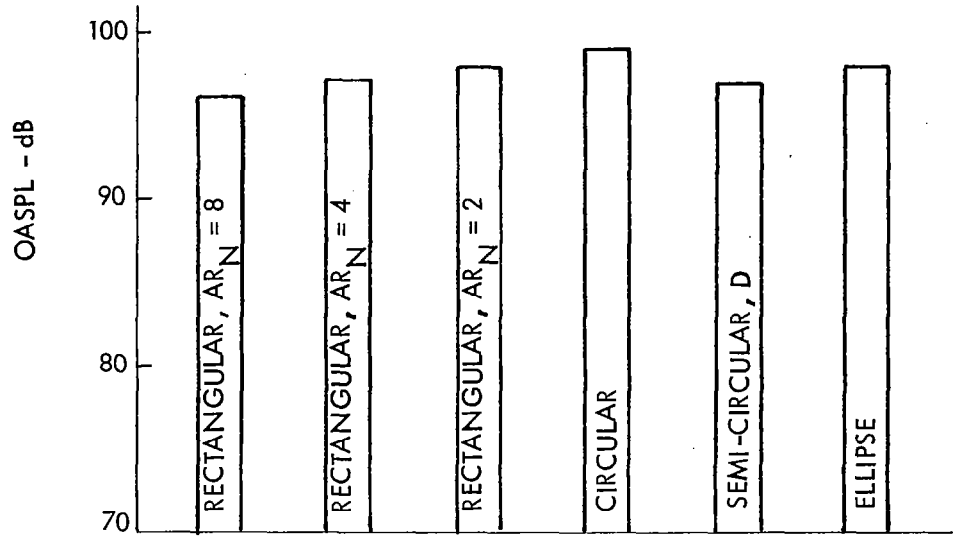

FIGURE 15. VARIATION OF OASPL WITH NOZZLE SHAPE
(ϕ = 90°, θ = 75°, V_j = 215 m/s, θ_N = 20°, L_F = 21.76 cm, δ_f = 30°, R_c = 7.62 cm)

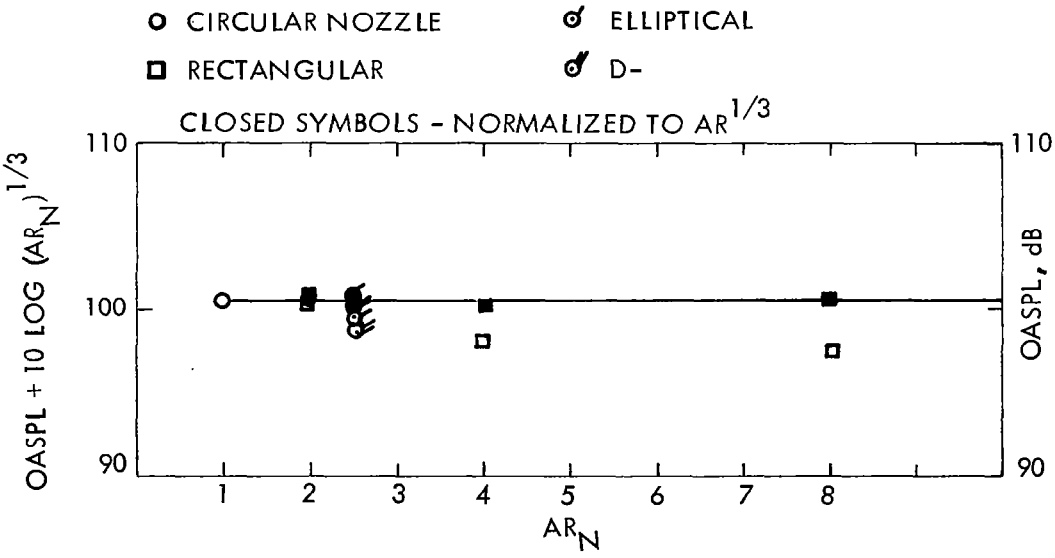

FIGURE 16. EFFECT OF NOZZLE ASPECT RATIO ON OASPL
(ϕ = 90°, θ = 90°, θ_N = 20°, V_J 215 m/s, L_F = 21.76 cm, δ_f = 30°, R_c = 7.62 cm)

decreases at least for rectangular shapes. Obviously, as the shape of the nozzle varies, the flow spreading on the surface changes and in turn the turbulence and noise generation may also change. It appeared from the data that the aspect ratio of the nozzle, AR_N, is a good parameter to be used in calculating noise levels. The nozzle aspect ratio is defined as the ratio between the square of maximum width to area of the nozzle. The variation of OASPL with nozzle aspect ratio is illustrated in figure 16, it is shown that the data correlates with $(AR_N)^{1/3}$. Thus, in developing the prediction program, the sound pressure levels are assumed to be proportional to $(AR_N)^{1/3}$. The nozzle area should influence the sound levels directly, since it has a strong influence on the mixing process and the turbulence generation. In figures 15 and 16, even though two sizes of nozzles were used, they were normalized to the same area of 20.26 cm^2 making use of the assumption that sound pressure is proportional to the area. Since there is no large deviation in this figure, it is assumed that the sound pressure level or sound intensity is proportional to the area of the nozzle exit as in the case of jet noise.

The sweep angle of the wing was assumed to have no effect on the noise characteristics of the USB configuration. It should be noted, however, the turbulence and the mean flow characteristics of the jet flow in the trailing edge wake may be different in flight for swept wings as compared to the straight wings. This phenomena should be studied further in conjunction with flight effects. In the development of the noise prediction program, the experimental data from the straight wing only was used. Other geometric parameters that were thought to be important were the transverse (z) and longitudinal (x) location of the nozzle exit on the wing, flap length, flap knee radius of curvature, and the flap deflection angle. The transverse location of the nozzle is not considered in this analysis, because the data used are only for the nozzle lip located right on the surface of the wing. If the nozzle is lifted from the wing, the flow and the noise characteristics change slightly. In fact, there may be some optimum combination of transverse and longitudinal location where the noise levels are minimum. However, for the purpose of noise prediction, it is assumed that these location effects are negligible, provided that the flow is fairly smooth and attached and turned along the surface. The longitudinal location of the nozzle and flap length

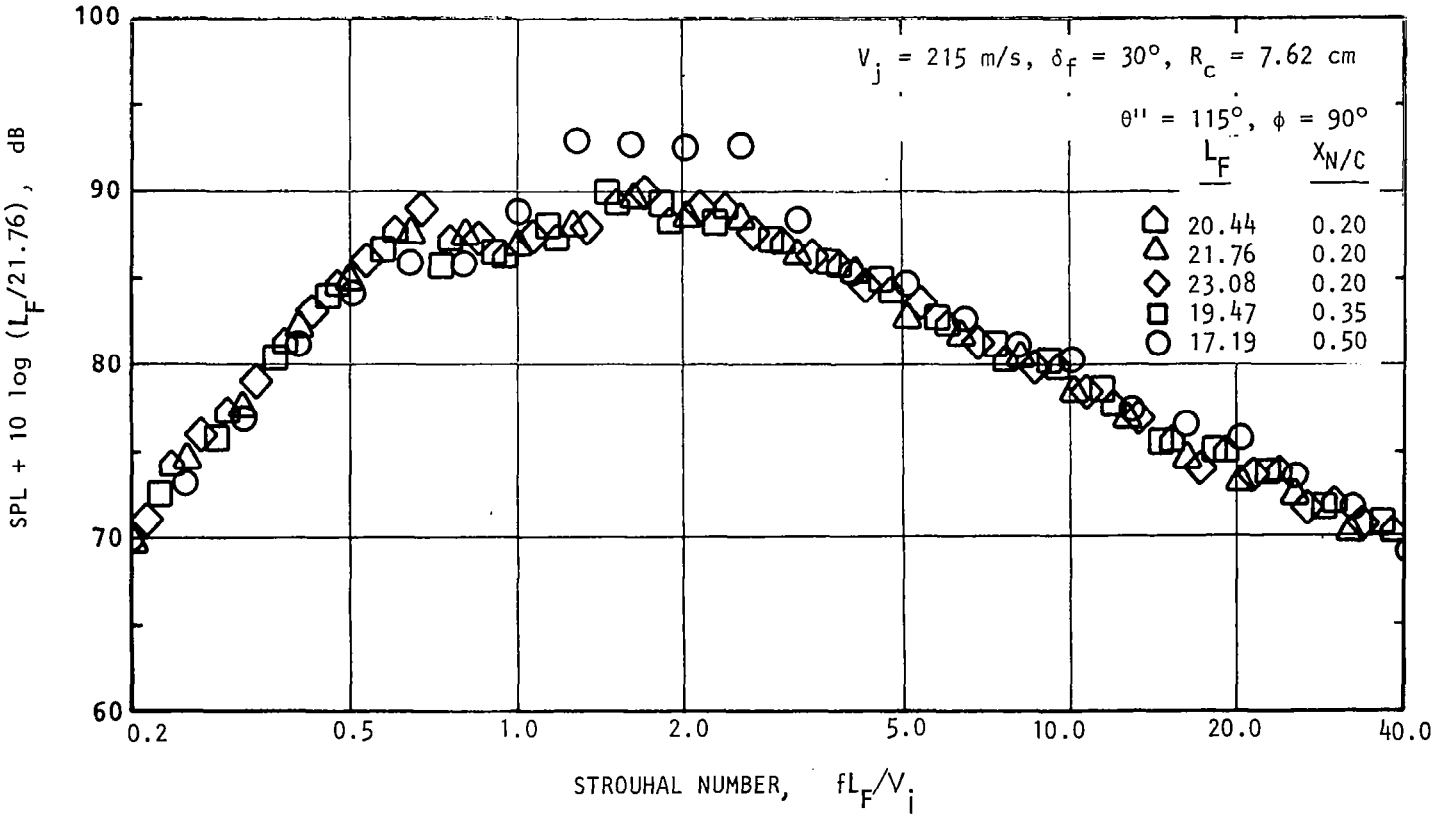

FIGURE 17. CORRELATION OF DATA FOR FLOW LENGTH EFFECTS, AR_N = 4 NOZZLE

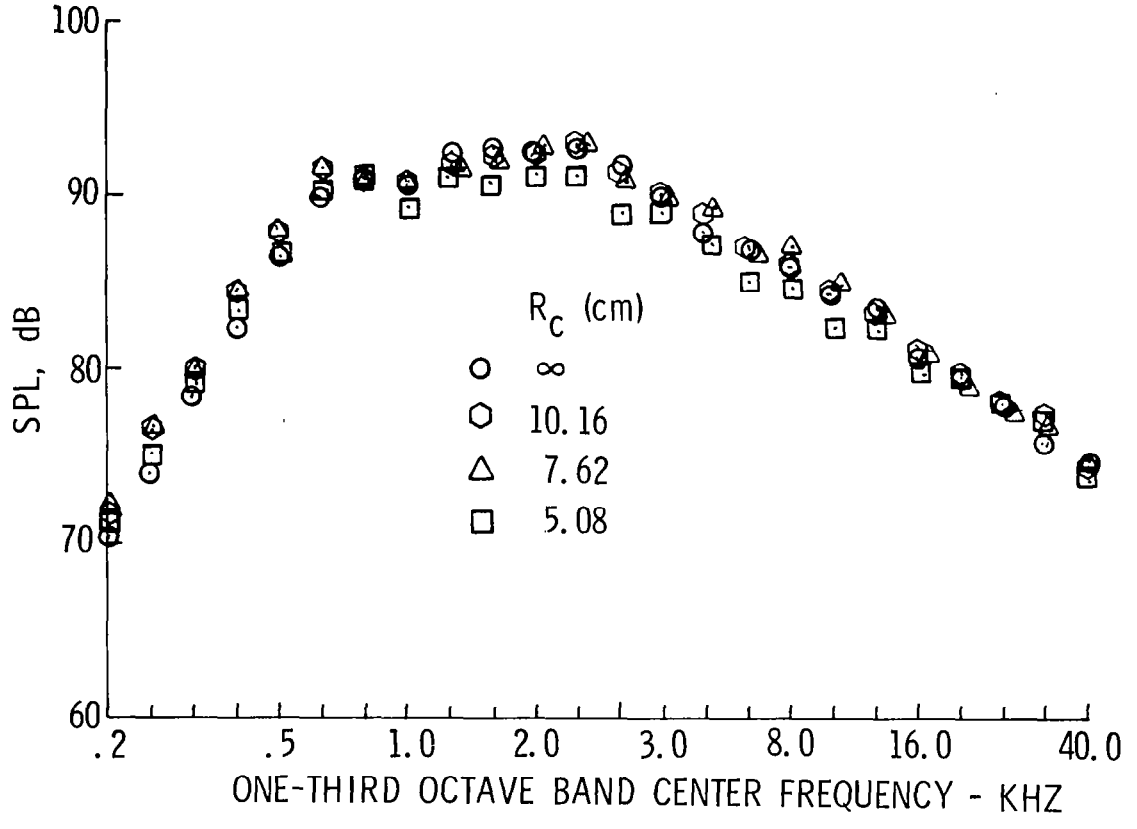

FIGURE 18. EFFECT OF FLAP RADIUS OF CURVATURE ON SOUND SPECTRA

($AR_N = 4$, $\delta_f = 30°$, $\theta = 90°$)

are interrelated. Since the chordwise length between the wing leading edge and the nozzle exit do not affect the flow characteristics, for the static case, it may be assumed that the noise characteristics are independent of this length. Then, in the case of an unslotted flap, the longitudinal length between the nozzle exit and the trailing edge may be divided into three parts: (1) the distance between the nozzle exit and start of curvature, (2) the curved section, and (3) the straight trailing edge section. The experimental data indicates that the total length between the nozzle exit and the trailing edge, known as "Flow Length" is the controlling parameter for a constant knee radius and flap angle, provided the flow is attached and turned along the surface (see figure 17). Figure 17 shows one-third octave spectra using nondimensional frequency for five flow lengths consisting of three nozzle locations and three flap trailing edge lengths. The basis for nondimensional frequency will be discussed later. The sound intensity is assumed to vary inversely as flow length. As can be seen, the data collapse very well. It was anticipated originally that the noise levels and spectral distributions would be a strong function of knee radius of curvature. However, the experimental results shown in figure 18 indicate that the radius of curvature has a negligible effect on far-field sound. But, if the radius of curvature is too small so that the flow can separate before leaving the trailing edge, then the noise levels may increase or decrease substantially depending on the location of the separation. Since only configurations where the flow is attached are of present interest, the effect of radius of curvature can be neglected. The variation in flap angle does not change the total noise generated if the mean flow velocity at the trailing edge is kept constant. For the practical range of flap deflections ($\delta_f \leq 60°$), it may be assumed the velocity at the trailing edge does not vary. However, the flow direction at the trailing edge varies as the flap deflection angle changes. Thus, for a constant angle from the delfected flap trailing edge, the noise levels are constant. This effect will be discussed further under the spectral Distribution.

The equation for the peak SPL of one-third octave band spectra is given by

$$\text{Peak SPL} = 10 \log \left(\frac{V_J}{V_o}\right)^{n(\phi,\theta'')} + 10 \log \frac{A_N}{A_o} - 20 \log \frac{R}{R_o}$$

$$- 10 \log \left(AR_N{}^{1/3} \cdot \frac{L_F}{D_H}\right) + K(\phi,\theta''), \qquad (1)$$

where V_J = Jet exit velocity, m/sec

V_o = Reference velocity (200 m/sec)

A_N = Nozzle exit area (m^2)

A_o = Nozzle exit reference area (1 m^2)

AR_N = Aspect ratio of the nozzle (W_N^2/A_N)

W_N = Width of the nozzle (m)

R = Distance from the aircraft (m)

R_o = Reference distance (1 m)

L_F = Flow length (length on the surface between the nozzle exit and the trailing edge, m)

D_H = Hydraulic diameter of the nozzle exit (m)

n and K are constants.

Hydraulic diameter of the nozzle exit, D_H, has been found to be a good correlating parameter for the turbulence intensity distribution near the trailing edge. The hydraulic diameter can influence the spreading characteristics of the jet on the surface; and, therefore, the ratio of L_F/D_H is used as one of the geometric parameters in equation (1). The nondimensional spectra shown in figure 19 illustrate how well the data collapse for different nozzle parameters (AR_N, D_H, and A_N).

The velocity exponent n and the constant K depend on the direction in which the sound radiates. Figure 20 illustrates the variation of OASPL with jet velocity, V_J for different angles, θ'' in the flyover plane, $\phi = 90°$. For the description of other angles, θ and θ', see figure 1.

Directivity and Spectral Distributions. As mentioned in the previous paragraph, the experimental data have indicated that the sound intensity and its variation with jet velocity are functions of directivity. This effect of

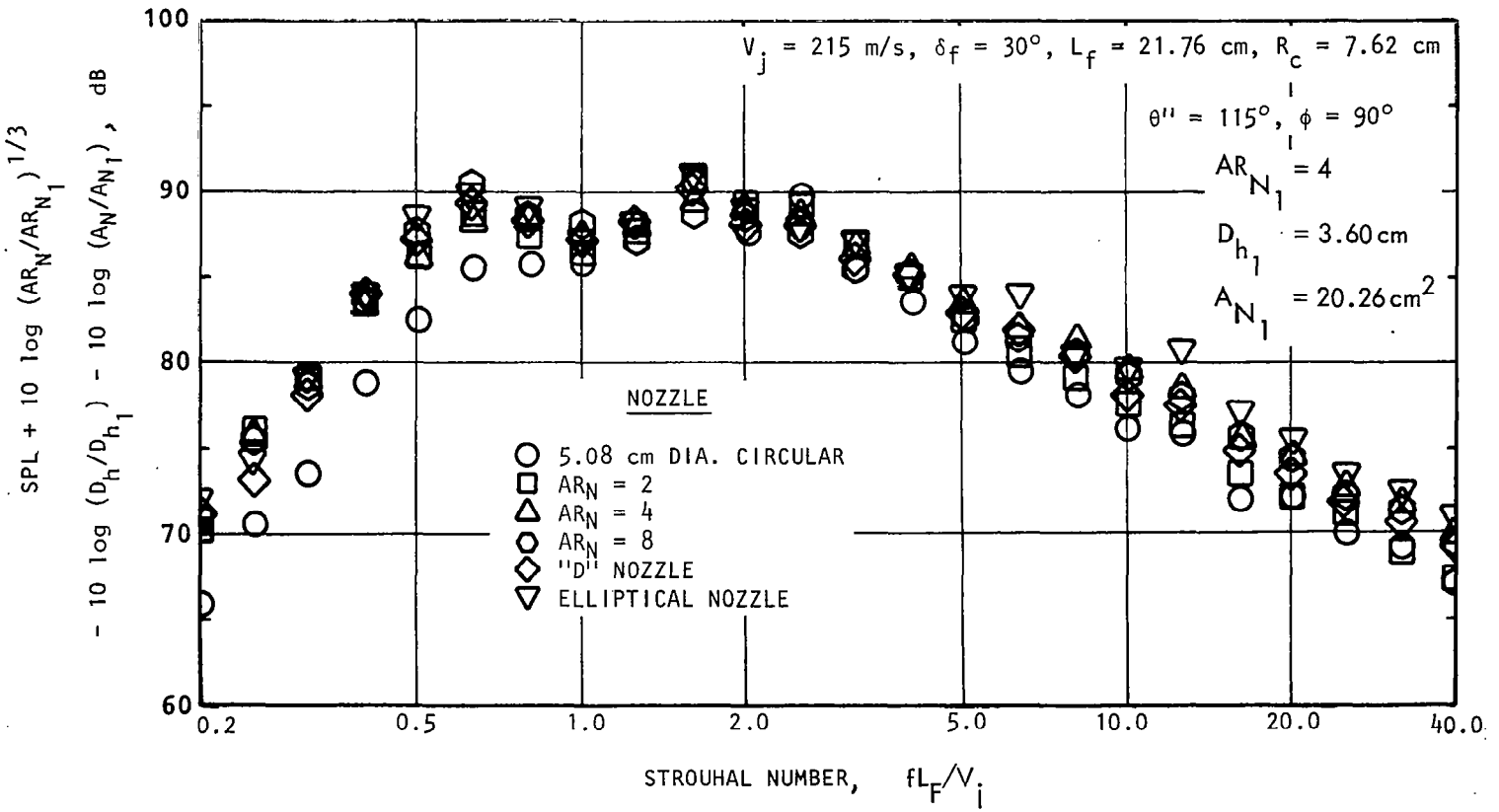

FIGURE 19. CORRELATION OF DATA FOR NOZZLE SHAPE EFFECT

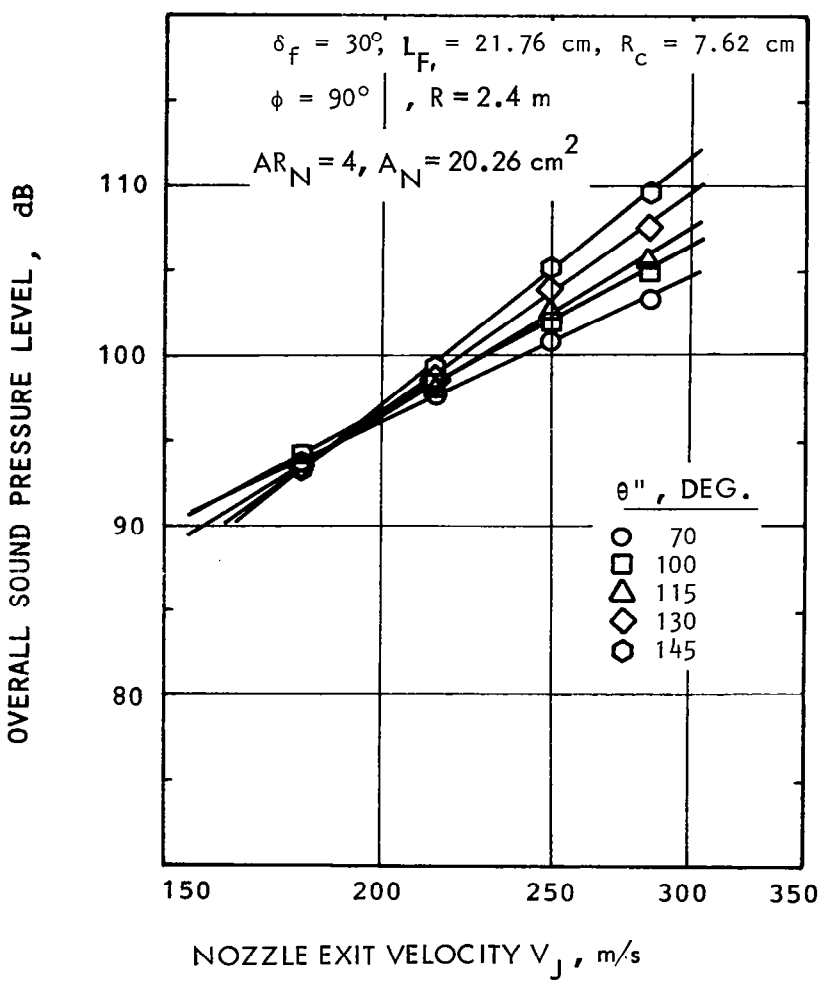

FIGURE 20. VARIATION SOUND PRESSURE LEVEL WITH JET EXIT VELOCITY

directivity is primarily due to (1) the contribution of different sources with different characteristics in different directions and (2) the refraction of sound through the shear layer. Thus, the velocity exponent n and the constand K are determined empirically as a function of the direction (ϕ,θ''). ϕ is the angle between any plane and the plane through the jet axis and parallel to the wing lateral (span) axis. θ'' is the angle from the flap trailing edge as shown in figure 1 (in the flyover plane, $\phi = 90°$, $\theta'' = \theta' + \delta_f$). The velocity exponent derived from the experimental data are presented in reference 1. Figure 21 shows the variation of velocity exponent as a function of ϕ and θ''. The constant K in equation (25) is determined by fitting the experimental data of all the configurations tested and shown in figure 22.

The length scale in determining the nondimensional frequency (Strouhal number) was based on the experimentally obtained far-field sound and the flow characteristics in the trailing edge wake. The flow length, L_F, was found to be the parameter which had strong influence on flow characteristics. Therefore, it should be logical to assume that the Strouhal number is derived as fL_F/V_J, and should be based on L_f as also shown in reference 28. The spectral distribution of sound was also found to be a function of flap deflection, δ_f. Thus, including the flap deflection, the Strouhal number is modified as $fL_F/V_J(1 + \delta_f)^{1/3}$. Figure 23 shows the spectral distribution using this frequency parameter for three flap angles in the flyover plane at $\theta'' = 115°$ and $145°$. The spectrum shape is similar for all values of ϕ and θ''. However, the Strouhal number $fL_F/(1 + \delta_f)^{1/3}$ is a function of directivity as discussed earlier. Thus, a frequency shift parameter, F_s was derived from the experimental data of all configurations and shown in figure 24. A unified spectrum shape for noise prediction purposes has been derived from the experimental data shown in figure 25. These data are for a constant $\phi = 90°$ (flyover plane). However, the spectrum shape was assumed to be unchanged for all the directions of practical importance. Figure 26 is the spectral distribution in various directions using the above analysis normalized to the direction $\theta'' = 90°$ and $\phi = 90°$. The results indicate that the formulation agrees in all directions.

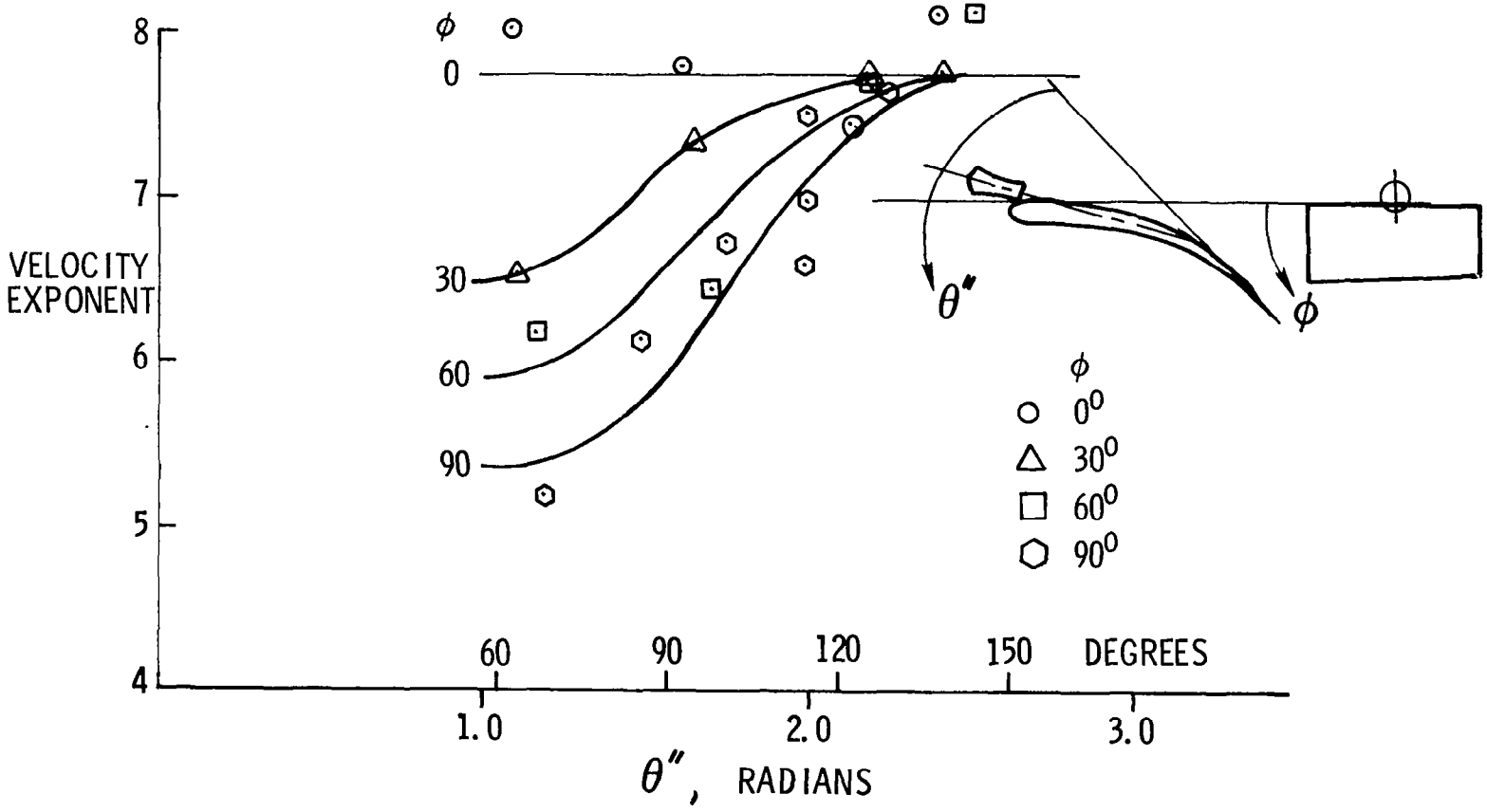

FIGURE 21. VELOCITY EXPONENT VS. DIRECTIVITY ANGLES θ" AND φ TO BE USED IN EQUATION 1

($\delta_f = 30°$, $L_F = 21.76$ cm, $R_c = 7.62$ cm, $AR_N = 4$)

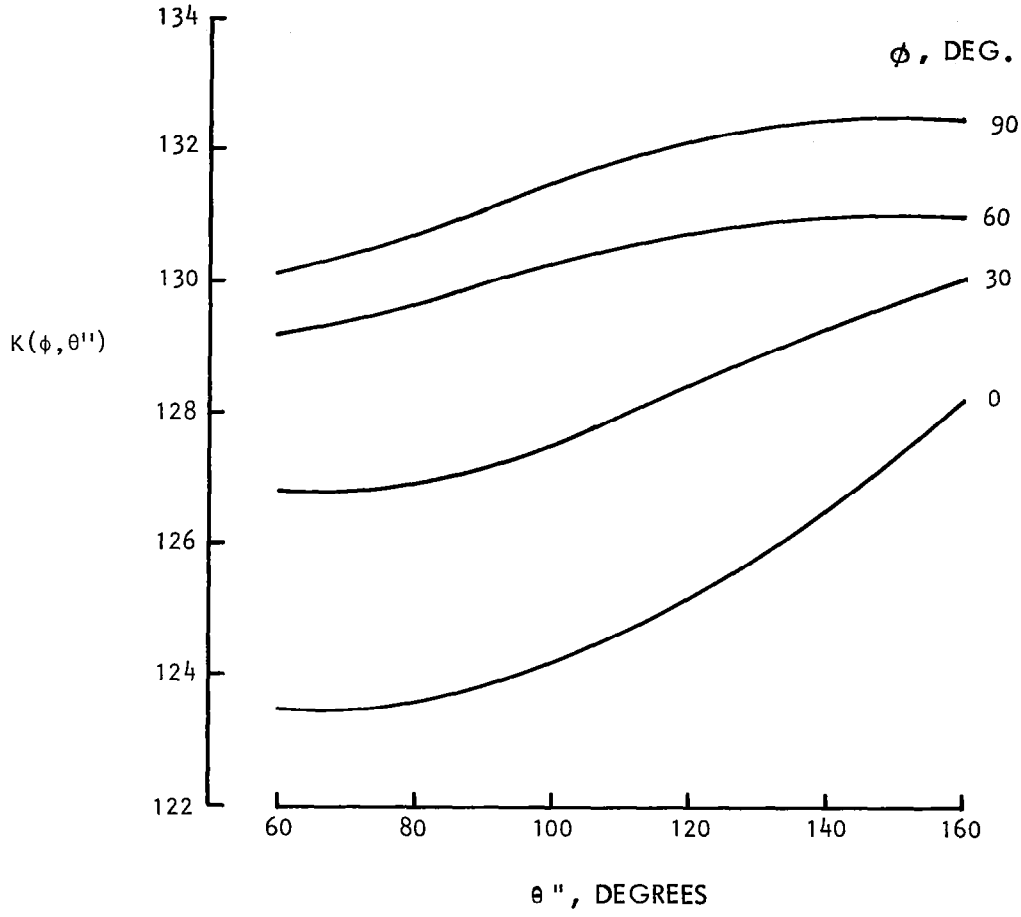

FIGURE 22. CONSTANT K VS. DIRECTIVITY ANGLES θ" AND ϕ TO BE USED IN EQUATION 1

(DERIVED FROM THE TEST DATA OF ALL CONFIGURATIONS)

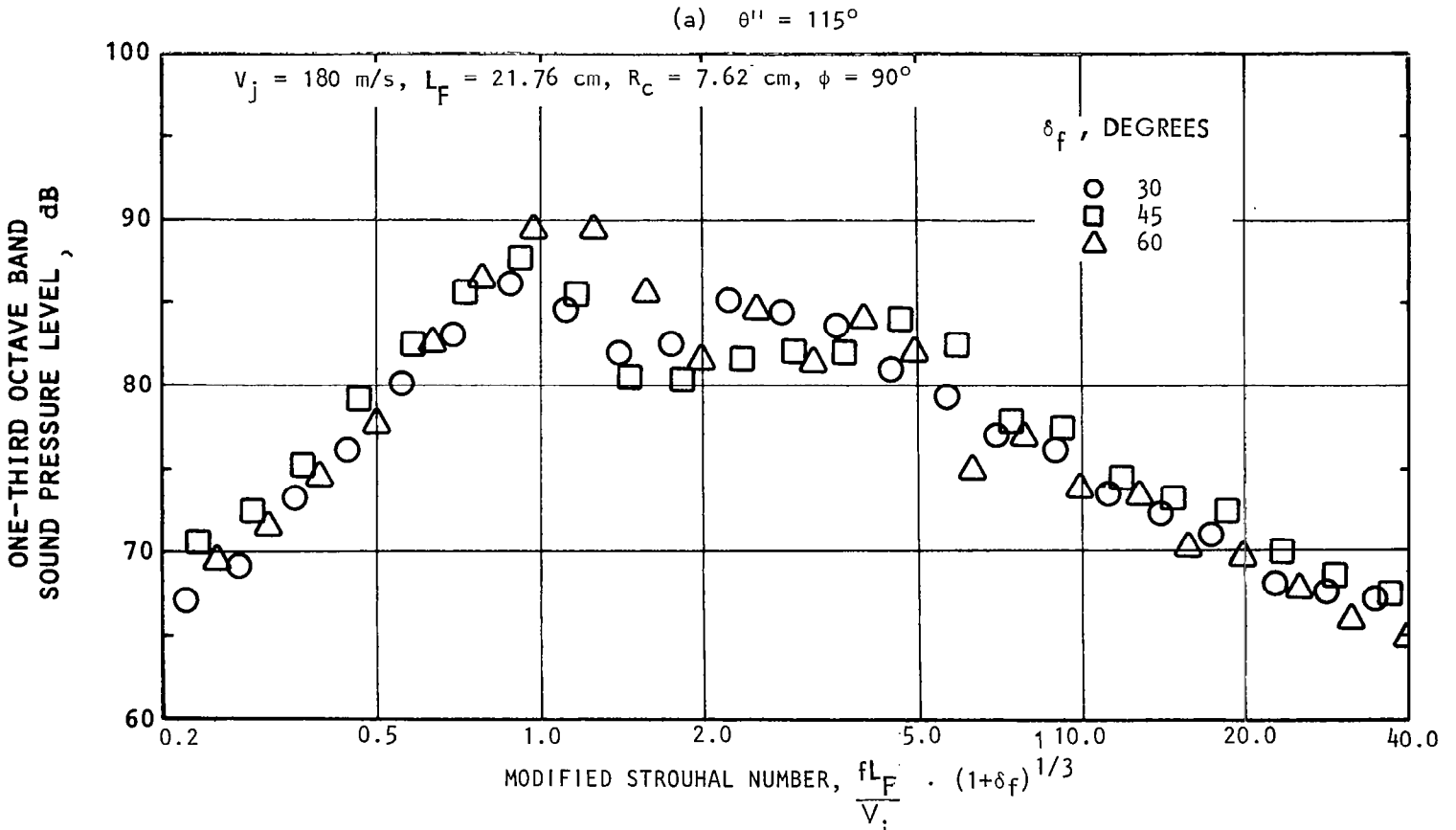

FIGURE 23. CORRELATION OF SPECTRAL DATA AT VARIOUS FLAP DEFLECTIONS USING MODIFIED STROUHAL NUMBER, AR_N = 4 NOZZLE

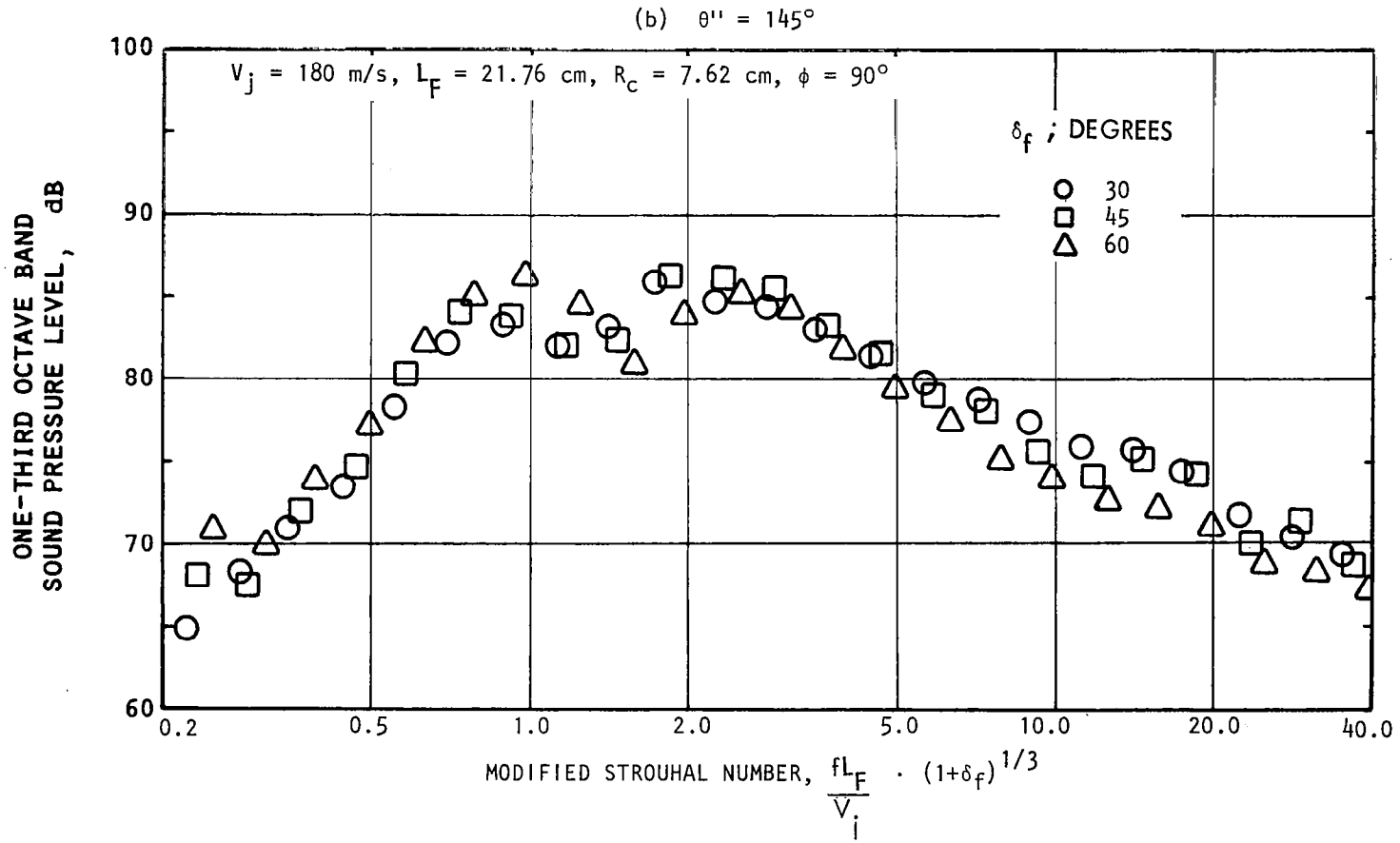

FIGURE 23. (CONCLUDED)

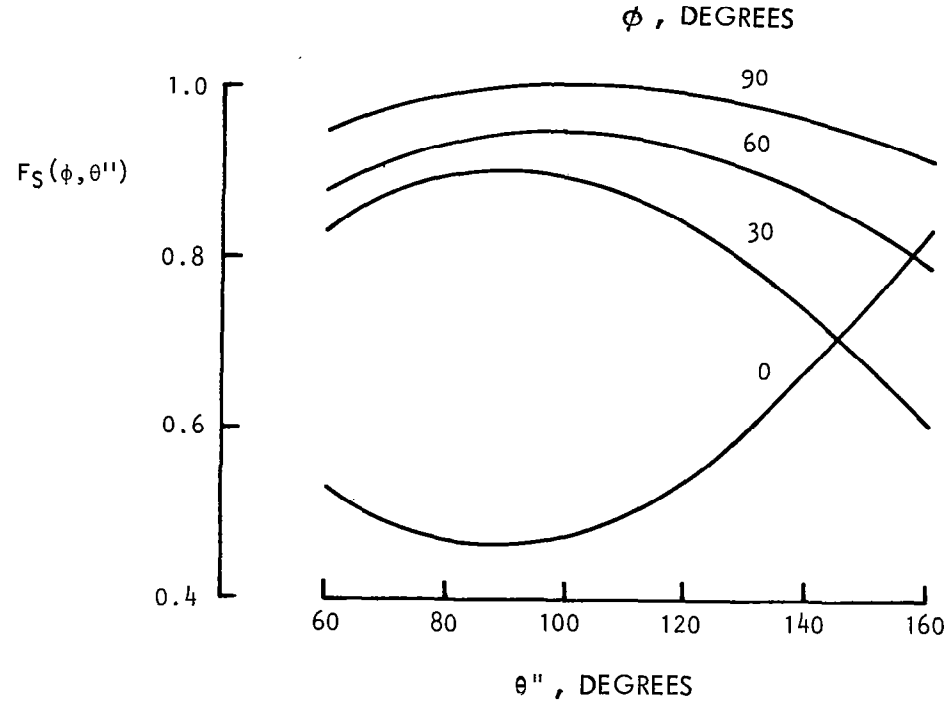

FIGURE 24. FREQUENCY SHIFT PARAMETER (F_S) VS. DIRECTIVITY ANGLES θ" AND φ

(DERIVED FROM THE TEST DATA OF ALL CONFIGURATIONS)

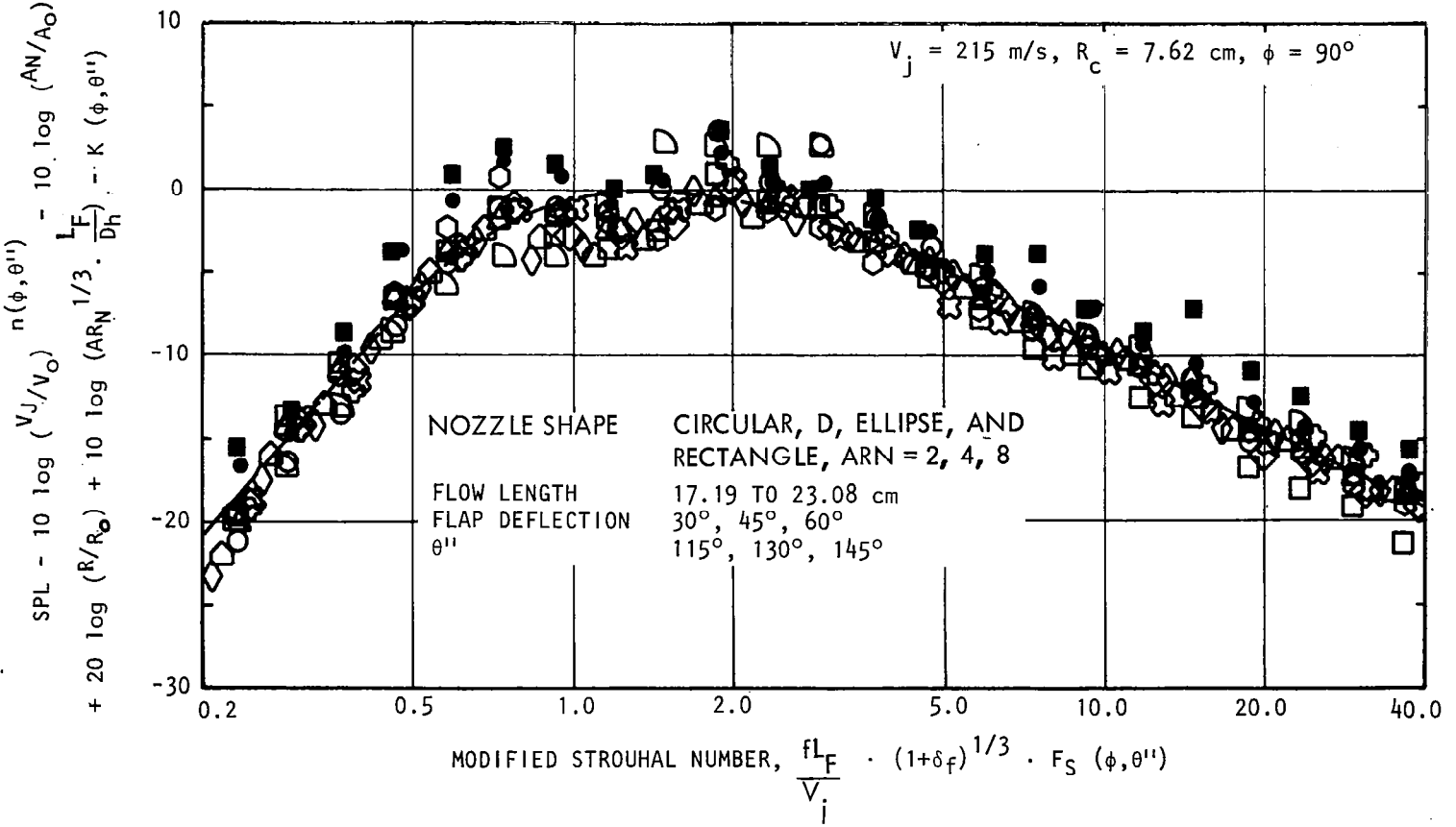

FIGURE 25. UNIFIED SPECTRUM SHAPE FOR USB NOISE FORMULATION

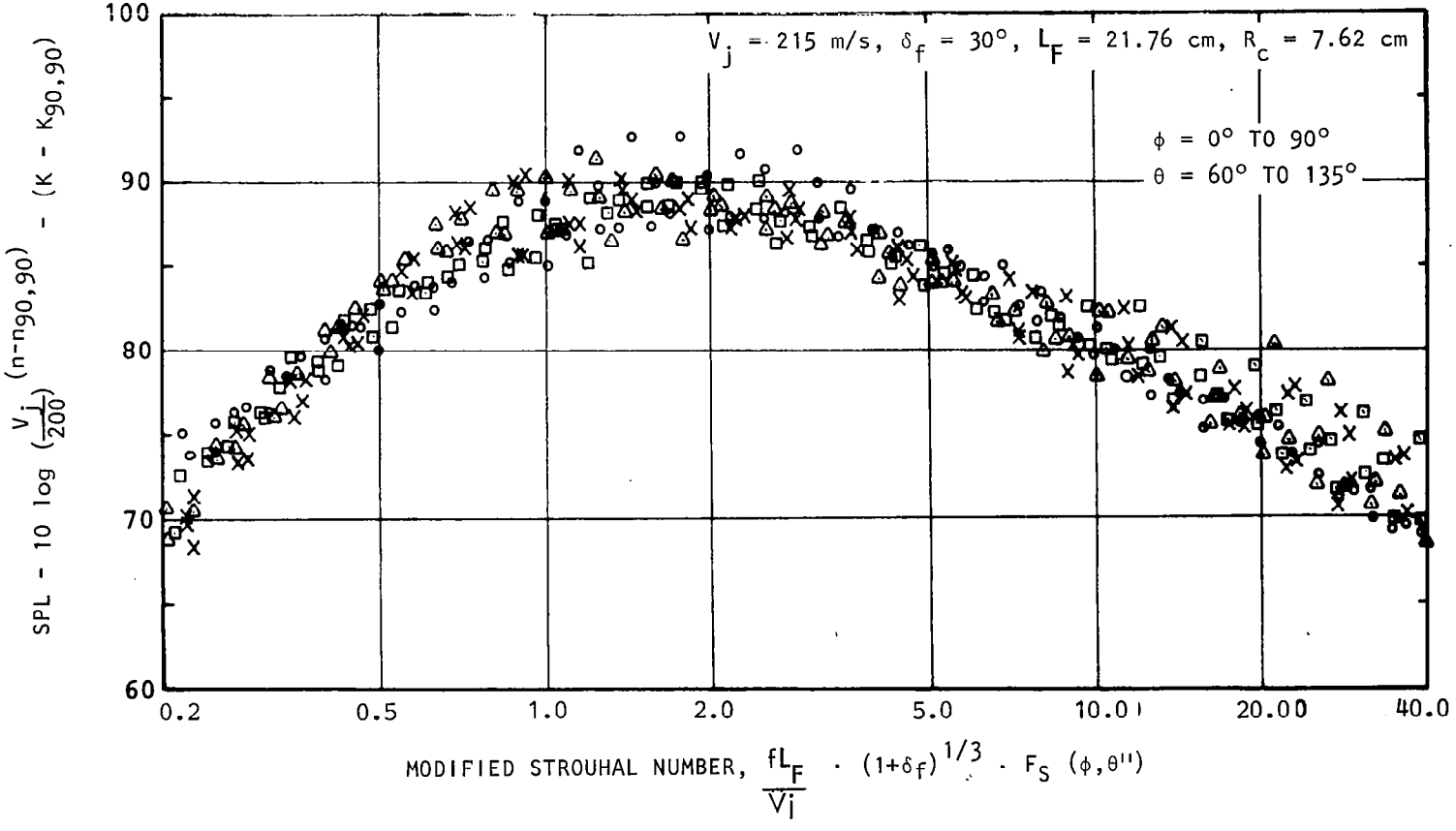

FIGURE 26. SPECTRAL DATA AT VARIOUS DIRECTIVITY ANGLES NORMALIZED TO $\phi = 90^\circ$ AND $\theta'' = 90^\circ$, $AR_N = 4$

3.2 Comparison With Test Results

Equation (1) and the graphs illustrated so far were used to evaluate the peak SPL and one-third octave spectra at any given far-field location. The predicted results are compared with the static scaled model experimental data in this section.

Figure 27 illustrates the comparison of one-third octave band sound pressure levels measured in the anechoic room with the prediction. The experimental data presented in this figure are for different jet exhaust velocities, nozzle areas and shapes, flow lengths and flap angles. As can be seen from this figure, the experimental data fall within ±2 dB from the prediction in all frequency ranges. The data are scattered most in the mid-frequency range and appear to show two peaks. As it is suggested in Section 2, this may be primarily due to reflection and refraction by the rigid surfaces of the test rig. The data correlation shown in figure 29 shows that the prediction model is quite good.

The experimental data from the acoustic performance test facility (large scale model data) are compared with the prediction in figure 28. The measured data in this figure are for two rectangular nozzles with an aspect ratio of 4 and 8. The data have been corrected for ground reflection. The band of scatter is somewhat greater than the anechoic room. However, the comparison between prediction and measured data is good for this case also.

The prediction model is compared with the small-scale model test results reported in reference 12 (figure 29). The measured data are for the baseline wing at the 20° flap deflection given in figure 17a of reference 12. Predicted sound levels were a little less than the measured data. However, considering the differences in test setups and configurations including nozzle geometry ahead of the exit, the comparison is satisfactory.

Another comparison with the full-scale model static test data of reference 29 is shown in figure 30. The model utilized a highly suppressed TF34 engine with mixed flow exhaust and an aspect ratio 4 nozzle. Measured

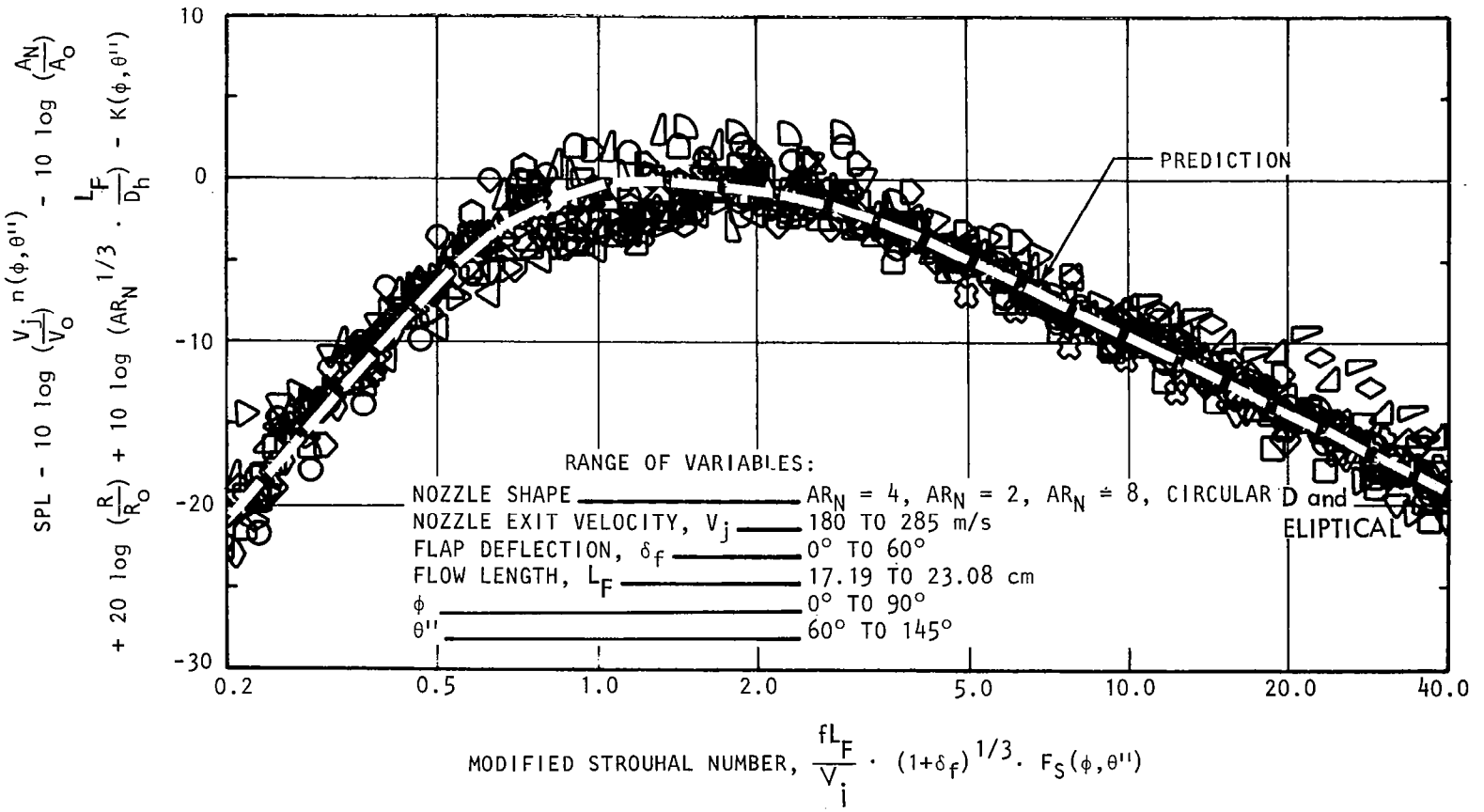

FIGURE 27. COMPARISON OF MEASURED AND PREDICTED SPECTRAL DATA (SMALL SCALE MODEL).

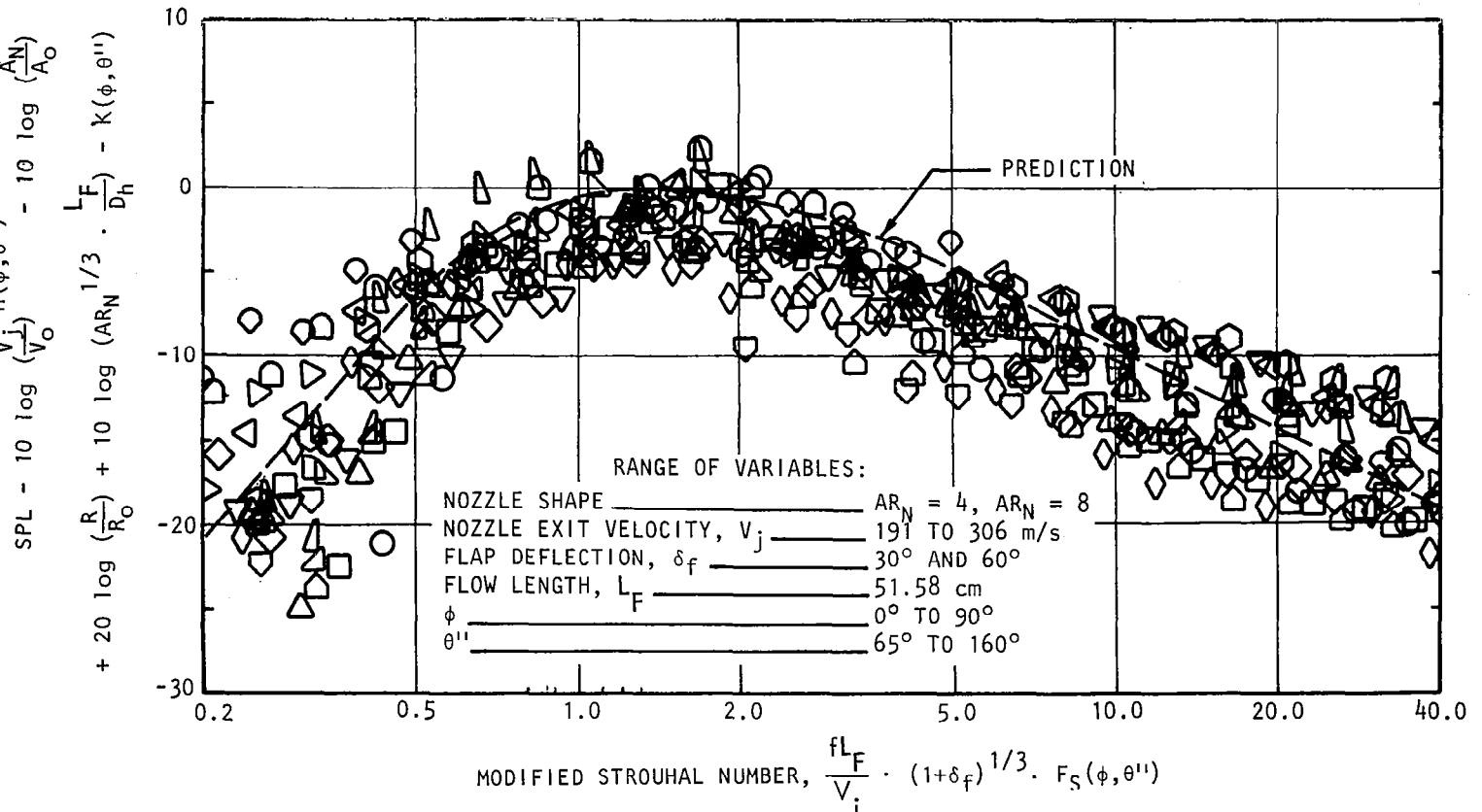

FIGURE 28. COMPARISON OF MEASURED AND PREDICTED SPECTRAL DATA (LARGE SCALE MODEL)

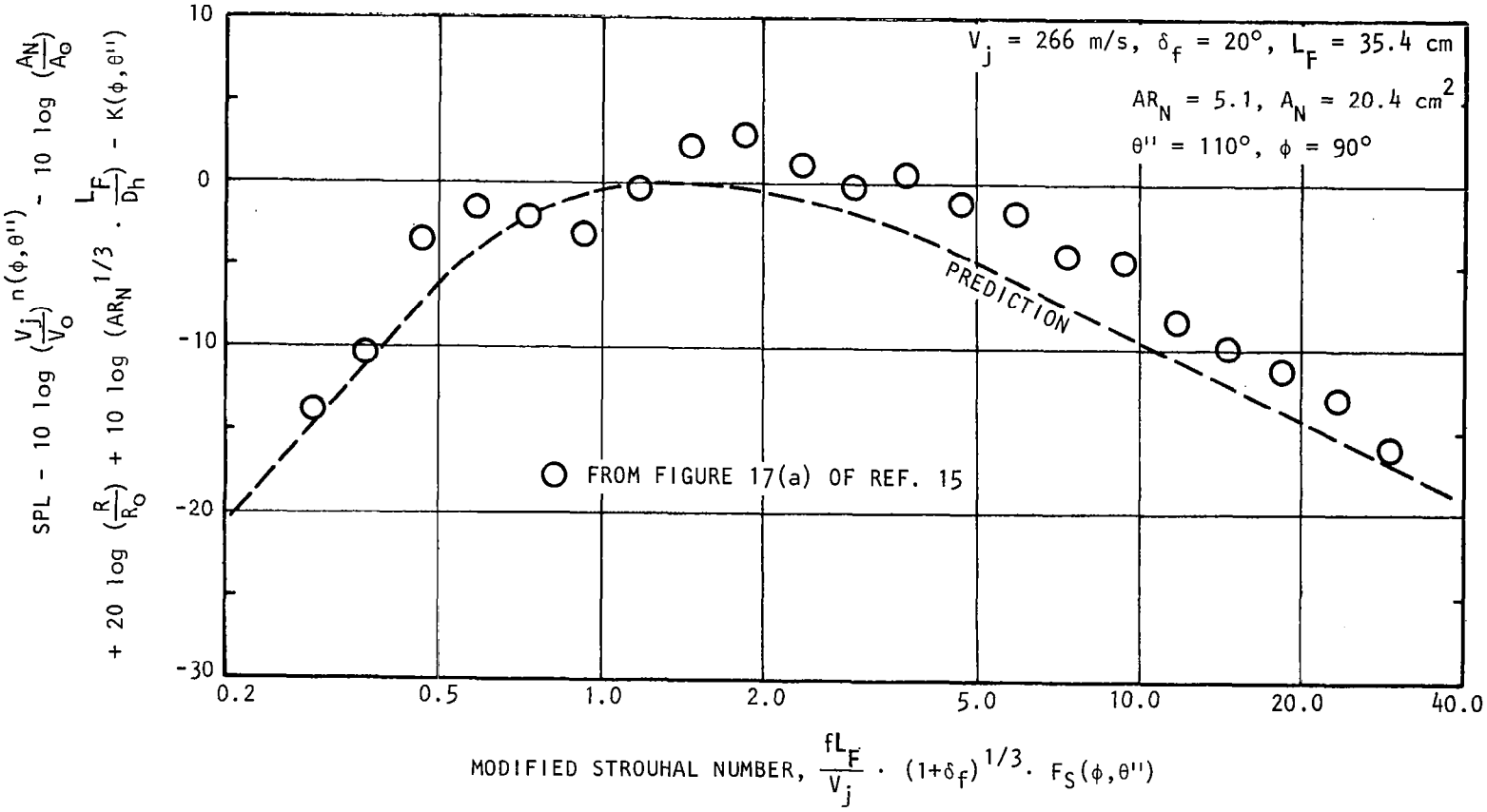

FIGURE 29. COMPARISON OF PREDICTION WITH RESULTS OBTAINED BY VON GLAHN AND GROESBECK (REF. 15)

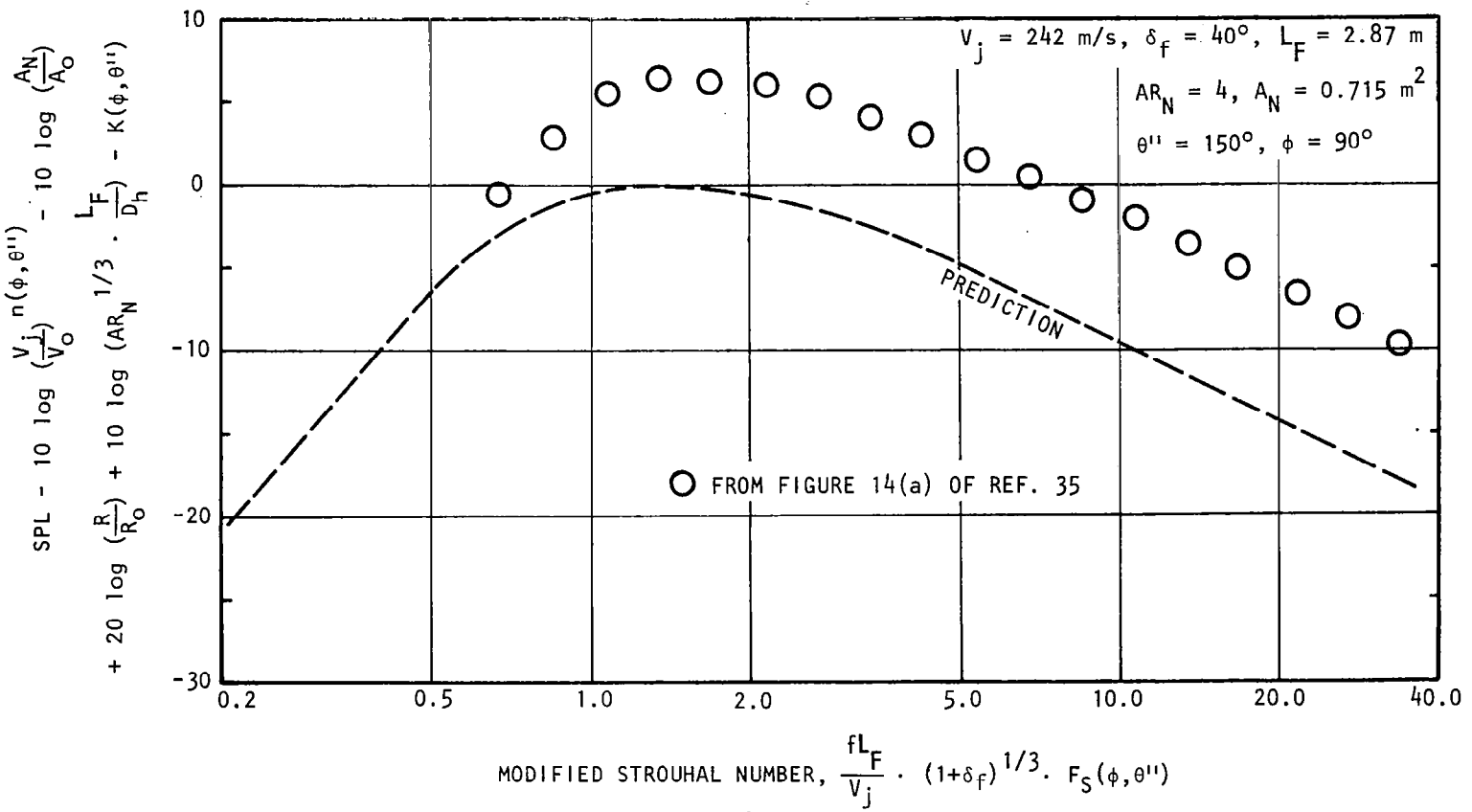

FIGURE 30. COMPARISON OF PREDICTION WITH RESULTS OF FULL SCALE USB TEST DATA OF REF. 35

spectra are presented for the short flap configuration at 40° flap deflection. The predicted results are again lower than measured. Differences in test conditions, such as flow turbulence at the nozzle exit with a real engine and other environments are expected to account for some of the differences. However, this anomaly is not completely explainable at this time.

3.3 Application and Limitations

The prediction model was derived in part by the use of the experimental data from static tests of scaled models. Consequently, a brief description of the range of the parametric variations included in this investigation will help establish the range of applicability that can be expected for the purpose of noise prediction. The following range of jet parameters were utilized in the derivation of the prediction model:

Nozzle Shape:	Rectangular ($AR_N = 2,4,8$) Circular, Elliptical and D
Flap Deflection:	0°, 30°, 45°, 60°
Nozzle Impingement Angle:	$\theta_N = 20°$
Nozzle Chordwise Location:	$X_N/C = 0.20, .35$
Nozzle Vertical Position:	$Z_N = 0.0$
Jet Temperature:	Ambient
Jet Velocity:	180 to 285 m/s
Flow Length/Hydraulic Diameter (L_f/D_H):	9.3 to 3.2

The nozzle impingement angle for purposes of the prediction equation is taken to be an angle near the minimum required to produce a significant spanwise region of attached flow at the trailing edge. An angle of 20° has been used for all nozzles based primarily on the surface flow visualization studies. Variations of this angle while maintaining attached flow can produce significant changes in the noise levels and spectral shapes. Similarly, nozzle contours which do not provide a smooth flow distribution at the exit should not be expected to correlate well with the present model.

Furthermore, differences in turbulence characteristics of the flow at the nozzle exit, as with an actual engine, are not accounted for in the model.

A nozzle chordwise location of 20% chord with the nozzle on the wing surface ($Z_N = 0$) has been used in the formulation. The data indicate that variations in the nozzle location may be effectively accounted for in the determination of flow length. The formulation is based mostly on ambient temperatures for the jet, but it is verified with limited data of the mixed flow exhaust with temperatures up to 93°C (200°F). Thus, it may be assumed that this model is applicable for exhaust temperatures at least up to 93°C. The criteria for the flap knee radius of curvature is for the jet flow to be attached and turned along the wing and flap surfaces.

The effects of forward speed have not been included in the prediction equation since no conclusive trends have been established from the wind tunnel data. For the noise footprint calculations of the aircraft described in Section 7, the flight effects are included as discussed below.

All of the above considerations should be taken into account in determining the applicability of the prediction model to a given configuration.

3.4 Computer Program

A computer program has been developed to predict the noise of aircraft with USB powered-lift systems. This program consists of routines for the various aircraft noise sources and the factors affecting the radiation to the far-field (community). A footprint program is also available to generate airport noise contours.

A simplified flow chart of the complete program is given in Figure 31. The following six noise sources are considered in developing the prediction program for USB aircraft: (1) high-lift system, (2) airframe, (3) fan, (4) turbine, (5) wing-jet, and (6) auxiliary power unit (APU). For high-lift noise, a computer routine is written based on the empirical formulation described previously in this section. In essence, several noise generating

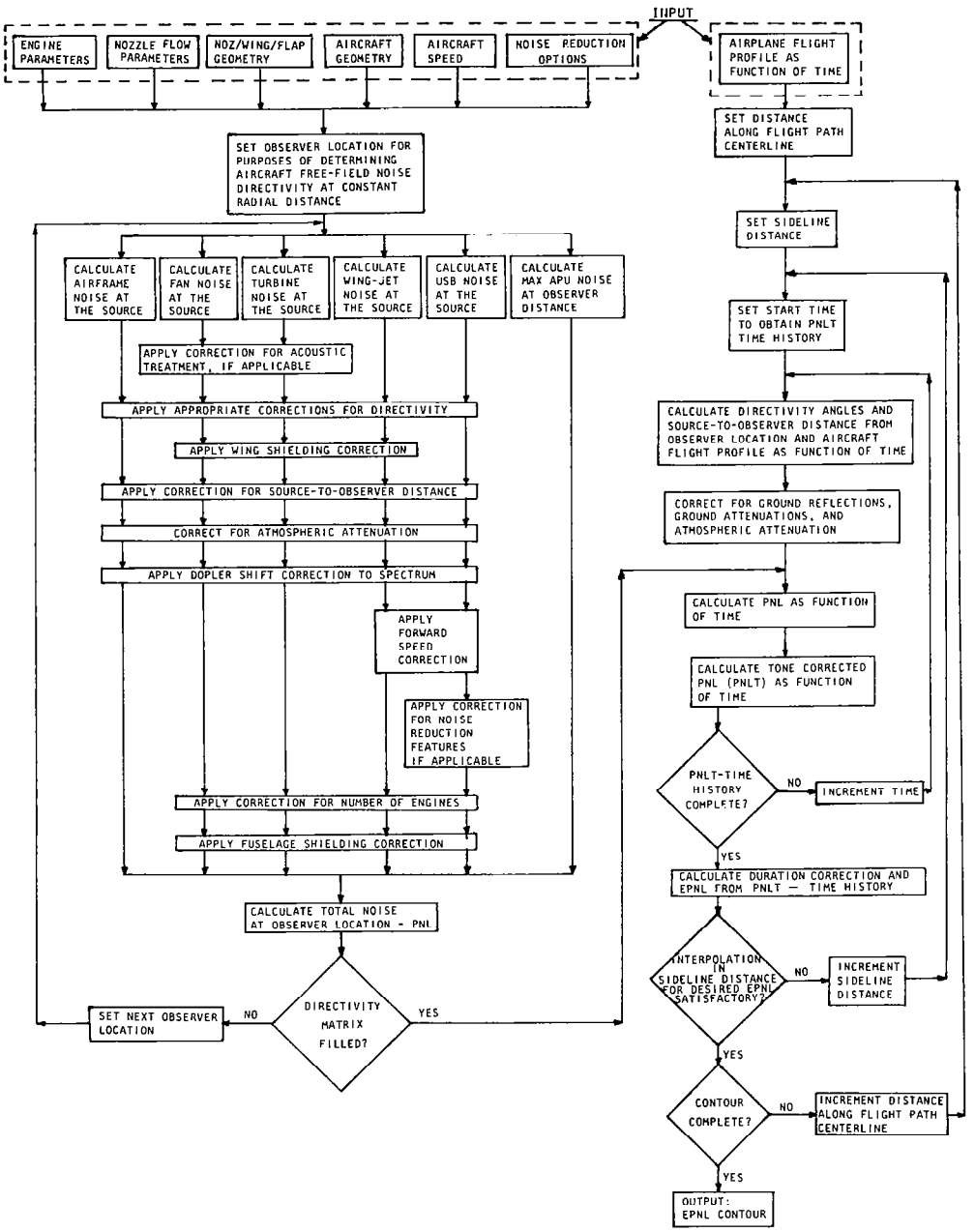

FIGURE 31. FLOW CHART OF NOISE FOOTPRINT PREDICTION PROGRAM

mechanisms for high-lift systems such as jet, excess engine (which includes nozzle lip and combustion), impingement, wall-jet, trailing-edge wake, and trailing-edge noise have been considered as a single high-lift noise source. Computer routines for the calculation of noise levels, spectra, and directivity for all the other sources are derived in reference 30. Since the analysis of the noise characteristics of these sources is beyond the scope of this study, the computer routines are retained without any modification. The methods used in the program to determine the aircraft noise radiated to an observer are described in reference 30.

The effects of forward speed on community noise are treated as a correction to the high-lift noise. Since forward speed effects have not been incorporated in the present formulation, the forward speed correction given in reference 30 has been retained in the present program. A Doppler-shift correction for forward speed is also applied to all source spectra except the APU. To determine the aircraft sound spectral distribution, the directivity pattern of each noise source, except the APU, is included in the basic prediction routine for that source. Furthermore, a wing-shielding correction is calculated for the fan, turbine, and wing-jet as a function of engine/wing/observer geometry. No wing-shielding correction, as such, is applied to the USB-flap noise since this effect is inseparately tied into the directivity of that source. Fuselage-shielding is also added as a correction to the fan, turbine, and high-lift noise sources. A correction to the high-lift noise is available as an option if the user wishes to consider any noise suppression such as treated trailing-edge surface or trailing-edge blowing. Finally, the total noise emanating from the aircraft in the direction of the observer is corrected for spherical divergence, atmospheric attenuation, extra ground attenuation, and ground reflections. The APU noise is calculated as a maximum PNL value at the observer location and added to the total PNL of the other sources. In this manner, total PNL's at any observer location on the ground relative to the aircraft may be determined.

In order to obtain noise footprints, these calculations are repeated at selected observer locations, without corrections for extra ground attenuation or ground relfections, to generate a PNL directivity for the aircraft being

investigated. Knowing the aircraft PNL noise directivity and the aircraft flight profile, EPNL contours for community noise studies were calculated. The flight profile describes aircraft distance along the runway centerline, altitude, and the angle of the wing chord relative to the ground as a function of time. Consequently, a tone-corrected PNL (PNLT) — time history and EPNL may be calculated at any observed location. Noise levels at each location are corrected for atmospheric attenuation, spherical divergence, extra ground attenuation, and ground reflection effects. To generate the desired EPNL contour, the observer sideline distance at selected distances along the runway centerline is incremented until the sideline distance to the desired EPNL is found. Thus, the EPNL contour is determined. The contour is printed out in tabular form and/or as a computer-generated plot. Contours may be calculated for either takeoff or landing conditions.

4. COMPATIBILITY STUDIES AND AIRCRAFT NOISE COMPUTATIONS

The compatibility of low noise USB nacelle installations with efficient advanced transport aircraft were investigated by conducting a detailed design feasibility study. The feasibility study was based on aircraft designs developed in the NASA short-haul studies of references 31-34. Accomplishment of the study required the following three steps:

- Selection of a suitable mission and definition of the associated baseline aircraft.
- Determination of the effects of perturbations from the baseline and selection of a final configuration
- Establishment of the design feasibility of the final configuration.

Throughout the study the basic goals of (1) cruise drag competitive with that of conventional installations, (2) satisfactory short-field characteristics, and (3) a 90 EPNdB noise footprint area of 2.59 km^2 (1 m^2) were kept in mind.

4.1 Aircraft Performance Requirements

The principal operating requirements considered in this phase of the investigation were the stage length, field length, and cruise Mach number. The nacelle drag levels were high enough to indicate that the analysis should concentrate on short-range and medium-range missions. These were selected to be 805 km (500 n.m.) and 2414 km (1500 n.m.), respectively. The design field lengths chosen were 610 m (2000 ft) for the short-haul aircraft and 1219 m (4000 ft) for the medium-haul aircraft. The design payload was set at 148 passengers, a break point above which more cabin attendants are required under FAA regulations.

4.2 Candidate Engines and Aircraft

The engines used in the analysis were the Allison PD-287-11, with a design fan pressure ratio of 1.35, and the General Electric CFM56, with a design fan pressure ratio of 1.47. The PD-287-11 is a study engine developed in the program that led to the Quiet Clean STOL Experimental Engine (QCSEE). The CFM56 is a current engine now undergoing test. A lower fan pressure ratio results in a quieter, but sometimes heavier and more expensive, aircraft and vice versa. The tradeoff between noise and cost was determined at both stage lengths by designing aircraft around each of the two engines.

Drag considerations and preliminary sensitivity studies led to the choice of nacelle configurations. The two types considered were (1) USB integrated nacelles and (2) OTW pylon-mounted configurations.

For the USB integrated nacelles, a range of different nozzle types was examined from the test results. The details of the test results are presented in reference 35. The sensitivity of a selected short-haul aircraft to the drag and weight characteristics of the different nozzle types was examined across a range of nozzle pressure ratios. Of the configurations examined, the D-duct nozzles resulted in the lowest ramp weight penalties, as shown in figure 32. It was also true that these minimum penalties were

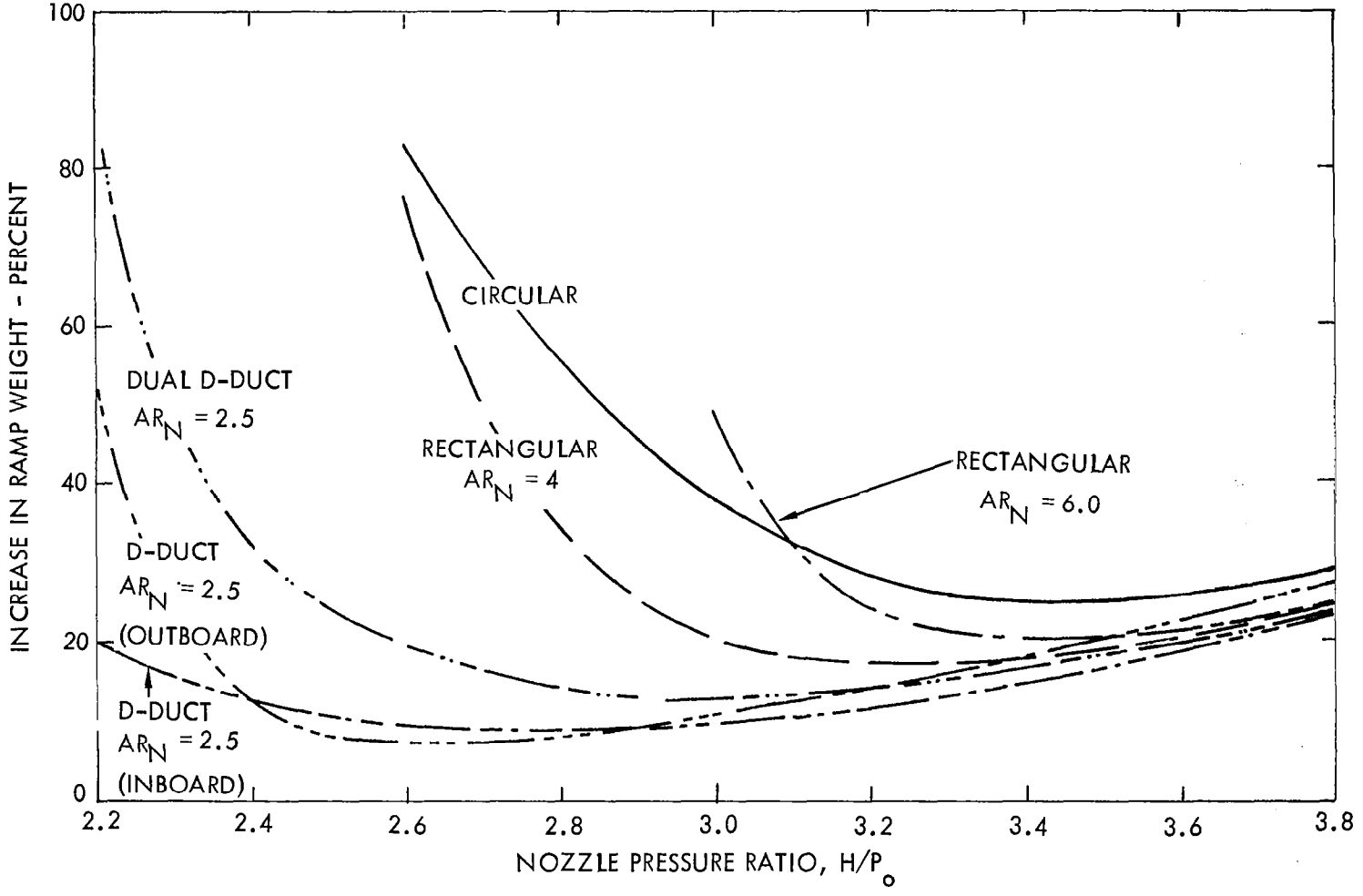

FIGURE 32. EFFECT OF NOZZLE SHAPE ON RAMP WEIGHT

(Range = 926 Km (500 n.m.). Field Length = 610 m (2000 ft.)
Baseline Weight = 62,093 KG (136,890 lb), Swept Wing, M_o = .73.)

experienced at the lowest pressure ratios tested. Thus, among the integrated nacelles, the choice of the D-duct was clear cut.

Although the drag of the pylon-mounted configurations was not measured directly under power, it was measured for the flow-through case. A comparison of the integrated D-duct versus short and long pylon-mounted nacelle configurations is shown in figure 33 for the flow-through pressure ratio. Here the short pylon shows significantly lower drag; the nacelle drag is slightly higher with the long pylon than for the integrated nacelle. The drag penalty due to power is expected to be lower for the pylon-mounted nacelles because there is no scrubbing. Based on these results, the short pylon-mounted nacelle was chosen for installation in the second study aircraft.

Since the best integrated nacelle had a higher drag level than the short pylon configuration, it was decided to employ the D-duct for the 805 km (500 n.m.) mission. It then followed that the short pylon nacelle would be used on the 2414 (1500 n.m.) mission.

Aircraft weight and cost usually increase with cruise Mach number, but it was not clear how strong the effect of Mach number would be on these aircraft. The basic combinations — short range/1.35 fan pressure ratio/integrated nacelle and medium range/1.47 fan pressure ratio/pylon-mounted nacelle — were therefore investigated at 0.70, 0.75, and 0.80 cruise Mach numbers.

The matrix of eight aircraft that evolved from the factors just discussed and was used in the analysis is shown below.

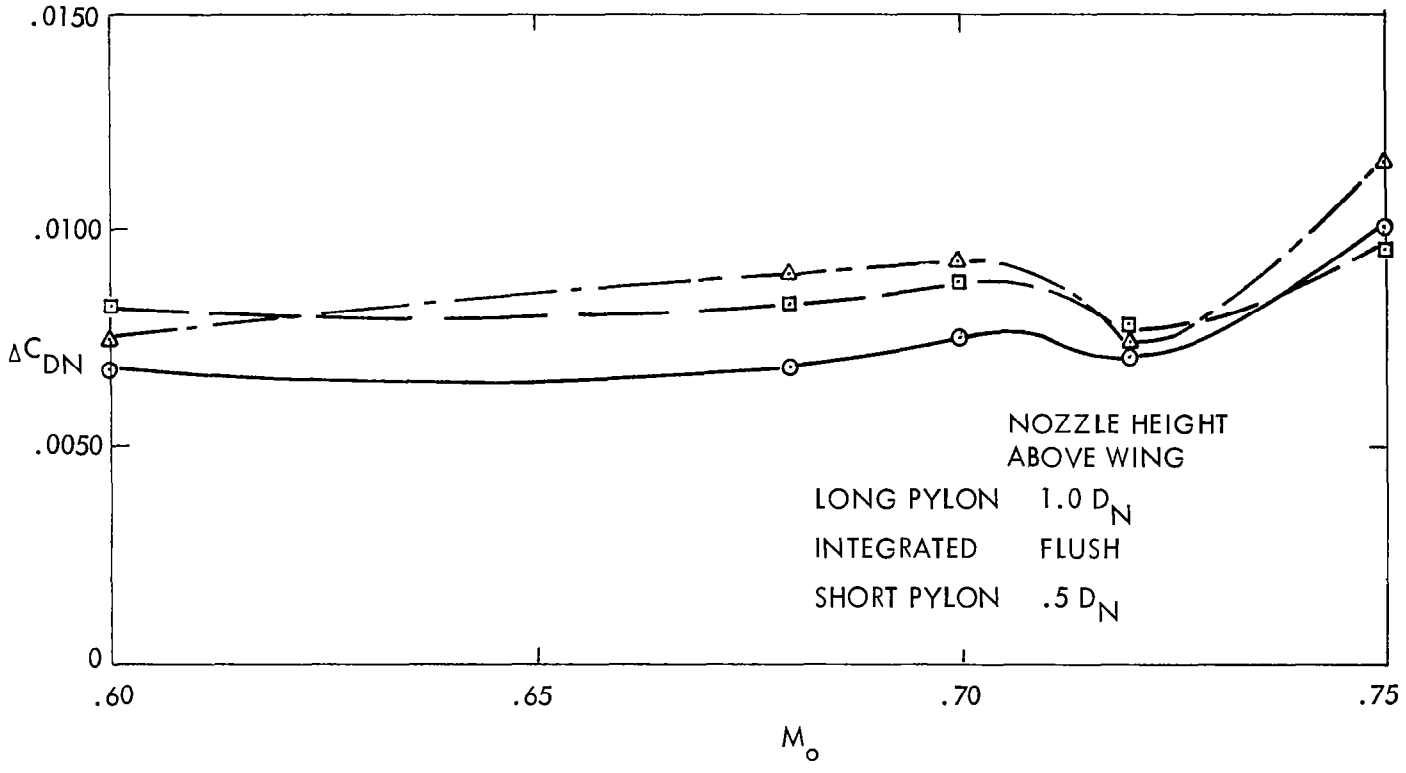

FIGURE 33. EFFECT OF PYLON ON NACELLE DRAG.

Straight Wing; C_L = .40. Circular Nozzle; H/P_o = 1.4.

Aircraft No.	1	2	3	4	5	6	7	8
No. of Passengers	148							
Stage Length, km (n.m.)	805 (500)				2414 (1500)			
Field Length, m (ft)	610 (2000)				1214 (4000)			
Fan Pressure Ratio	1.35			1.47	1.47			1.35
Nacelle Type	Integrated				Pylon Mounted			
Cruise Mach No.	0.70	0.75	0.80	0.75	0.70	0.75	0.80	0.70

4.3 Analysis

The analysis used computer programs, data bases, and experience developed during Lockheed's three-year study of short-haul transportation systems for NASA, reported in references 31 through 34. The sequence of operations was as follows:

(1) An airport performance program was used to determine the wing loading and thrust loading needed to meet the takeoff and landing field length requirements. USB high-lift system characteristics developed in the short-haul work were used. These characteristics, drawn largely from tests conducted in the Questol program, which led to the Quiet STOL Research Aircraft (QSRA) competition, are based on the use of a large flap of moderate deflection with a final segment, blown at the knee, that can be further deflected as needed. The airport performance program also provided takeoff and landing flight paths and landing thrust settings and flap settings for use in calculating noise.

(2) Aerodynamic parameters such as wing aspect ratio, sweep angle, taper ratio, thickness ratio, etc., were selected on the basis of optimization studies conducted under the short-haul transportation system contracts. Two-engine aircraft were chosen for the medium-range mission to reduce the takeoff noise footprint area. A two-engine aircraft requires more total thrust than a four-engine, but the steeper climbout angle more than compensates for the added thrust when footprint area is the criterion. A two-engine design is impractical, however, at the short-field length associated with the short-range mission. Highly deflected landing flaps are needed to get the aircraft

into the short field, and their drag is such that the installed thrust required to handle an engine-out go-around becomes excessive. Four-engine aircraft were therefore used for the short-haul mission.

(3) The aircraft thus defined were run through their missions in the general aircraft sizing program (GASP), with the performance curves of the selected engine, to determine the component sizes and weights needed to meet the requirements. GASP converges to the required combination of engine size, wing area, and mission fuel, calculating the drag weight, and size of each major component and system of the aircraft as it does. It also calculates procurement and operating costs. The cost equations were not updated for the present analysis, but are indicative of relative magnitudes.

Nacelle drag coefficients were input to GASP as a function of aircraft lift coefficient and were based on the design nozzle pressure ratios of the study engines. Drag values used were actual test data from the USB cruise performance program reported in reference 35. They were modified for scale effect and corrected for the difference in wing aspect ratio between the test model and the full-scale study aircraft.

(4) The noise levels and footprint areas of the resulting aircraft were calculated using the noise prediction program described in Section 3 of this report.

Results. The salient characteristics of the eight aircraft analyzed in the baseline selection phase are listed in Table 1. Cost, weight, and noise comparisons are presented in figures 34 through 36. It can be seen in figure 34 that neither procurement cost nor direct operating cost (DOC) are strongly affected by the mission variables; a factor of 1.2 covers the spread between the highest and lowest values of both costs.

Ramp weight shows more overall variation, primarily because the medium-haul mission requires considerably more fuel, and thus a larger aircraft, than the short-haul mission. One interesting feature of the weight comparison is that aircraft 2, designed for Mach 0.75, is slightly lighter than aircraft

TABLE 1. USB STUDY AIRCRAFT

AIRCRAFT NO. →	1	2	3	4	5	6	7	8
MISSION								
NO. OF PASSENGERS	148							
STAGE LENGTH, Km (N.M.)	927 (500)				2780 (1500)			
FIELD LENGTH, m (Ft)	610 (2000)				1219 (4000)			
CRUISE MACH NO.	0.70	0.75	0.80	0.75	0.70	0.75	0.80	0.70
CRUISE ALTITUDE, m (Ft)	9144 (30000)							
PROPULSION SYSTEM								
NOZZLE SHAPE	D (SEMICIRCULAR)				CIRCULAR			
NACELLE TYPE	BLENDED				PYLON-MOUNTED			
NO. OF ENGINES	4				2			
FAN PRESSURE RATIO	1.35			1.47	1.47			1.35
RATED THRUST, N (Lb)	79993 (17984)	83200 (18705)	90753 (20403)	101307 (22776)	160978 (36191)	160946 (36184)	183395 (41231)	203447 (45739)
NACELLE DIAMETER, m (Ft)	2.05 (6.72)	2.09 (6.85)	2.18 (7.15)	2.14 (7.02)	2.70 (8.85)	2.70 (8.85)	2.88 (9.45)	3.26 (10.71)
AIRCRAFT								
RAMP WEIGHT, Kg (Lb)	66266 (146116)	66067 (145678)	68765 (151626)	72563 (160001)	78893 (173959)	80728 (178006)	85544 (188625)	83511 (184141)
WING AREA, m^2 (Ft^2)	186.1 (2003)	169.8 (1828)	159.0 (1711)	199.9 (2152)	172.9 (1861)	185.3 (1995)	169.9 (1829)	204.1 (2197)
WING LOADING, Kg/m^2 (Lb/Ft^2)	354 (72.5)	387 (79.2)	430 (88.0)	359 (73.6)	453 (92.8)	433 (88.6)	499 (102.3)	407 (83.3)
THRUST-TO-WEIGHT RATIO	0.460	0.480	0.503	0.536	0.391	0.382	0.410	0.464
ASPECT RATIO	10.0				7.73			
SWEEP ANGLE, 0.25c, DEGREES	20							
TAPER RATIO	0.3							
THICKNESS RATIO, AVG.	0.141		0.123	0.141	0.141		0.123	0.141
CRUISE DATA								
F_N/MAX CRUISE	1.000			0.600	0.890	0.975	1.000	1.000
C_L	0.325	0.310	0.304	0.291	0.415	0.344	0.350	0.372
C_D	0.0273	0.0256	0.0248	0.0204	0.0335	0.0284	0.0303	0.0317
L_D	11.9	12.1	12.3	14.2	12.4	12.1	11.5	11.7
NACELLE C_D, TOTAL	0.0104	0.0096	0.0096	0.0050	0.0116	0.0096	0.0120	0.0132
TAKEOFF AND LANDING DATA								
CLIMBOUT ANGLE	14.2	14.8	15.5	18.3	11.4	11.2	11.7	14.0
CLIMBOUT SPEED, Km/Hr (Kt)	184.7 (99.6)	184.7 (99.6)	185.4 (100.0)	187.6 (101.2)	250.8 (135.3)	250.5 (135.1)	252.0 (135.9)	228.8 (123.4)
APPROACH ANGLE, DEGREES	5.9	5.9	5.9	6.1	3.8	3.8	3.8	3.6
APPROACH SPEED, Km/Hr (Kt)	160.7 (86.7)	160.2 (86.4)	159.4 (86.0)	153.9 (83.0)	250.5 (135.1)	251.6 (135.7)	247.9 (133.7)	262.9 (141.8)
RATE OF SINK, m/S (Ft/Min)	4.57 (900)							
APPROACH F_N/TAKEOFF F_N	0.38	0.42	0.47	0.45	0.20	0.19	0.24	0.12
COSTS (1972 $)								
ENGINES	$3.59M	$3.64M	$3.75M	$2.83M	$2.08M	$2.08M	$2.18M	$3.11M
COMPLETE AIRCRAFT	$10.58M	$10.82M	$11.34M	$10.36M	$9.49M	$9.80M	$10.44M	$11.15M
DOC, 2 x 1972 FUEL PRICE (23¢/Gal), ¢/SEAT-S.M.	2.33	2.26	2.27	2.27	1.74	1.72	1.76	1.94
DOC, 4 x 1972 FUEL PRICE (46¢/Gal), ¢/SEAT-S.M.	2.94	2.36	2.89	2.99	2.32	2.32	2.40	2.52
NOISE								
TAKEOFF FOOTPRINT, 90 EPNdB, Km^2 ($S.M.^2$)	2.83 (1.09)	3.03 (1.17)	3.47 (1.34)	9.90 (3.82)	15.20 (5.87)	14.66 (5.66)	17.35 (6.70)	4.07 (1.57)
TAKEOFF FLYOVER AT 6.49 Km (3.5 N.M), EPNdB	83.4	83.4	83.7	88.6	95.8	95.6	96.5	85.6
TAKEOFF, MAXIMUM AT 152.4 M (500 Ft), SIDELINE, EPNdB	99.1	99.1	100.3	106.3	106.4	106.2	107.4	101.4
LANDING FOOTPRINT, 90 EPNdB, Km^2 ($S.M.^2$)	0.11 (0.04)	0.18 (0.07)	0.36 (0.14)	1.14 (0.44)	0.11 (0.04)	0.11 (0.04)	0.16 (0.06)	0.11 (0.04)
LANDING FLYOVER AT 1.86 Km (1 N.M.), EPNdB	86.8	88.7	91.1	95.0	86.1	85.9	88.5	85.5
TOTAL FOOTPRINT, 90 EPNdB, Km^2 ($S.M.^2$)	2.94 (1.13)	3.21 (1.24)	3.83 (1.48)	11.04 (4.26)	15.31 (5.91)	14.77 (5.70)	17.51 (6.76)	4.18 (1.61)

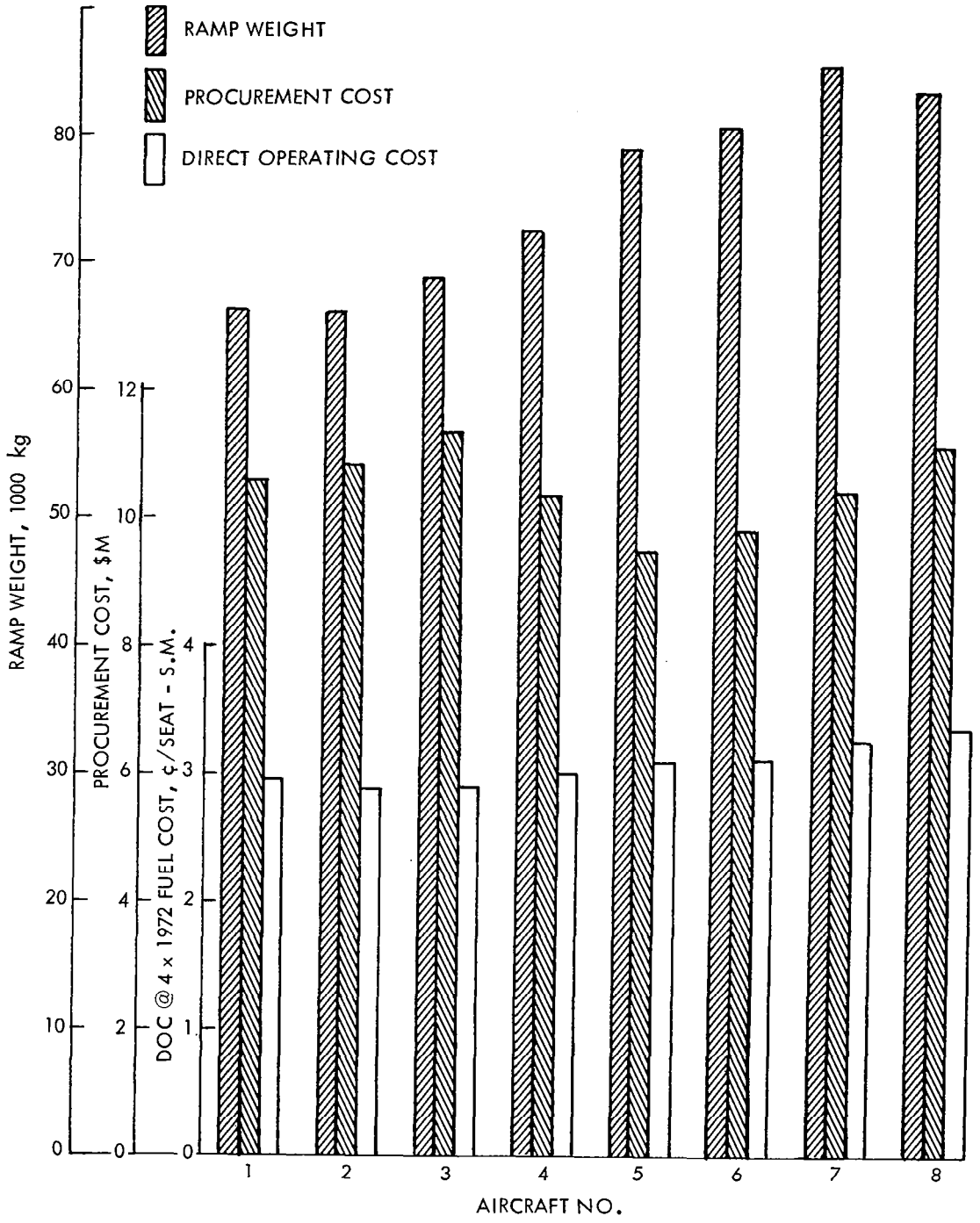

FIGURE 34. WEIGHT AND COST - USB STUDY AIRCRAFT

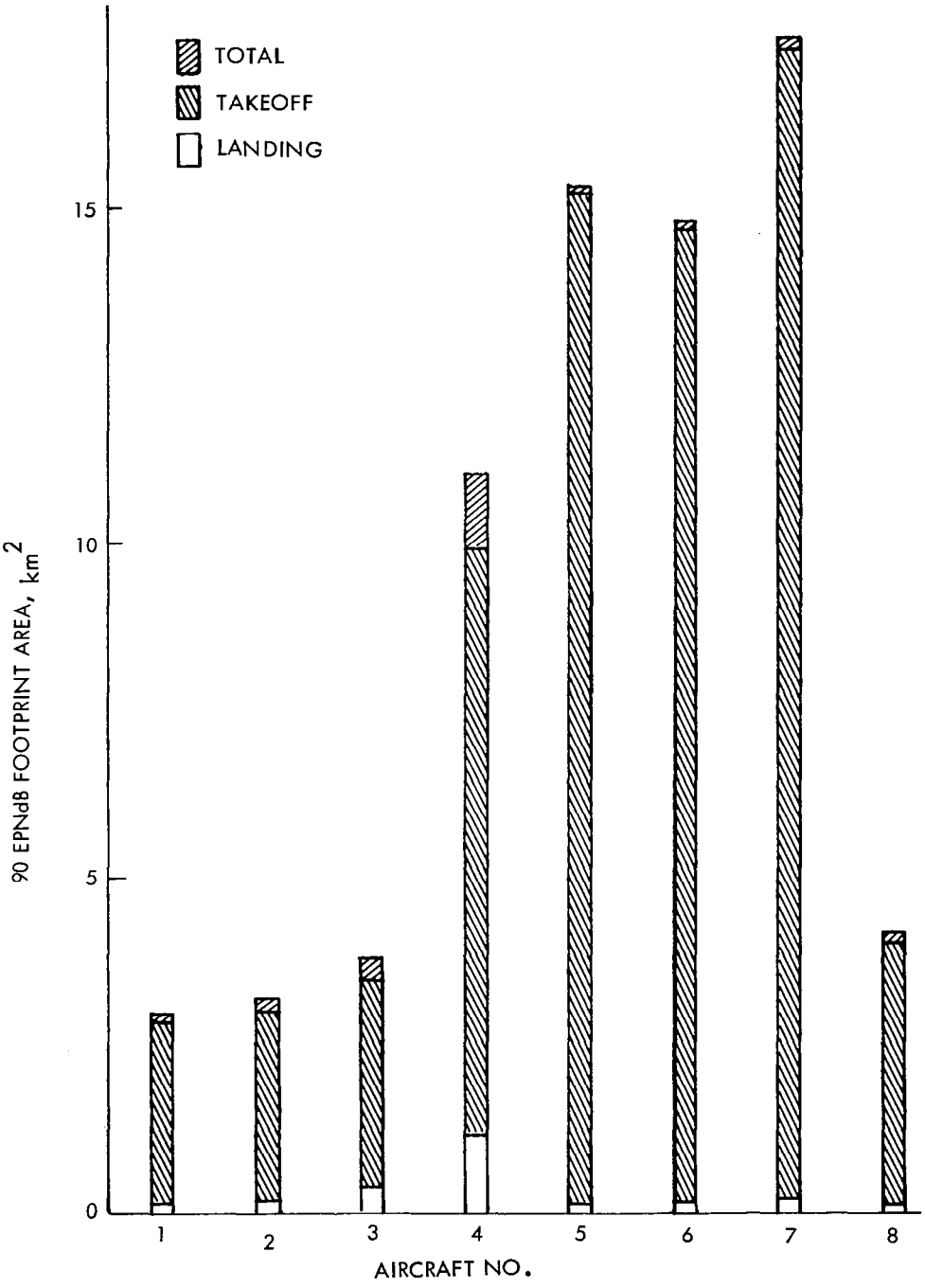

FIGURE 35. NOISE FOOTPRINT AREAS, USB STUDY AIRCRAFT

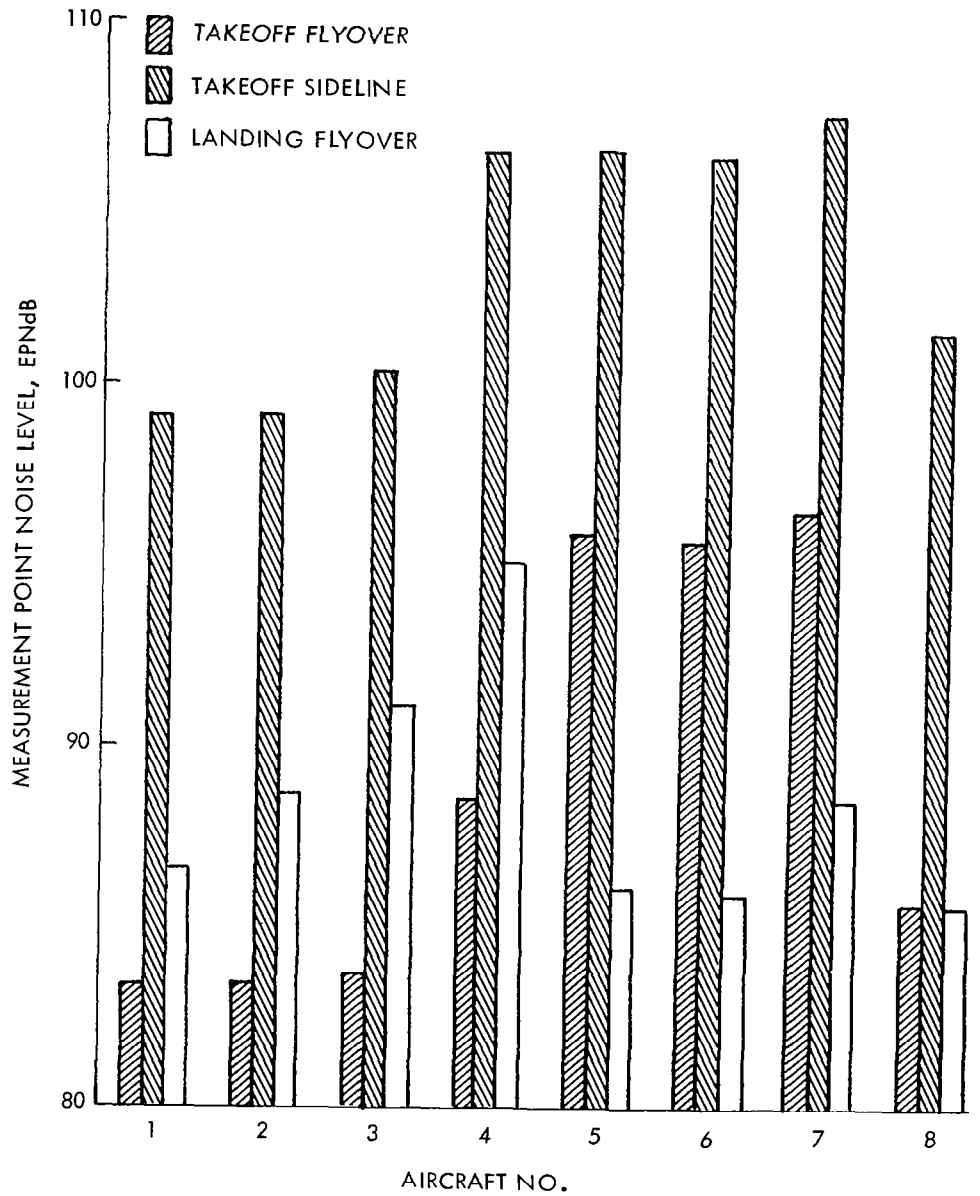

FIGURE 36. MEASUREMENT POINT NOISE LEVELS, USB STUDY AIRCRAFT

1, which is designed for Mach 0.70. There are two reasons for this. First, the field length requirement is so stringent that the engine size is set by takeoff requirements; as it turns out, the resulting engine size is better matched to Mach 0.75 than to Mach 0.70 cruise. Second, nacelle drag is very sensitive to lift coefficient at the lower wing loadings. Since the cruise lift coefficient for the Mach 0.75 airplane is slightly lower than for Mach 0.70, the drag coefficient is also lower. It is possible that further optimization of the wing would eliminate the weight minimum at 0.75 cruise Mach number.

Noise shows the largest variation among the parameters shown. Takeoff noise levels are dictated primarily by the choice of engine, as can be seen from the following table.

Fan Pressure Ratio	1.35	1.47
Aircraft Nos.	1-3,8	4-7
Range of Values -		
Takeoff Footprint, Km^2	3-4	10-17
Takeoff Flyover, EPNdB	83-86	89-96
Takeoff Sideline, EPNdB	99-101	106-107

Landing noise is more a function of field length: The shorter field requires highly deflected flaps and substantial thrust settings (38-46%) during approach, while the flap deflections are much lower and the thrust settings are only 12-24% with the longer field. Thus, the 1.47 fan pressure ratio aircraft at the shorter field length (aircraft 4) has the highest landing approach flyover noise (95 EPNdB) and the only appreciable landing footprints (see figure 36). Otherwise, the landing footprints are negligible and the approach flyover noise levels are all in the range of 91-95 EPNdB.

The effect of design cruise Mach number is fairly small at either stage length. Weight, cost and noise generally increase with Mach number along an accelerating curve, with little difference between 0.70 and 0.75 Mach number and somewhat more increase at 0.80 Mach number.

Baseline Aircraft Selection. The 1.47 fan pressure ratio aircraft (No. 4 through 7) were ruled out as baselines because of their noise. It appears from figure 35 that aircraft with a fan pressure ratio of about 1.35 (Nos. 1, 2, 3 and 8) is required to meet the 90 EPNdB total footprint area goal of 2.59 km^2 (1 m^2).

The study showed that satisfactory aircraft could be designed with true USB nacelles (aircraft No. 1-3). It was therefore decided to eliminate aircraft 8 with its pylon-mounted nacelle. This left a choice to be made between the three cruise Mach numbers represented by aircraft 1-3. The differences between aircraft 2, at 0.75 Mach number and aircraft 1, at 0.70 Mach number are minor. Aircraft 3, at 0.80 Mach number is somewhat poorer than the other two on all counts, and the time saved by its extra speed is small at the 805 km (500 n.m.) range - four minutes, compared to the 0.75 Mach number, if the full 805 km is covered at design cruise speed. Aircraft 2 was therefore selected as the baseline design.

4.4 Perturbation Studies

With a baseline design selected, the effects of perturbations of aircraft variables which affect performance and noise were investigated. The cruise performance parameters varied with nozzle boattail angle, aspect ratio, relative size, and discharge position. Parameters affecting noise that were varied were nozzle aspect ratio and impingement angle on the wing, flap extension, deflection, and radius of curvature, fan duct noise treatment, and total noise source strength. Each parameter was varied individually while holding the others constant. In addition, for the noise studies, the effects of a long-chord flap combined with changes in nozzle aspect ratio and fan duct noise treatment were determined. Only takeoff footprint area and takeoff measurement point flyover noise were considered in this study.

Cruise Performance. The effects of the various nozzle geometric parameters as determined from force tests were examined across a wide range of thrust coefficients. Performance data for the straight and swept wings were evaluated at the appropriate drag divergence Mach numbers of 0.68 and

and 0.73 respectively. The criterion for evaluation was total nacelle interference drag, $\Delta C_{D_{NIT}}$, which is the sum of the nacelle aerodynamic drag, scrubbing drag, and vectoring drag, less nacelle skin friction drag.

Results from the evaluation of boattail angle effects are presented in figure 37(a) for thrust coefficients (C_μ's) ranging from 0.04 to 0.12. The approximate corresponding range of pressure ratio is 1.6 to 2.9. Two distinctly different trends are apparent. In the subcritical range of pressure-ratios, on the other hand, a neatly defined optimum occurs at around 15-18° and the drag increments rise sharply above those values. Since most transports cruise in the critical-to-supercritical range, good design practice will call for holding boattail angles to less than 20°.

Nacelle drag increments as a function of nozzle pressure ratio are shown in figure 37(b). Except for the lowest pressure ratio examined, a definite preference was indicated for the D-duct (AR = 2.5). At the pressure ratios of greatest interest, i.e. 1.9 to 2.6, a 22 to 30% drag reduction is shown relative to the circular nozzle. Next to the D-duct, the nozzle with AR = 6 appeared to have the lowest drag increment, although it is not clear why this is so. The advantage shown over an aspect ratio of 4 is relatively small.

To determine the effect of size, two nozzles which were identical except for size were selected from the cruise performance program matrix. These were nozzle N4, with $c^2/A_N = 24$, and nozzle N12, with $c^2/A_N = 48$, where c is the wing chord and A_N is the nozzle area. (These nozzles and other details are described in reference 35). Evaluation of the drag of these nozzles at various pressure ratios resulted in the curves shown in figure 37(c). The data show that as the nacelle gets smaller, the drag coefficient based on nacelle frontal area goes up, which is probably related to the effect of the nacelle on spanloading and thus on wing efficiency. Although the basic drag of the nacelle is a function of nacelle cross-sectional area, the span affected varies with nacelle diameter. Thus the change in wing efficiency is really a function of the square root of the cross-sectional area.

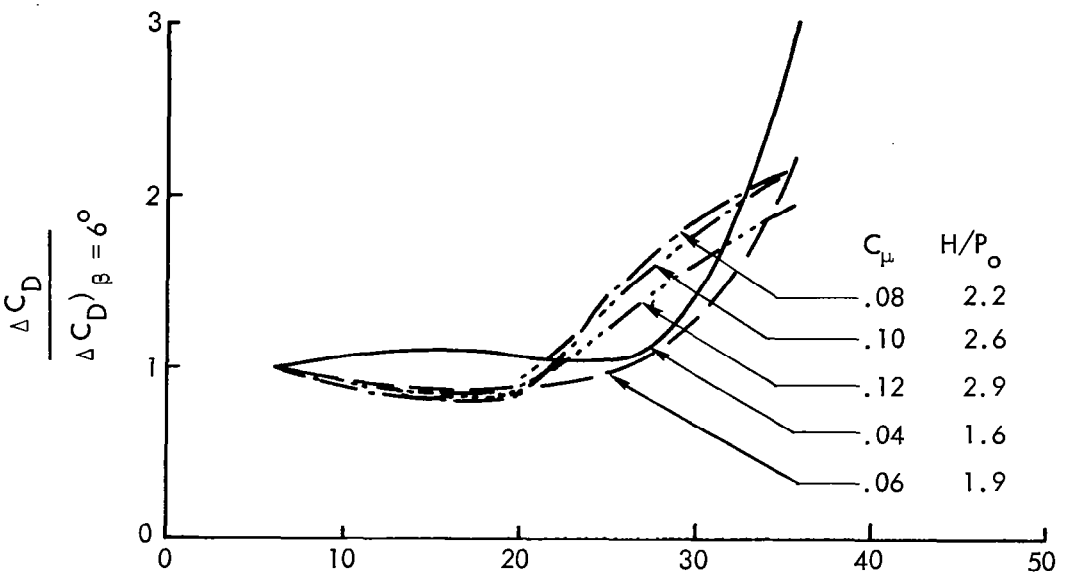

(a) EFFECT OF BOATTAIL ANGLE. M_o = .68; C_{L_A} = .40; x/c = .35.

NOTE: ΔC_D IS $\Delta C_{D_{NIT}}$

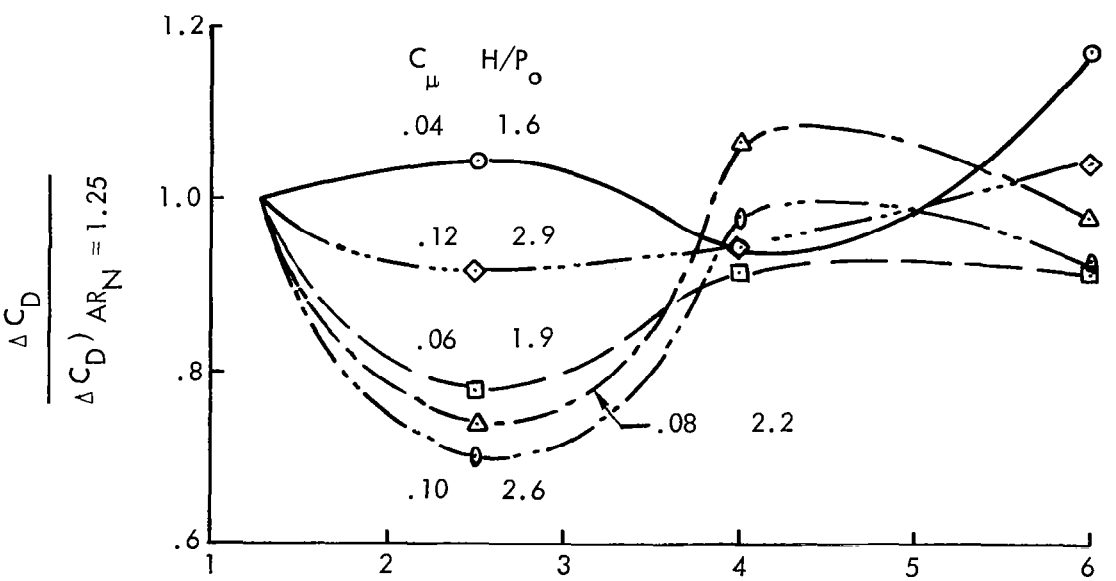

(b) EFFECT OF NOZZLE ASPECT RATIO

C_{L_A} = .40; X/C = .35

FIGURE 37. NACELLE DRAG SENSITIVITIES

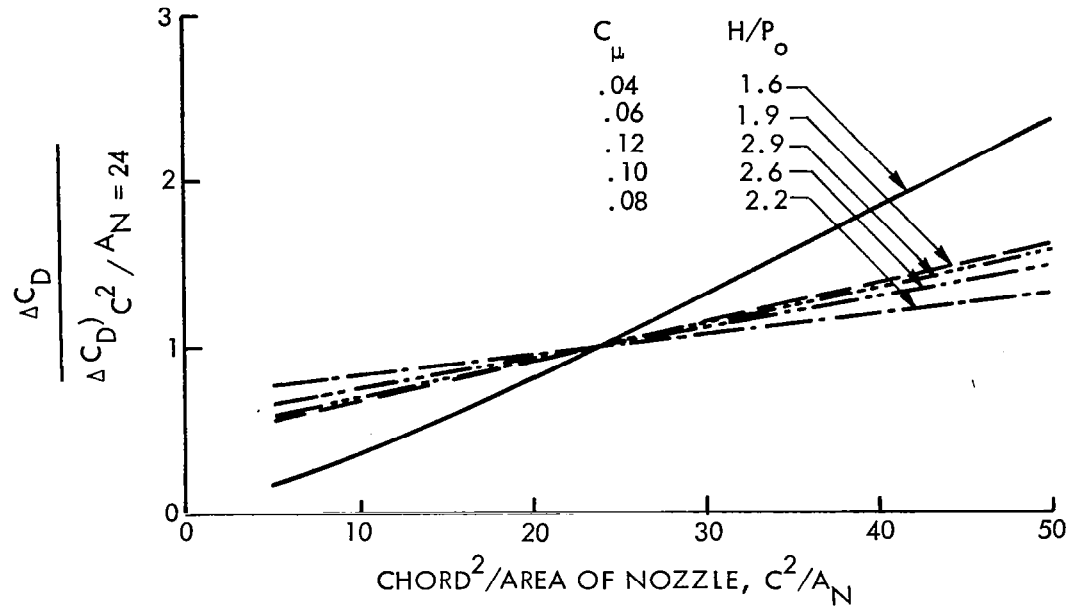

(c) EFFECT OF NOZZLE RELATIVE SIZE.

NOTE: ΔC_D IS $\Delta C_{D_{NIT}}$ C_{L_A} = .40; X/C = .35

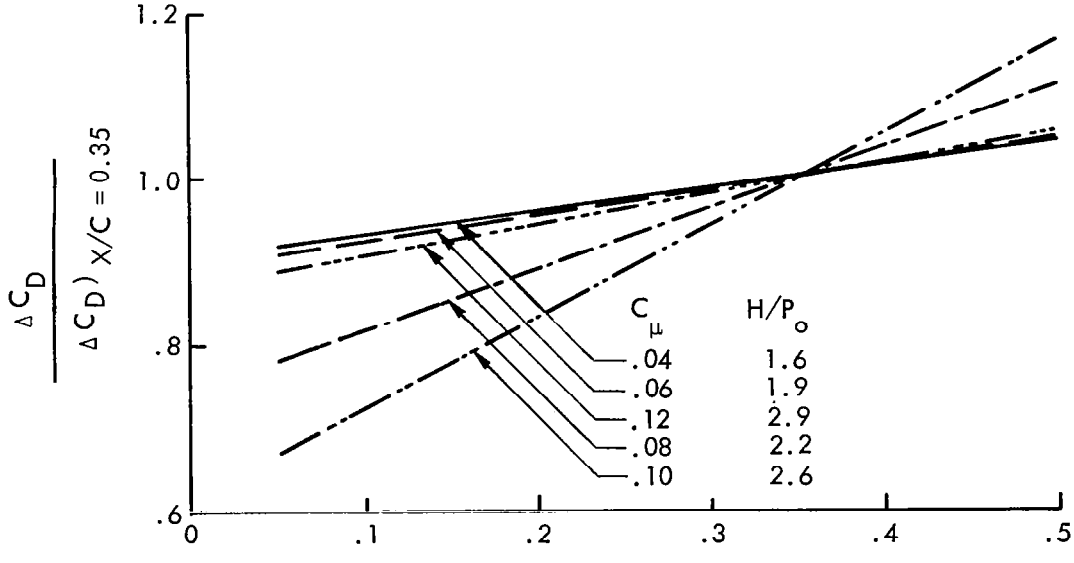

(d) EFFECT OF NOZZLE EXIT POSITION, C_{L_A} = .40

FIGURE 37. CONCLUDED

The change in nacelle incremental drag with chordwise position is presented in figure 37(d), which is based on results obtained with circular nozzles with discharges at different chordwise positions. Drag was shown to be consistently reduced by forward movement of the nacelles. This result is highly credible since it is the same trend as has been obtained for conventional under-the-wing installations. The favorable trend is due to the improvement in nacelle-wing area distribution as the nacelle is moved forward.

As had been anticipated, the perturbation studies of the basic nozzle geometric variables did not result in any changes of these parameters from their baseline values. A boattail angle of 16°, previously selected for the baseline, is seen in figure 37(a) to be near optimum. The choice of a D-duct nozzle is unassailable from a performance standpoint, based on the nozzle aspect ratio effects of figure 37(b).

Figure 37(c) indicates that larger nozzles provide lower drag penalties. This would mean that for the same installed thrust, two large engines would be better than four small ones. For an aircraft that must operate from a 2000-foot field, however, switching to a twin-engine design would result in a considerable increase in required installation thrust capability, more than negating the potential drag saving. The value of c^2/A_N employed on the baseline is approximately 14, which, as is seen in figure 37(c), results in a significantly lower drag coefficient than the reference (intermediate) nacelle test value of 24.

In the case of nozzle exit position, figure 37(d) shows that nacelle drag is reduced as the nacelle is moved forward to where x/c approaches zero. The tradeoff here is against weight and scrubbing drag, and the choice of $x/c = 0.35$ was made based on extensive work performed for the QSRA effort, which indicated this was a near-optimum value.

Noise Levels. Noise effects were determined from the noise prediction model (described in the previous section) alone, without resizing the aircraft or recalculating its airport performance. For most variables this procedure is believed to yield results that are either approximately correct or

conservative (higher than the true noise levels). Incorporating size and flight path effects would yield higher noise levels only in the case of the nozzle aspect ratio variation; the higher aspect ratios of the nozzle variants are associated with higher cruise drag and thus with less noise reduction when size and flight path effects are considered.

Size and flight path effects in the other cases are generally either favorable (especially with the long-chord flap) or small. Greater flap deflection could have either adverse or favorable indirect effects on noise, depending on what other changes were made in the high-lift system to hold the field length constant.

The results are shown in figure 38, in which takeoff footprint area at 90 EPNdB is plotted against takeoff flyover noise level at the 6.49 km (3.5 n.m.) measurement point. The baseline aircraft has a 90 EPNdB footprint area of 3.03 km (1.17 m^2) and a flyover noise level of 83.4 EPNdB. The goal is a total footprint area of 2.59 km^2 (1 m^2); allowing 0.11 km^2 for the landing footprint, the takeoff footprint goal becomes 2.48 km^2. Changes in flap radius of curvature, flap deflection, nozzle impingement angle, and fan duct noise attenuation cause essentially no change in the baseline noise values. The points representing these variations are grouped near the baseline point. However, the other variables – nozzle aspect ratio increase, noise source strength reduction, and flap extension – are quite effective in reducing noise. Aircraft incorporating these modifications are indicated to be capable of at least meeting the noise goal. These variables are discussed below.

Nozzle Aspect Ratio. Flat rectangular nozzles are shown to reduce markedly both footprint area and flyover noise. As is noted above, however, they have higher drags than the baseline semicircular D nozzle, and the effects of the drag increase on aircraft size and flight path are not included in the analysis. The favorable effects of increased nozzle aspect ratio on noise would be diminished if size and flight path effects were considered.

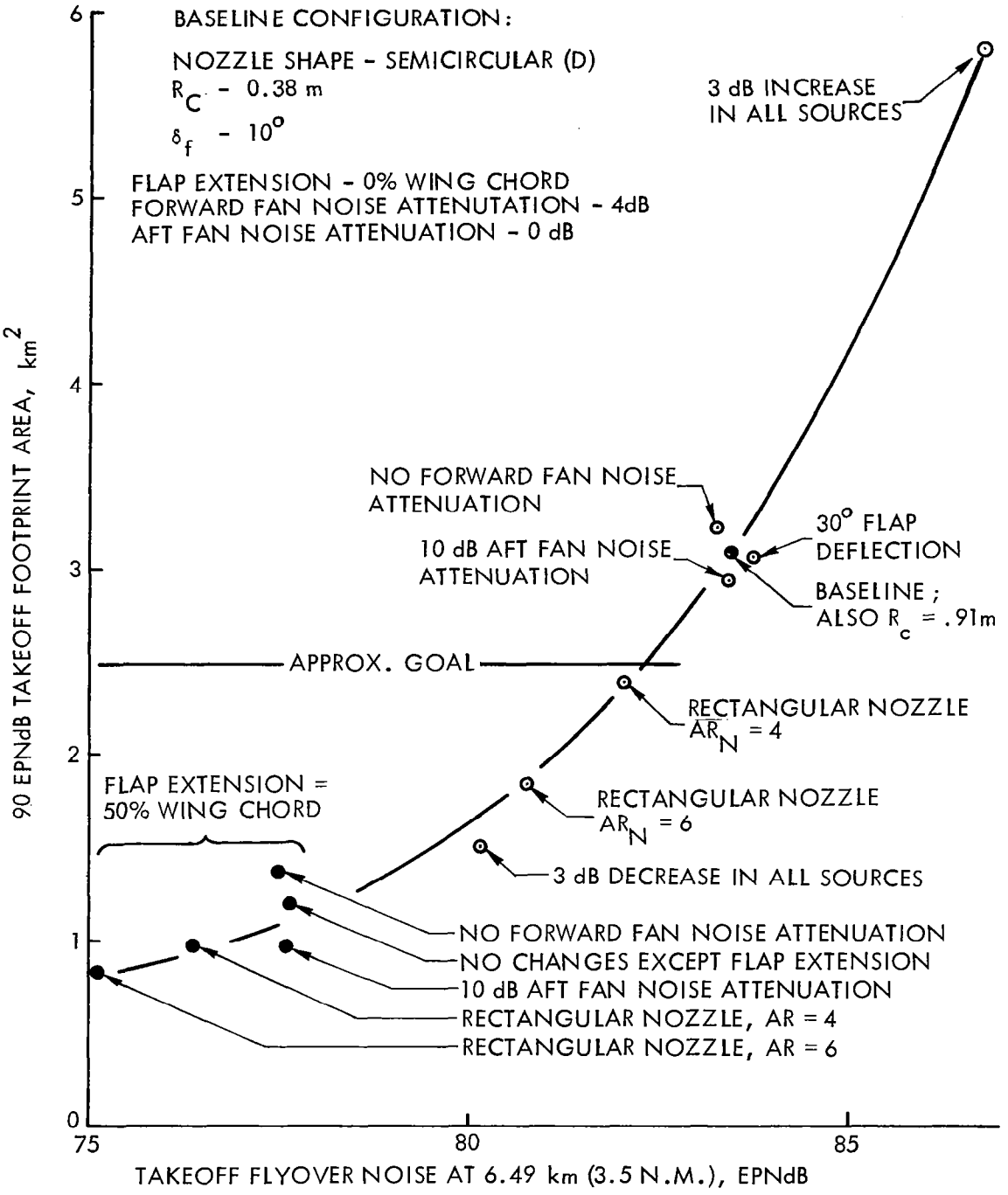

FIGURE 38. EFFECTS OF PERTURBATIONS FROM BASELINE AIRCRAFT ON TAKEOFF NOISE. NO CHANGE IN AIRCRAFT SIZE OR FLIGHT PATH.

Since the noise goal is achievable with the D nozzle, nozzle aspect ratio variations were not pursued further. If the nozzle were to be changed, however, the aspect ratio 6 design would be preferred to the aspect ratio 4. Both configurations have more drag than the D nozzle, but aspect ratio 6 has slightly less drag than aspect ratio 4 and is considerably quieter.

High-Lift System Noise Reduction. The noise generated by a USB high-lift system can be reduced by modifying the flow conditions at the flap trailing edge. Although preliminary results reported in reference 36 indicate reductions of up to 10 dB, attempts to repeat these results in the present program were unsuccessful; the OASPL reductions achieved were about 2 dB with passive treatment of the flap surface and about 5 dB with trailing edge blowing (reference 1).

The effect of an assumed 3 dB decrease is shown in figure 38. (For convenience in using the prediction program the decrease was applied to all sources but the effect is essentially the same as applying it to high-lift system noise alone, as high-lift system noise is the only significant contributor to the noise of the baseline aircraft.) The effect is to reduce the takeoff flyover noise by slightly more than 3 EPNdB and to cut the takeoff footprint area in half. The effects of flap treatment on aircraft size and performance and thus on noise should be considered in a more complete analysis but such effects are expected to be small. Surface treatments would affect only takeoff and landing, being covered when the flaps are retracted. Blowing would be off at cruise and is already included in the baseline flap system.

Flap Extension. As is discussed in Section 3 of this volume, extending the flap chord is the most effective way to reduce noise. The baseline flap, described earlier, deflects 20° over most of its chord, with a final blown segment that deflects further. There is no increase in chord when the flap is deployed. By changing to an unslotted Fowler flap, with the segments sliding back on tracks to extend the basic wing chord by 50%, high-lift system noise is reduced enough to lower the flyover noise from 83.4 EPNdB to 77.6 EPNdB and the 90 EPNdB takeoff footprint area from 3.0 km^2 to 1.2 km^2. These reductions do not include the effects of the increased lifting area on

the climbout angle, which would cause further decreases in both of the noise parameters.

In view of the large reductions achieved by extending the flap, this perturbation was combined with changes in fan duct noise treatment and in nozzle aspect ratio. The results, plotted as solid symbols at the left in figure 38, are similar to those obtained with the baseline flap. Fan duct treatment has somewhat more effect because high-lift system noise is reduced, but fan noise is still unimportant. Increasing the nozzle aspect ratio is less beneficial than with the baseline flap because the noise levels are already low and further improvements yield diminishing returns.

4.5 Final Design

The selected final design, shown in figure 39, is the same as the baseline, aircraft 2 of Table 1, in most respects. It is a high-wing four-engine aircraft designed for a passenger capacity of 148, field length of 610 m (2000 ft), stage length of 927 km (500 n.m.), and cruise Mach number of 0.75. The ramp weight is 66,067 kg (145, 678 lb.) and the wing area is 170 m^2 (1828 ft^2), for a wing loading of 387 kg/m^2 (79.2 psf). The engines are Allison PD-287-11's scaled to a takeoff rated thrust of 83,200 N (18,705 lb.), giving an installed thrust-to-weight ratio of 0.48. Other features and characteristics are shown in Table 1, and figure 39.

The initial cruise lift coefficient for the final design is 0.31, which reflects a relatively low wing loading. The associated drag coefficient is 0.0256, resulting in a cruise lift/drag ratio of 12.1. The total nacelle drag coefficient is 0.0096. The approach speed is 160 km/hr (86 kn) while climbout speed is 185 km/hr (100 kn).

In accordance with earlier discussion, the nacelle has a D nozzle located at 35% chord, with a boattail angle of 16°. Extended-chord flaps are used to get the noise benefit of the increased flow length from the nozzle to the flap trailing edge, and the flap internal blowing system is deleted. The aft fan duct noise treatment is deleted, leaving the fan duct untreated

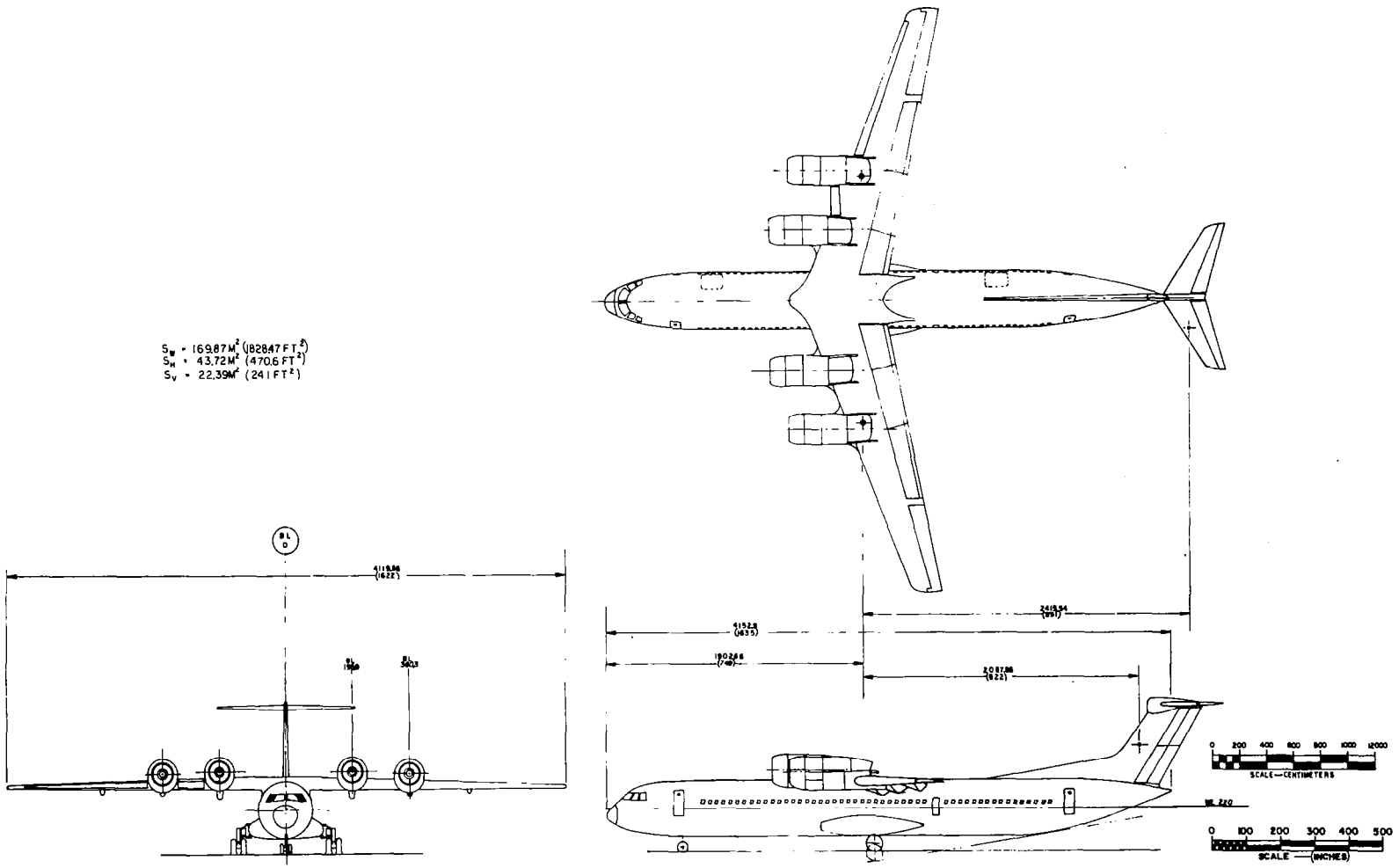

FIGURE 39. GENERAL ARRANGEMENT, FINAL DESIGN AIRCRAFT.

forward and aft, although there is provision to incorporate treatment in both areas if it is found to be desirable.

Nacelle Design. The propulsion and high-lift system installation for the outboard position is shown in figure 40. Installation design details are discussed in the following paragraphs.

Inlet. The fan intake is a standard short-duct arrangement which extends roughly one-half nacelle diameter forward of the fan face. A generous lip thickness is employed to facilitate efficient inflow at high angles of attack. The cowl is circular with the exception of the lower lobe, which is slightly elliptical to provide space for the engine accessory package.

The inlet leading edge and the internal lip downstream to the throat are protected with an evaporative anti-icing system, which employs aluminum skins in conjunction with overheat detectors. Downstream of the throat, provision is made for acoustical treatment of the inlet duct to attenuate forward radiated flap noise.

The inlet-forebody assembly is supported by and attached to the front flange of the engine fan case. It is considered to be a component of the quick engine change unit (QECU), although its overhaul schedule is based on airframe time-between-overhauls (TBO) rather than engine TBO.

Fan Case Cowling. The fan case cowling is divided into upper and lower segments. The lower segment can be opened by unlatching the lower center seam and is hinged at or just below the engine horizontal centerline for quick access to the engine reduction gear case and accessories. The upper half is attached to the fan case flanges and is removable for engine access or removal.

Fan Duct and Nacelle Structure. The upper fan duct is integrated into the nacelle by two heavy main rings and carries the engine loads into the wing box skins with a pin attachment on the upper surface and by skate angles on the lower surface. A monocoque shell, which incorporates the front and

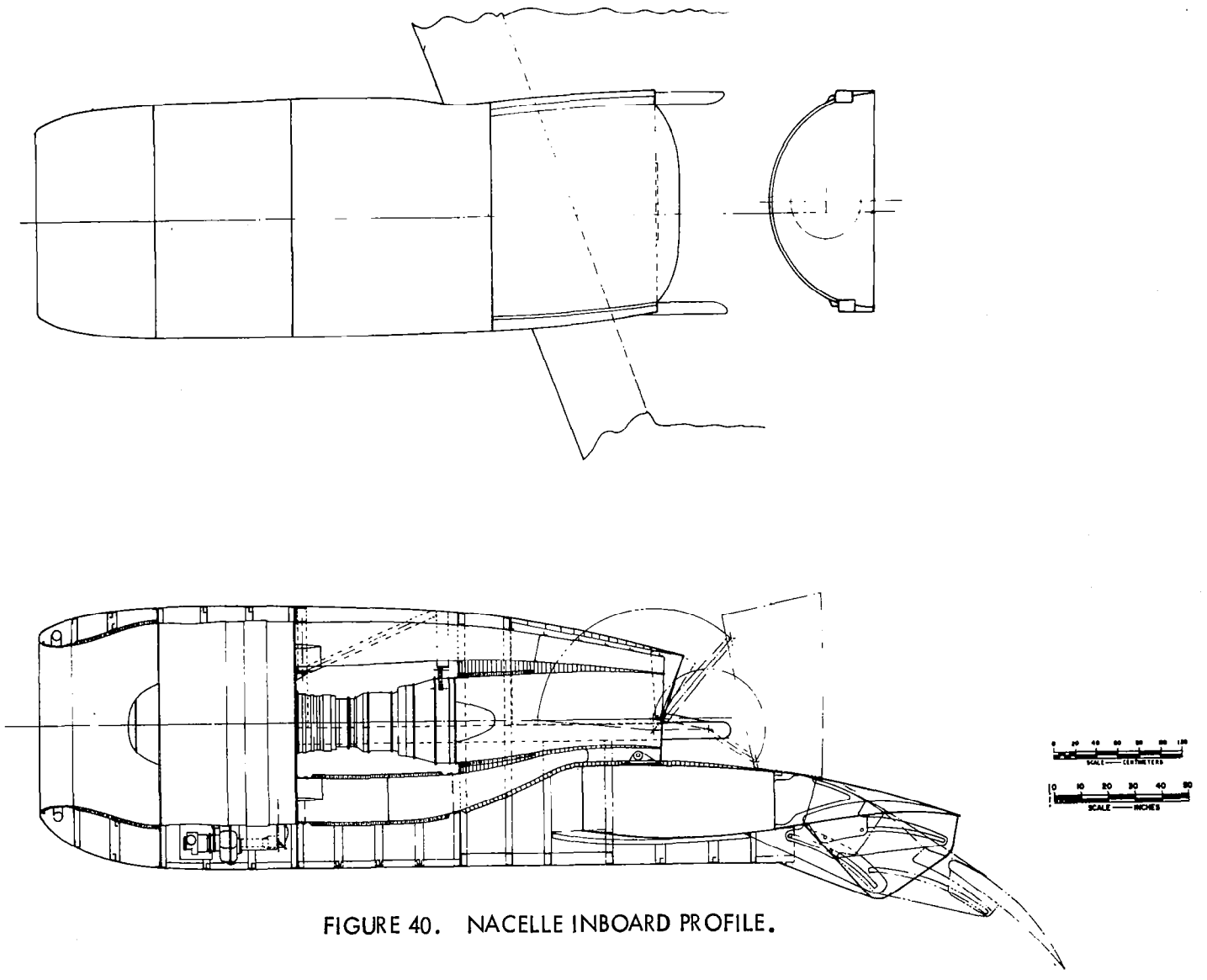

FIGURE 40. NACELLE INBOARD PROFILE.

rear engine mounts is thereby effected. This type of construction allows the engine to be changed in the conventional manner by lowering it onto a transportation trailer, either with AGE attached to the nacelle or with an elevator on the ground cart. The inner surface of the fan duct can be acoustically treated to minimize aft radiated fan noise.

Thrust Reverser. The rear upper external contour of the nacelle is formed by the outer surface of the target thrust reverser door. The inner surface of this door is constructed of high-temperature material to maintain structural strength and rigidity during its short, but high-temperature, duty cycle. Extension or retraction of the door on its four-bar linkage is accomplished hydraulically with the movable hinge points describing the arcs illustrated in figure 40. The total jet, both primary and secondary, is deflected forward and upward, providing a reverse force plus a downward force on the aircraft, making its brakes more effective. As is also illustrated in the figure, there is an articulated eyebrow-shaped section on the aft lip of the thrust reverser which can be extended to exert a downward force on the discharging jet and thereby assure its attachment to the upper surface of the wing and flap. The deflector would be employed whenever high lift coefficients are required, as during takeoff and landing.

A pair of stangs extend aft of the nozzle from along the sides to provide fixed hinge points for the aft bars on the door linkage. The stangs are located several boundary layer heights above the wing surface and outside the jet efflux. Because of the venting thus provided, their interference with the local flow patterns is expected to be minimal.

Nozzle. Separation of the fan and primary duct flow streams is maintained right up to the nozzle discharge in order to minimize flow suppression and other interaction effects. The primary nozzle is slightly S-shaped in the side view, but a circular cross-section is maintained throughout. It is constructed of steel honeycomb with the forward inner portion fabricated to include a perforated face sheet to attenuate turbine noise. The outer fan duct above the wing surface is conventional sheet metal/stiffener construction.

Wing/Flap Design.

Wing Insulation. The upper surface of the wing box beam aft of the nozzle discharge is insulated with a fireproof coating. This protects the upper wing and flap structure from burning fuel which can result from a wet start and reduces the temperature variation in the wing structure to within acceptable limits.

Flap System. To obtain maximum acoustic attenuation for the upper surface jet flow, a long-chord high-extension flap system was selected. Directly behind the engine the flap surface is continuous, as is shown in figure 40. Away from the nacelles, however, slots are provided to assure attachment of the freestream. In case of engine failure, slots can be opened in the unslotted portion of the wing behind the dead engine.

The flap system shown indicates how chord extension can be obtained. The first flap segment slides back on a fixed track. The second segment is mounted to the first through another track which provides further extension. As shown, in a representative landing configuration, the extension, measured along the upper surface, is 36% of the wing chord.

At takeoff the extension with this track configuration would be about 25% of the wing chord. Interpolation on figure 38 indicates that a 25% chord extension is in itself sufficient to achieve the noise footprint area goal, even with the baseline takeoff performance. Baseline performance can be improved, however, in several ways. First, the 12% of fan airflow used by the baseline internal flap blowing system can be returned to the main nozzle for more efficient thrust production and the weight of the flap ducts can be saved. Second, the flap tracks can be designed so that the takeoff setting provides considerably more chord extension, with only the angular deflection required for takeoff, while the final extension to the landing setting serves primarily to increase deflection with little increase in chord. This arrangement is in use today. Chord extensions of 40% or more at takeoff should be feasible.

4.6 Noise Characteristics

The noise characteristics of the final design were calculated based on the following:

- o Aircraft size, weight, and performance as in baseline.
- o 40% chord flap extension at both takeoff and landing.
- o Flap deflections and landing thrust setting as in baseline.
- o No internal flap blowing.
- o No fan duct noise treatment.

The calculated values are:

Takeoff Footprint Area, 90 EPNdB -	1.76 km^2 (0.68 m^2)
Takeoff Flyover at 6.49 Km (3.5 n.m.) -	79.5 EPNdB
Takeoff, Maximum at 152.4 M (500 Ft) Sideline -	98.4 EPNdB
Landing Footprint Area, 90 EPNdB -	0.12 km^2 (0.05 m^2)
Landing Flyover at 1.86 Km (1 n.m.) -	86.8 EPNdB
Total Footprint Area, 90 EPNdB -	1.88 km^2 (0.73 m^2)

It can be seen that the calculated total footprint area of 1.88 km^2 (0.73 m^2) betters the 2.59 km^2 (1 m^2) goal by a considerable margin. The area would be further reduced if the overlap of the takeoff area and landing area were subtracted.

The flight path and noise footprint are shown in figure 41. The takeoff spectra of the various noise sources considered in the prediction program and of the complete aircraft are presented for the flyover location in figure 42. Even with no fan duct treatment, high-lift system noise is the strongest source, although fan noise exceeds it at the higher frequencies. The PNL directivity pattern at takeoff is shown in figure 43.

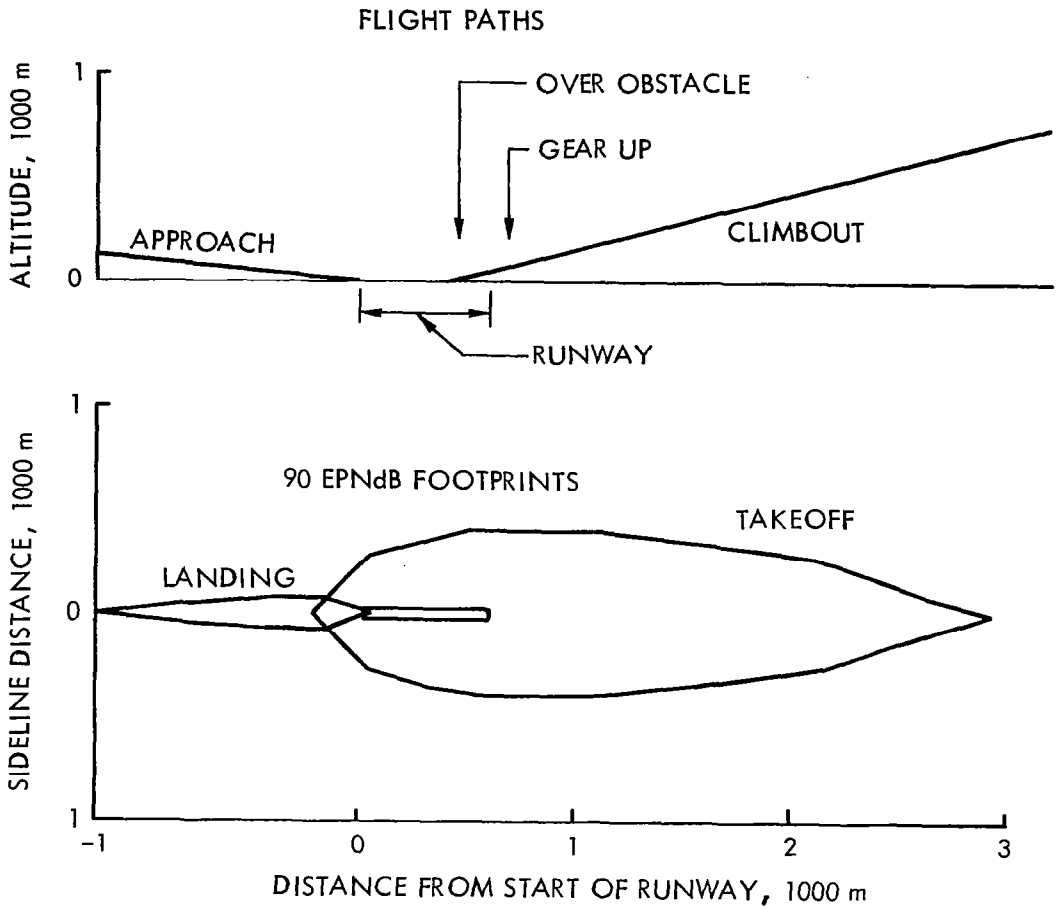

FIGURE 41. FLIGHT PATHS AND NOISE FOOTPRINTS, FINAL DESIGN AIRCRAFT.

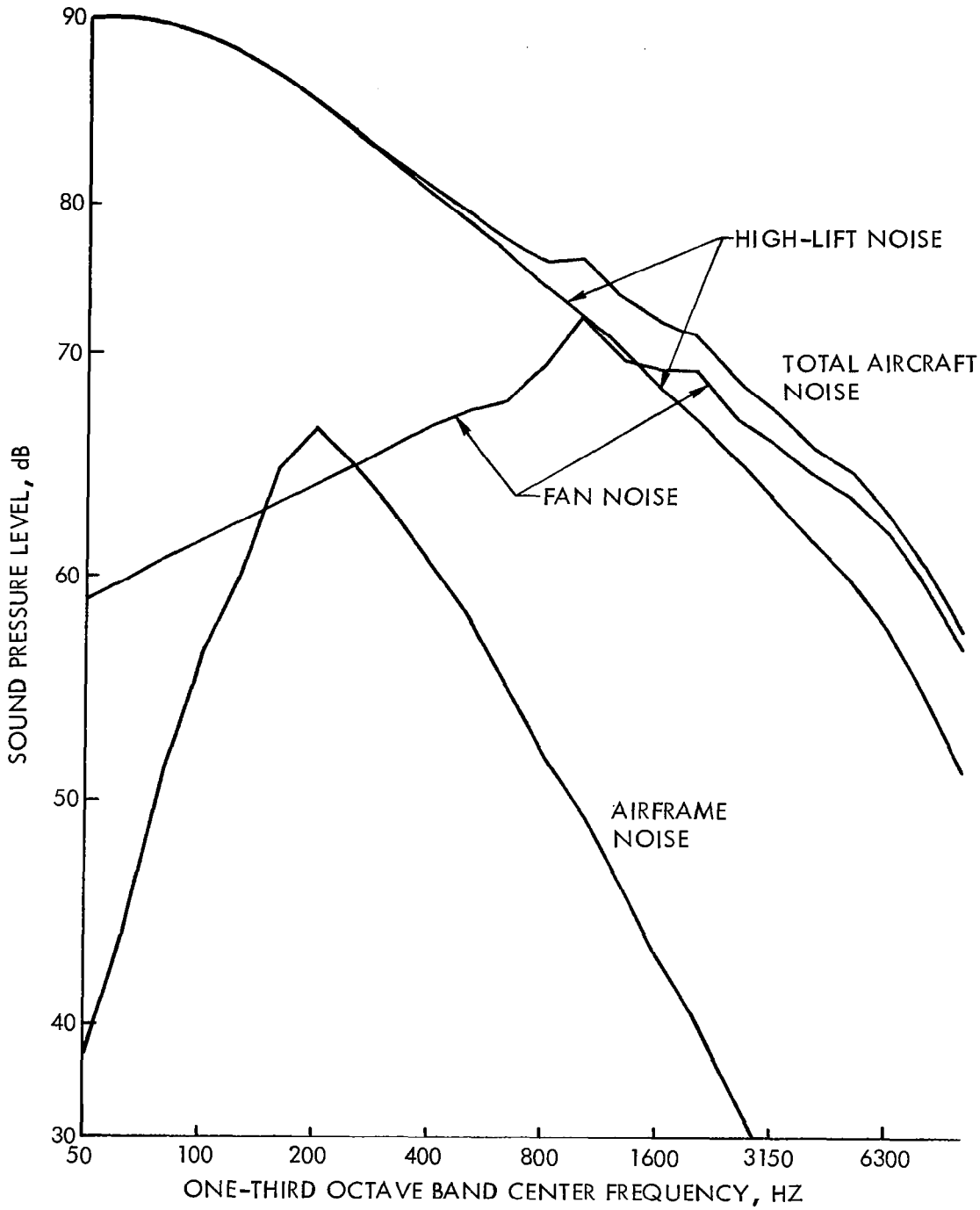

FIGURE 42. SPECTRA BY SOURCE, FINAL DESIGN AIRCRAFT, TAKEOFF. Elevation Angle = 90°; Angle from Nose = 90°; 152.4 m (500 Ft.) Distance; No Ground Reflection.

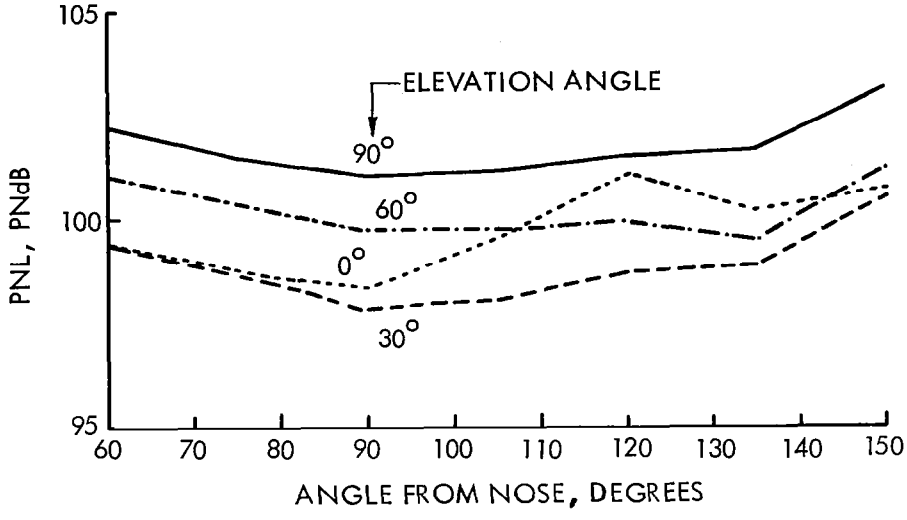

FIGURE 43. PNL DIRECTIVITY, FINAL DESIGN AIRCRAFT, TAKEOFF. 152.4 m (500 Ft.) Radius; No Ground Reflections.

5. THEORETICAL DEVELOPMENTS OF TRAILING EDGE NOISE

The various USB noise source mechanisms and their relative importance to community noise were discussed in Section 2. It was concluded that the flow mixing noise downstream of the trailing edge is a dominant noise source in a practical USB flap system. Therefore, in order to gain some insight into the basic phenomena of noise generation, a theory was developed for the radiated noise from the shear layer downstream of the trailing edge. In this theoretical development, the relationship between the flow characteristics and the radiated sound field were derived.

5.1 Theoretical Formulation

The following assumptions were made in modeling the trailing edge wake shear flow.

The trailing edge wake is assumed to be locally a two-dimensional shear layer with a constant thickness δ and the turbulence is spatially homogeneous with respect to any plane parallel to the shear layer. These assumptions, of course, require that the growth rate of the shear layer is small, which is true in most cases, particularly when consideration is given to the expansion of the shear layer beyond the trailing edge in the x-z plane.

The fluid inside the layer is assumed to be incompressible so that the fluctuating pressure inside at the edges of the shear layer can be estimated by regarding the speed of propagation of pressure disturbances to be effectively infinite. This assumption is reasonable when the flow velocity in the trailing edge wake is small and the layer is thin. In the case of practical USB, good spreading of the subsonic jet flow is a desirable feature and thus it is reasonable to assume that the flow velocity in the wake is small. For calculations of the radiated sound field from the flow mixing in the wake, the layer may be regarded as thin.

In addition to the above basic assumptions, some of the characteristics of the fluctuating velocities are assumed to be known. These assumptions and the measured characteristics will be further discussed as the analysis for the radiated sound field is developed.

Consider a two-dimensional turbulent shear layer with a constant thickness δ' and characteristic velocity U as shown in figure 44. With the assumption of flow incompressibility in the wake, the fluctuating pressure, p due to turbulence inside the shear layer is given by the solution of the following Poisson's equation (see refs. 37 and 38).

$$\nabla^2 p = -\rho \left[2 \frac{d\bar{u}}{dz} \cdot \frac{\partial w}{\partial x} + \frac{\partial^2 u_i u_j}{\partial x_i \partial x_j} \right] \equiv -T(x,y,z,t) \tag{2}$$

where ρ is the density, $\bar{u}(z)$ is the mean flow velocity and (u,v,w) or $u_i (i = 1,2,3)$ are the turbulent velocity components in the x,y, and z directions. A formal solution of equation (2) can be constructed by first taking the Fourier transform of this equation in x and y as

$$\frac{d^2\tilde{p}}{dz^2} - (k_x^2 + k_y^2)\tilde{p} = -\tilde{T}(k_x,k_y,z,t) \tag{3}$$

where $\tilde{p}$ and $\tilde{T}$ are the Fourier transforms of p and T, respectively, while k_x and k_y are the Fourier transform variables. $\tilde{T}$ is related to the velocity field by

$$\tilde{T} = \frac{\rho}{(2\pi)^2} \iint_{-\infty}^{\infty} \left[2 \frac{du}{dz} \frac{\partial w}{\partial x} + \frac{\partial^2 u_i u_j}{\partial x_i \partial x_j} \right] e^{-(k_x x + k_y y)} \cdot dx\, dy \tag{3a}$$

The solution of equation (3) which satisfies the boundedness condition away from the shear layer is

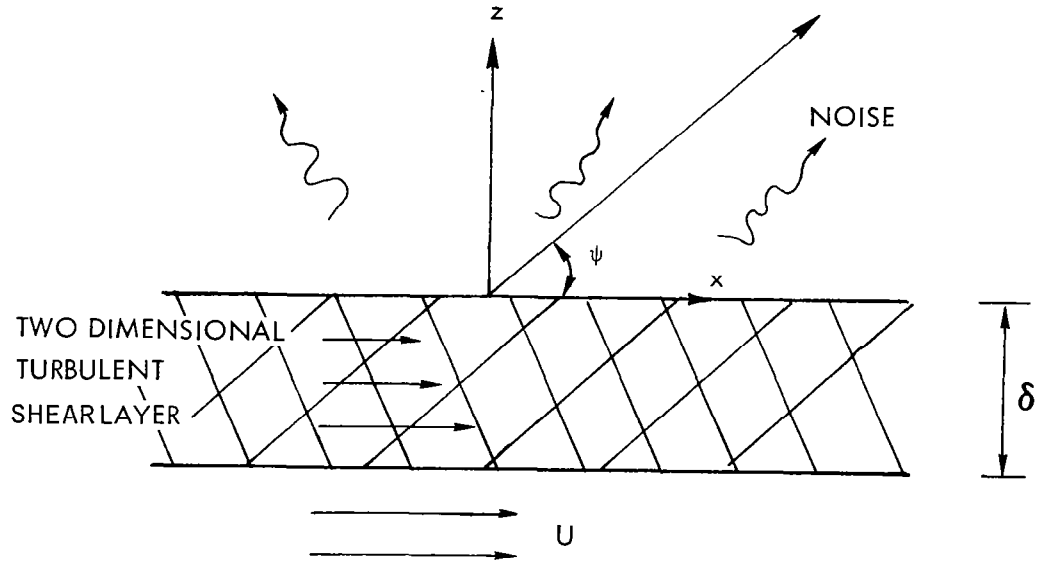

FIGURE 44. MODEL OF A TWO DIMENSIONAL TURBULENT SHEAR LAYER. (NOTE THE z-AXIS IS THE NEGATIVE OF THAT USED IN PREVIOUS FIGURES)

$$\tilde{p}(k_x,k_y,z,t) = \frac{1}{2}\int_{-\infty}^{\infty} \frac{1}{k_1}\, e^{-k_1|z-z'|}\tilde{T}(k_x,k_y,z',t)dz' \tag{4}$$

where $k_1 = \sqrt{k_x^2 + k_y^2}$.

Since our interest in this problem is to calculate the radiated sound field from the shear layer, the fluctuating pressures from the turbulent mixing of the shear layer only are considered. Thus, in equation (4) $\tilde{T}$ is taken to be zero outside the turbulent shear layer. The limits of the integral, therefore, may be replaced by the thickness of the shear layer, δ as

$$\tilde{p} = \frac{1}{2}\int_{-\delta'}^{0} \frac{1}{k_1}\, e^{-k_1|z-z'|}\tilde{T}(k_x,k_y,z',t)dz' \tag{5}$$

By inverting the Fourier transform in equation (5), the turbulent pressure fluctuation in the x-y plane (figure 44) can be found

$$p(x,y,t)_{Z=0} = \frac{1}{2}\int_{-\delta'}^{0}\int_{-\infty}^{\infty} \frac{1}{k_1}\, e^{k_1 z'}\, \tilde{T}(k_x,k_y,z',t)$$

$$e^{i(k_x x + k_y y)}\, dz'\, dk_y\, dk_y$$

Substitution of $\tilde{T}$ from Equation (3a) and use of the relation (2) leads to

$$p(x,y,t) = \frac{1}{8\pi^2}\int_{-\delta'}^{0}\int\int_{-\infty}^{\infty}\int\int \frac{1}{k_1}\, T(x',y',z',t)$$

$$e^{k_1 z' + i[k_x(x-x') + k_y(y-y')]}$$

$$\cdot\, dx'\, dy'\, dk_x\, dk_y\, dz'. \tag{6}$$

In order to calculate the radiated sound field, it is necessary to evaluate the cross-correlation function and its Fourier transform of the fluctuating

pressures since it is of interest, to calculate the sound radiated in the direction above the z-plane, the characteristics of the fluctuating pressures in the plane $z = 0$ are required. The cross-correlation function of the pressures in this plane is given by

$$\langle p(x,y,t)\ p(x+\xi,\ y+\eta,\ t+\tau)\rangle = \frac{1}{64\pi^4} \int_{-\delta'}^{0} \int_{\infty}^{\infty} \frac{1}{k_1} \frac{1}{k_1'}$$

$$\cdot \langle T(x',y',z',t+\tau)\ T(x'',y'',z'',t)\rangle\ e^{k_1 z' + k_1' z''}$$

$$\cdot e^{i[k_x(x'x') + k_y(y-y')] + i[k_x'(x-x'') + k_y'(y'y'')]} \qquad (7)$$

$$\cdot e^{i(k_x\xi + K_y\eta)}$$

$$\cdot dx'\ dy'\ dx''\ dy''\ dk_x\ \ dk_y\ \ dk_x'\ dk_y'\ dz'\ dz''$$

The assumption of spatially homogeneous turbulence in the x-y plane (parallel to shear layer) will enable one to consider the cross-correlation of velocity terms, T, as a function of separation distance rather than the actual location of the points. Thus, the cross-correlation function of T may be written as

$$\langle T(x',y',z',t+\tau)\ \ T(x'',y'',z'',t)\rangle = R_T(x',y',z',t+\tau,z'',y'',z'',t)$$

$$= R_T(\bar{x},\bar{y},z',z'',\tau) \qquad (8)$$

where $\bar{x} = x' - x''$ and $\bar{y} = y' - y''$.

Now the tenfold integration in equation (7) can be evaluated by using $\bar{x},\bar{y}$ as the integration variables instead of x' and y'. Equation (7) may be written as

$$\langle p(x,y,t)\ p(x+\xi,\ y+\eta,\ t+\tau) = \frac{1}{64\pi^4} \int_{-\delta'}^{0} \int\int\int\int\int\int\int\int_{-\infty}^{\infty} \frac{1}{k_\perp k_\perp'} R_T(\bar{x},\bar{y},z',z'',\tau)$$

$$\cdot e^{k_\perp z' + k_\perp' z''} \cdot e^{-i(k_x\bar{x} + k_y\bar{y}) - i(k_x + k_x')x'' - i(k_y + k_y')y''}$$

$$\cdot e^{i(k_x + k_x')x + i(k_y + k_y')y} \cdot e^{i(k_x\xi + k_y\eta)}$$

$$\cdot dx\ dy\ dx''\ dy''\ dk_x\ dk_y\ dk_x'\ dk_y'\ dz'\ dz''$$

At this stage, the variables x'' and y'' of the integrand are separated. The integration over these variables gives the product of two delta functions as,

$$\frac{1}{4\pi^4} \int\int_{-\infty}^{\infty} e^{-i(k_x+k_x')x'' - i(k_y+k_y')y''} \cdot dx\ dy = \delta(k_x+k_x') \cdot \delta(k_y + k_y')$$

The Fourier transform of R_T may be written as,

$$\tilde{R}_T(k_x,k_y,z',z'',\tau) = \frac{1}{2\pi^2} \int\int_{-\infty}^{\infty} R_T(\bar{x},\bar{y},z',z'',\tau) \cdot e^{-(k_x\bar{x} + k_y\bar{y})}\, d\bar{x}\ d\bar{y}$$

Using these expressions and integrating over k_x' and k_y', the following expression is obtained.

$$\langle p(x,y,t)\ p(x+\xi,\ y+\eta,\ t+\tau)\rangle \equiv R_p(\xi,\eta,\tau) \rangle \equiv R_p(\xi,\eta,\tau)$$

$$= \frac{1}{4} \int_{-\delta'}^{0} \int\int_{-\infty}^{\infty} \frac{1}{k_\perp^2} \tilde{R}_T(k_x,k_y,z',z'',\tau)\ e^{k_\perp(z'+z'')}\ i(k_x\xi+k_y\eta)\ dk_x\ dk_y\ dz'\ dz'' \qquad (9)$$

The Fourier transform of $R_p(\xi,\eta,\tau)$ is

$$\tilde{R}_p(k_x,k_y,\omega) = \frac{1}{(2\pi)^3}\iiint_{-\infty}^{\infty} R_p(\xi,\eta,\tau)\, e^{-i(k_x\xi + k_y\eta - \omega\tau)}\, d\xi d\eta d\tau$$

$$= \frac{1}{4}\iint_{-\delta'}^{0} \frac{1}{k_1^2}\,\tilde{R}_T(k_x,k_y,z',z''\omega)\, e^{k_1(z'+z'')}\, dz'\, dz'' \qquad (10)$$

In equation (10), R_T is related to the turbulent velocity correlations by equation (8) and (2).

$$R_T(x,y,z',z'',\tau) = \langle T(x',y',z',t+\tau)\; T(x'',y'',z'',t)\rangle$$

$$= 4\rho^2 \frac{d\bar{u}}{dz'}\frac{d\bar{u}}{dz''}\frac{\partial w}{\partial x'}\frac{\partial w}{\partial x''} + 2\rho^2 \frac{du}{dz'}\frac{\partial w}{\partial x'}\frac{\partial^2 u_k u_l}{\partial x_k''\partial x_l''}$$

$$+ \frac{\bar{u}}{dz''}\frac{\partial w}{\partial x''}\frac{\partial^2 u_i u_j}{\partial x_j'\partial x_i'}\rangle + \rho^2 \langle \frac{\partial^2 u_k u_l}{\partial x_i\,\partial x_j}\frac{\partial^2 u_k u_l}{\partial x_k''\partial x_l''} \qquad (11)$$

In equation (11) there are three types of terms involving correlation of two, three, and four turbulent velocity components. The relative significance of these terms with respect to their contributions to the integral in equation (10) will be examined as follows:

Terms Involving Correlation of Two Velocity Components:

The cross-correlation function of the fluctuating velocities, w, is defined as

$$R_w(x',y',z',t+\tau;x'',y'',z'',t) = \langle w(x',y',z',t+\tau)\cdot w(x'',y'',z'',t)\rangle$$

Since the turbulence is assumed to be homogeneous in the x-y plane, the correlation function may be written as

$$R_w(x',y',z',t+\tau;x'',y'',z'',t) = R_w(\bar{x},\bar{y},z',z'',\tau)$$

(Note that $\bar{x} = x' - x''$, $\bar{y} = y' - y''$)

This function is a measure of turbulence characteristics of the shear layer. The first term of equation (11) consisting of two velocity terms may be written as

$$4\rho^2 \frac{d\bar{u}}{dz'} \frac{d\bar{u}}{dz''} \left\langle \frac{\partial w}{\partial x'} \frac{\partial w}{\partial x''} \right\rangle = 4\rho^2 \frac{d\bar{u}}{dz'} \frac{d\bar{u}}{dz''} \frac{\partial^2}{\partial x^2} R_w(\bar{x},\bar{y},z',z'',\tau)$$

Present day knowledge of turbulent characteristics of shear flow is not adequate to formulate a general prediction model for the correlation function, $R_w(\bar{x},\bar{y},z',z'',\tau)$. Therefore for the purpose of evaluating the importance of this term, it will be modeled empirically using some of the experimental data. Figure 45 shows a typical space-time correlation function of turbulent velocities measured in the shear layer. The details of these measurements are discussed in the next section. In references 39 and 40 such a correlation function was approximated by superposition of functions of the following form:

$$R_w(\bar{x},\bar{y},z',z'',\tau) \sim e^{-\bar{x}/\lambda\delta'} \left[\frac{\alpha A}{\alpha^2 + \left(\frac{U}{U_c\delta}\right)^2 [(\bar{x} - U_c\tau)^2 + \beta^2\bar{y}^2]} \right]$$

where λ is the longitudinal decay rate of the cross-correlation function. This is a measure of the distance travelled by an eddy or wave in the shear layer before coherence is lost.

α and A are constants

U_c is the eddy (wave) convection velocity

β is the scale of anisotropy.

In order to establish the dependence of the correlation function, R_w, on lateral coordinates z' and z'', extensive correlation measurements are required. Such accurate data are not available and extremely difficult to obtain. Thus, using the limited available data, it would seem reasonable to assume the following form:

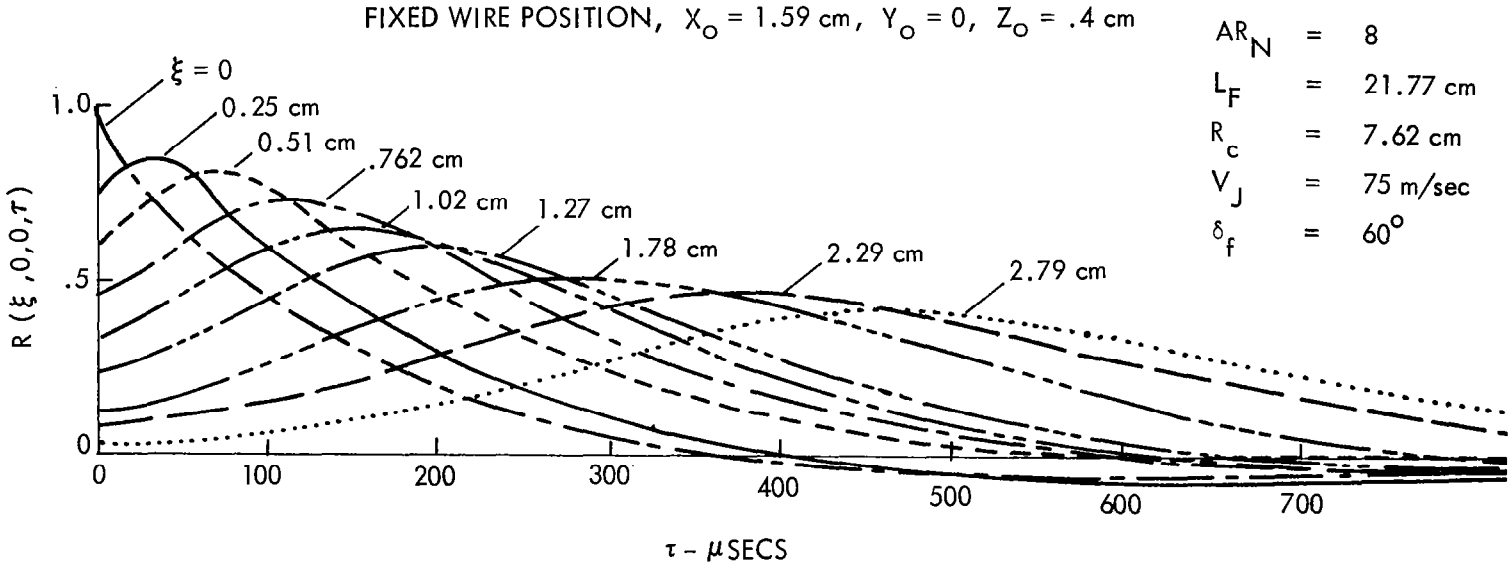

FIGURE 45. STREAMWISE SPACE - TIME CORRELATION

$$R_w(\bar{x},\bar{y},z',z'',\tau) = G(z',z'')\ e^{-|\bar{x}|/\lambda\delta'} \frac{\sum_{i=1}^{n} \frac{\alpha_i A_i}{\alpha_i^2 + \left(\frac{U}{U_c\delta}\right)^2 [(x - U_c\tau)^2 + \beta^2\bar{y}^2]}}{\sum_{i=1}^{n} \frac{A_i}{\alpha_i}} \tag{12}$$

where $G(z',z'')$ is the lateral (z-direction) correlation function of the velocity fluctuations of zero time delay.

The parameters U_c, β, λ, α_i, and A_i may depend on z' and z''. On setting $\bar{x} = \bar{y} = 0$ and $z' = z''$, equation (12) becomes

$$R_w(0,0,z',\tau) = G(z') \frac{\sum_{i=1}^{n} \frac{\alpha_i A_i}{\alpha_i^2 + \left(\frac{U\tau}{\delta}\right)^2}}{\sum_{i=1}^{n} \frac{A_i}{\alpha_i}} \tag{13}$$

The Fourier transform of equation (13) gives the power spectrum of turbulence

$$P(0,0,z',\omega) = \frac{1}{2\pi} \int_{-\infty}^{\infty} R(0,0,z',\tau)\ e^{-i\omega\tau}\ d\tau$$

$$= \frac{G(z')}{2\pi} \int_{-\infty}^{\infty} \frac{\sum_{i=1}^{n} \frac{\alpha_i A_i \frac{\delta'^2}{U^2}}{\left(\frac{\alpha_i\delta'}{U}\right)^2 + \tau^2}}{\sum_{i=1}^{n} \alpha_i A_i} \cdot e^{-i\omega\tau}\ d\tau$$

$$= \frac{G(z')}{2U} \quad \frac{\sum_{i=1}^{n} A_i \, e^{-\alpha_i \frac{\omega\delta'}{U}}}{\sum_{i=1}^{n} \alpha_i A_i}$$

Therefore, the power spectrum is given by

$$\frac{P(\omega)}{G(z')} \cdot \frac{U}{\delta'} = \frac{1}{2} \quad \frac{\sum_{i=1}^{n} A_i \, e^{-\alpha_i \frac{\omega\delta'}{U}}}{\sum_{i=1}^{n} \alpha_i A_i} \tag{14}$$

Thus, α_i ($i = 1,2, \ldots n$) may be determined by fitting equation (14) to the measured power spectrum or equation (13) to the measured auto-correlation function of the turbulence. The actual measurements of the correlations in the trailing edge wake and the evaluation of the various parameters are discussed in the next section.

The Fourier transform of the correlation function (12) is

$$\tilde{R}_w(k_x,k_y,z',z'',\omega) = \frac{1}{(2\pi)^3} \iiint_{-\infty}^{\infty} R_w(x,y,z',z'',\tau) \, e^{-(k_x x + k_y y - \omega\tau)} \, d\bar{x} \, d\bar{y} \, d\tau$$

$$= \frac{(G(z',z'')U_c\delta}{2\pi^2 \beta U^2 \lambda} \cdot \frac{\sum_{i=1}^{n} \alpha_i A_i K_o \left[\frac{\alpha_i U_c \delta'}{U} \sqrt{\frac{k_y^2}{\beta^2} + \frac{\omega^2}{u_c^2}} \right]}{\sum_{i=1}^{n} \frac{A_i}{\alpha_i} \left[\frac{1}{(\lambda\delta')^2} + k_x - \frac{\omega}{u_c} \right]} \tag{15}$$

where $K_o(\ )$ is the zeroth order modified Bessel function. Therefore, the Fourier transform of the first term of equation (11), which consists of correlation between the two lateral velocity components may be written as

$$\tilde{R}_T(k_x,k_y,z',z'',\omega) = 4\rho^2 \frac{d\bar{u}}{dz'} \frac{d\bar{u}}{dz''} \frac{G(z',z'')U_c\delta' k_x^2}{2\pi^2 \beta \lambda U^2}$$

$$\frac{\sum_{i=1}^{n} \alpha_i A_i k_o \left[\alpha_i \delta' \frac{U_c}{U} \sqrt{\frac{k_y^2}{\beta^2} + \frac{\omega^2}{U_c^2}}\right]}{\sum_{i=1}^{n} \frac{A_i}{\alpha_i} \left[\frac{1}{(\lambda\delta')^2} + \left(k_x - \frac{\omega}{U_c}\right)^2\right]} \qquad (16)$$

Experimental measurements of the radiated sound field of the jet flow over a finite flap length (attributed to the trailing edge noise) by many investigators (refs. 8, 11, 15, 16, and 23) indicate that the dominant part of the noise generated in the vicinity of the trailing edge (which contributes equally in directions both above and below the wing) is in the low frequency range with $\omega\delta/U<<1$. Since $k_x\delta$ and $k_y\delta$ are proportional to $\omega\delta/U \cdot M$ (M is the Mach number based on the ambient speed of sound), it is expected that only low frequency and small wave number components are important in equation (16).

Terms Involving Correlation of Three Velocity Components:

The second and third terms in equation (11) consists of correlation of the three velocity components. A typical term may be written as

$$\frac{d\bar{u}}{dz''} \left\langle \frac{\partial w}{\partial x''} \frac{\partial^2 u_i u_j}{x_i' x_j'} \right\rangle = \frac{d\bar{u}}{dz''} \frac{\partial^3 \langle w u_i u_j \rangle}{\partial x \partial x_i \partial x_j} = \frac{d\bar{u}}{dz''} \frac{\partial^3 R(w,u,u_j)}{\partial x \partial x_i \partial x_j}$$

where $x_i = x_i' - x_i''$ is used.

The Fourier transform of this term is given by

$$\frac{d\bar{u}}{dz''} \cdot k_1^3 \tilde{R}(w,u_i,u_j)$$

The correlation function of three velocity fluctuations is not easily obtainable experimentally since it involves three components in three

directions. However, it may be expected that $\tilde{R}(w,u_i,u_j)$ to have similar characteristics as R_w. Now, from a noise standpoint, since we are only interested in components of small wave numbers, the term $d\bar{u}/dz'' \cdot K_1^3 R(w,u_i,u_j)$ is an order $\omega\delta/U \cdot M$ smaller than equation (16) even if $\tilde{R}(w,u_i,u_j)$ is comparable in magnitude to $\tilde{R}_w$. Actually, $\tilde{R}(w,u_i,u_j)$ is much smaller than $\tilde{R}_w$, because it is expected that u and w are the same order of magnitude as v is very much smaller than u or w. Therefore, in estimating the radiated sound field, terms of this type may be neglected.

Terms Involving Correlation of Four Velocity Components:

Arguments similar to that used for the correlations of three velocity components in the previous paragraph show that these terms are of the order $(\omega\delta/U)^2 M^2$ smaller than equation (16). For a highly sheared turbulent layer, where the velocity gradient is large, it is therefore permissible to neglect these terms as well. A similar conclusion was arrived at for the simple jets in reference 41. In a recent work on wall pressure spectra of turbulent boundary layers, the same approximation was employed in reference 42.

Therefore, it may be concluded that the correlation function of more than two fluctuating velocities may be neglected. Retaining only the most important term, the correlation function, R_T is given as

$$R_T(x,y,z',z'',\tau) = 4\rho^2 \frac{du}{dz'} \cdot \frac{du}{dz''} \left\langle \frac{\partial w}{\partial x'} \frac{\partial w}{\partial x''} \right\rangle = 4\rho^2 \frac{d\bar{u}}{dz'} \cdot \frac{d\bar{u}}{dz''} \frac{\partial^2}{\partial x^2} R_w(x,y,z',z'',\tau) \qquad (17)$$

where $R_w(\bar{x},\bar{y},z',z'',\tau)$ is defined by equation (12).

Relation Between Fluctuating Pressure and Flow

Equation (10) may be simplified to relate the fluctuating pressures to the flow characteristics using equations (17) and (12) as

$$\tilde{R}(k_x,k_y,\omega) = \frac{\rho^2}{2\pi^2} \iint_{-\delta'}^{0} \frac{d\bar{u}}{dz'} \frac{d\bar{u}}{dz''} G(z',z'')$$

$$\frac{U_c \delta' k_x^2}{\beta\lambda U^2 (k_x^2 + k_y^2)} \frac{\sum_{i=1}^{n} A_i \alpha_i K_o \left[\frac{\alpha_i \delta' U_c}{U} \sqrt{\frac{k_y^2}{\beta^2} + \frac{\omega^2}{U_c^2}} \right]}{\sum_{i=1}^{n} \frac{A_i}{\alpha_i} \left[\frac{1}{(\lambda\delta')^2} + \left(k_x - \frac{\omega}{U_c} \right)^2 \right]} dz' \, dz'' \qquad (18)$$

Since small values of k_x and k_y are more important in calculations of the sound field, it is assumed in equation (18), $e^{k_1(z'+z'')} \approx 1$. It is not feasible to evaluate all the terms in equation (18) as a function of z' and z''. However, the measurements indicate that $d\bar{u}/dz'$ and $G(z')$ are highly peaked functions (with maximum at $z = z_m$). The constants ρ, U_c, λ, A_i and α_i could be evaluated at $z = z_m$ and are considered to be independent of z, so that they can be taken outside the integrals. Thus, the Fourier transform of pressure correlation function may be written as

$$\tilde{R}(k_x,k_y,\omega) = \frac{\rho^2 U_c \delta'^3}{2\pi^2 \beta\lambda U} \frac{k_x}{k_x^2 + k_y^2} \frac{\sum_{i=1}^{n} A_i \alpha_i K_o \left[\frac{\alpha_i \delta' U_c}{U} \sqrt{\frac{k_y^2}{\beta^2} + \frac{\omega^2}{U_c^2}} \right]}{\sum_{i=1}^{n} \frac{A_i}{\alpha_i} \left[\frac{1}{\lambda^2} + \delta'^2 \left(k_x - \frac{\omega}{U_c} \right)^2 \right]}$$

$$\cdot \iint_{-\delta}^{0} \frac{d\bar{u}}{dz'} \frac{d\bar{u}}{dz''} G(z',z'') \, dz' \, dz'' \qquad (19)$$

Relation Between the Fluctuating Pressures and Radiated Sound. The fluctuating pressures in the x-y plane due to the turbulence in the shear layer are related to the sound pressures, p, radiating above x-y plane by the wave equation

$$\nabla^2 p - \frac{1}{a^2} \frac{\partial^2 p}{\partial t^2} = 0$$

with the boundary condition

$$p(x,y,o,t) = p_w(x,y,t) \qquad \text{at} \qquad z = 0$$

and the outgoing sound propagation condition at $z \to \infty$.

Solution of this equation for a two-dimensional boundary layer noise is solved in reference 43. Since the pressure wave components with subsonic phase velocities decay much faster (exponentially), only the components with supersonic phase velocities are considered in order to calculate the radiated sound. With this condition, the far-field sound pressure auto-correlation function is related to the near-field pressure cross-correlation function by,

$$\langle p(x,y,z,t)p(x,y,z,t+\tau)\rangle = \iiint_V \tilde{R}(k_x,k_y,\ ) \ e^{-i\omega\tau} \ dk_x \ dk_y \ d\omega$$

where the integration volume, V, is the conical region, $\omega^2 \geq a\ (k_x^2 + k_y^2)$ in the k_x, k_y, space as shown in figure 46.

The sound power radiated per unit frequency per unit solid angle, Ω, from a unit surface area of the shear layer (x-y plane) in the direction ψ in the x-z plane is given by the directivity function $D(\psi,\omega)$. The details of this derivation can be found in reference 43.

$$D(\psi,\omega) = \frac{1}{\rho a}\frac{dp(\psi,\omega)}{d\Omega} = \frac{1}{\rho a}\tilde{R}\left(\frac{\omega}{a}\cos\psi, 0, \omega\right)\frac{\omega^2}{a^2}\sin\psi$$

where $P(\psi,\omega)$ is the power spectrum per unit solid angle, Ω is the solid angle and a is the ambient speed of sound. Upon using the expression R given in equation (19), the directivity function becomes

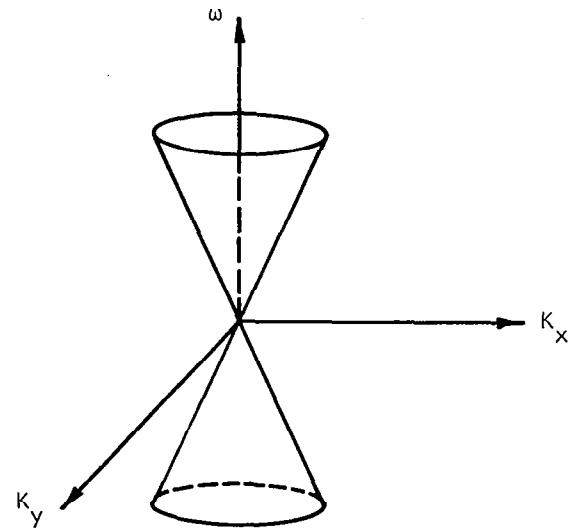

FIGURE 46. THE ACOUSTIC RADIATION CONE IN (K_x, K_y, ω) SPACE

$$\frac{D(\psi,\omega)}{\rho U^2 \delta} = \frac{\frac{U_c}{U}\left(\frac{\omega\delta'}{U}\right)^2 M^3 \sin\psi}{2\pi^2\ \beta\lambda}$$

$$\frac{\sum_{i=1}^{n} A_i \alpha_i K_o\left(\frac{\alpha_i \delta' \omega}{U}\right)\left[\frac{1}{U^4}\iint_{-\delta'}^{o} \frac{du}{dz'}\frac{du}{dz''}\, G(z',z'')\, dz'dz''\right]}{\sum_{i=1}^{n}\left(\frac{A_i}{\alpha_i}\right)\left[\frac{1}{\lambda^2} + \left(\frac{\omega\delta'}{U}\right)^2\left(M\cos\psi - \frac{U}{U_c}\right)^2\right]} \qquad (20)$$

$M = U/a$ is the flow Mach number based on ambient speed of sound. In equation (20), for a fixed Strouhal number, $S = \omega\delta'/U$, the quantities in square brackets are not expected to be strongly dependent on U. δ' is a weak function of velocity; but to obtain the total noise radiation in a fixed direction, it is necessary to integrate the above expression over the whole surface of the turbulent shear layer. Suppose L_s is the effective length of this surface area, then the product $L_s\delta'$ is weakly dependent on U. Thus, equation (20) suggests that trailing edge noise per unit frequency is roughly scaled according to a U^5 law (or U^6 dependence for total noise power). It is to be noted that a similar velocity dependence was derived in reference 21. But, their conclusion was based on an entirely different mechanism.

The measured flow characteristics in USB trailing edge wakes and the discussion of evaluation of various turbulence parameters required in the theory are discussed in the next section.

5.2 Flow Characteristics in the Trailing Edge Wake

Experiments were conducted in order to obtain mean flow and turbulence characteristics of the flow field in USB trailing edge wakes. The details of these experiments and the experimental results are presented in reference 1. The quantitative information on turbulence characteristics required for the theoretical evaluation of the trailing edge wake and to provide a better understanding of the physical processes causing the noise generation were measured for one configuration. Calculations based on these measurements

and comparisons with the measured noise data revealed information about the dominance of trailing edge wake noise.

The experimental model for these studies consisted of a jet blowing over a wing/flap surface as illustrated schematically in Figure 1. The jet flow was from a convergent rectangular nozzle with exit area of 20.26 cm^2 and width-to-height ratio of 8. The air supply for the jet was from a continuous air supply at ambient temperature. The jet velocity was controlled using a regulator and all the flow results were obtained at a nozzle pressure ratio of 1.1 and the maximum velocity at the trailing edge was 75 m/sec. The details of the air supply system are discussed in reference 1. The wing/flap is of rectangular planform with 50.8 cm span and the total streamwise length on the surface was 26.47 cm. The flap consisted of two chordwise segments, one with a radius of curvature of 7.62 cm and the other a 6.48 cm long straight trailing edge segment with flow turning angle (flap angle) of 60°. The flow length, defined as the length on the surface between the nozzle exit and the flap trailing edge, was 22.5 cm. The nozzle was located on the surface with the nozzle axis inclined to the wing surface at an angle of 20°. The jet flow was turned along the surface as visualized by the oil-flow picture on the surface as shown in Figure 47 and also some smoke flow visualizations. The mean flow and turbulence characteristics were measured along the jet centerline (mid-span) in the wake. The coordinates used in discussing these measurements are shown in Figure 1.

Mean and Fluctuating Velocity Profiles. The mean velocity and turbulence intensities were measured using a constant temperature hot-wire probe mounted parallel to the trailing edge (y-axis) on a remotely controlled traverse mechanism. A single hot-wire is sensitive to the two velocity components in the direction perpendicular to the wire. There, the measured velocities are the resultant of longitudinal (x) and lateral (z) components, viz. $\sqrt{u^2+w^2}$. It was assumed that the lateral components of mean velocity, was negligible compared to the longitudinal component, $\bar{u}$; and the profiles of the fluctuating velocities of both components, u and w are similar. The previous measurements reported in references 15 and 17 indicated that the turbulence intensity away from the surface (large z) are the same order of magnitude for

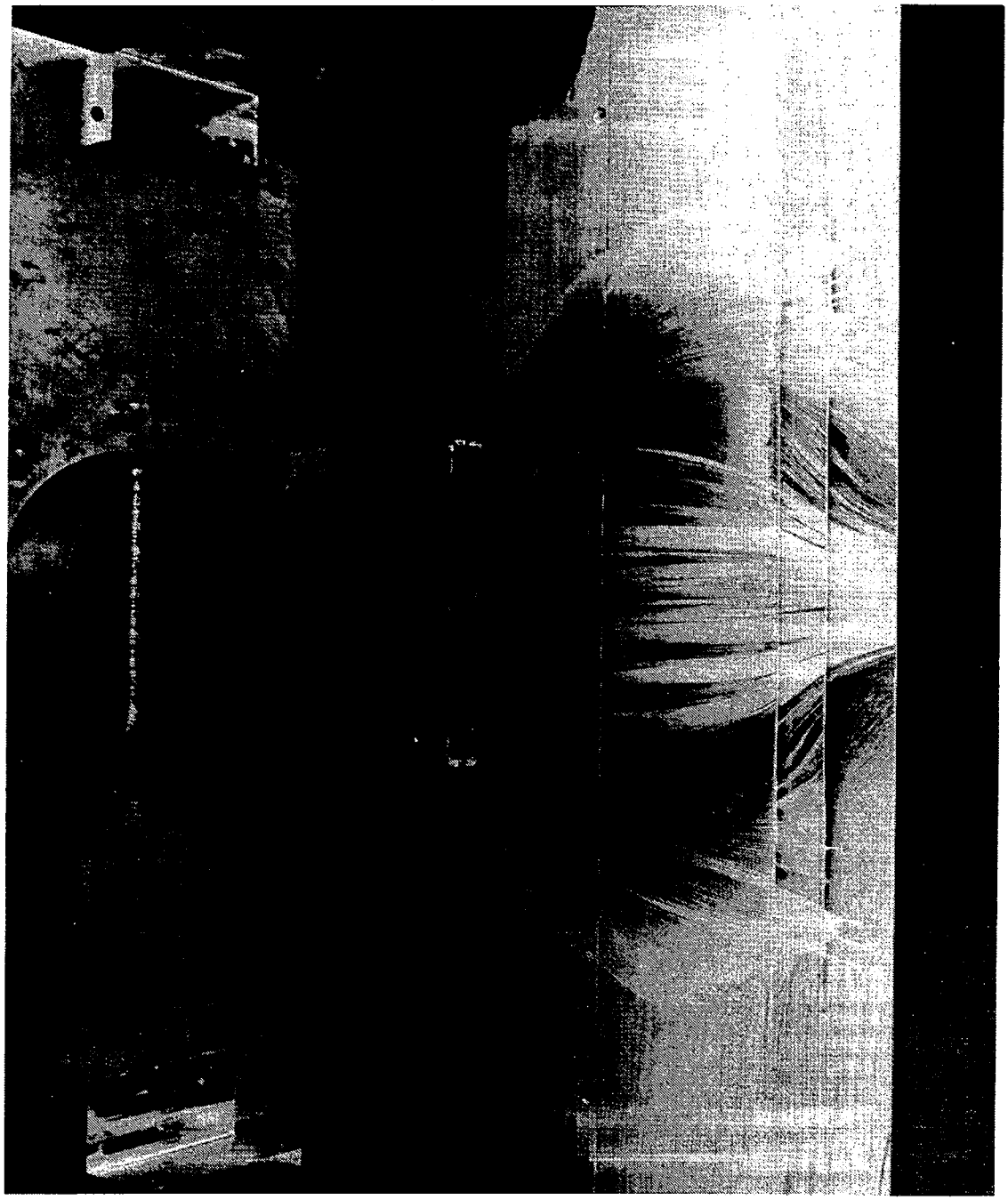

FIGURE 47. SURFACE FLOW PATTERN OF USB (OIL FLOW VISUALIZATION)

AR_N = 8

R_c = 7.62 cm

L_F = 21.77 cm

both just upstream and downstream of the trailing edge. Close to the surface, however, the turbulence associated with the large velocity gradient just downstream of the trailing edge is very large compared to that of the upstream. Thus, it may be inferred that large turbulence intensities are generated in the highly sheared layer of the trailing edge wake. The turbulence shown for large values of z are generated upstream and convected by the mean flow.

Space-Time Correlations. Two-point, space-time correlations of fluctuating velocities were measured in the trailing edge wake using two single hot-wire probes with a two-channel system.

Figure 48 shows the auto-correlation function of the fluctuating velocities measured at three axial locations, $x = 0.3$, 1.59, and 2.54 cm along the line, $y = 0$ (mid-span) and $z = 0.4$ cm. The maximum flow velocity in this region is 74.4 m/sec. The rate of decay of the auto-correlation function is very similar in all the three locations. This auto-correlation function indicates that the turbulence characteristics are broadband with an approximate peak frequency of about 625 Hz. Figure 45 shows the streamwise space-time correlation function (for different separation distances for a fixed wire position at $x_o = 1.59$ cm, $y_o = 0$, $z_o = 0.4$ cm. As the separation distance increased, the peak value of the correlation function reduced and the delay time for the peak correlation increased. The spanwise and lateral space-time correlation functions obtained for one fixed hot-wire position are shown in figures 49 and 50. Several important turbulence characteristics such as eddy convection velocity, longitudinal, spanwise, and lateral turbulence scales are deduced from these correlation measurements as discussed below.

Convection Velocity. The convection velocity, U_c, characterizes the gross motion of turbulence in the downstream direction. A signal of fluctuating velocity sensed at one measurement position is received at a second position, distance x_1, downstream of the first position at a time τ_1 later. For a frozen pattern, therefore, the convection velocity is defined as $U_c = x_1/\tau_1$ or $U_c = x_1/\tau$ at $\partial R(x_1,\tau)/\partial\tau = 0$, where x_1 and τ_1 are fixed separation and time delay, respectively, and x,τ are corresponding variable quantities.

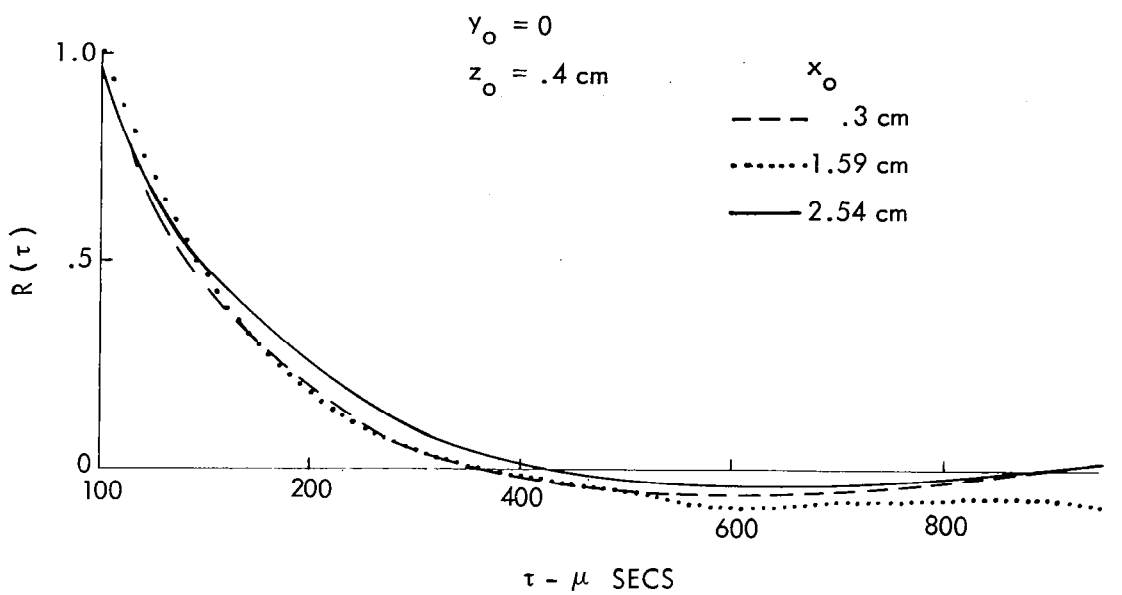

FIGURE 48. AUTO CORRELATION FUNCTION OF FLUCTUATING VELOCITIES

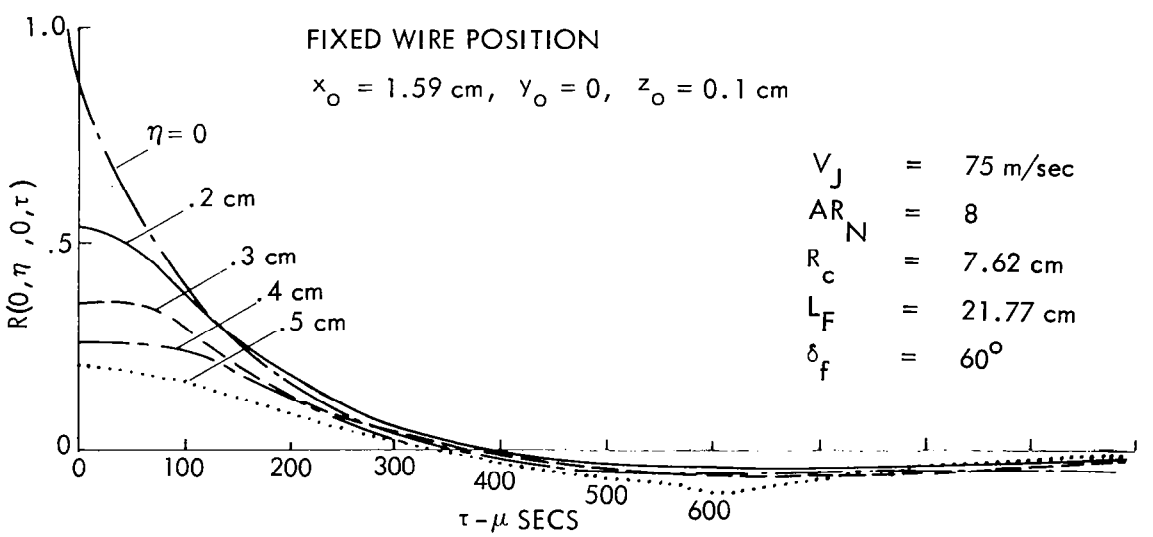

FIGURE 49. SPANWISE SPACE - TIME CORRELATION FUNCTION

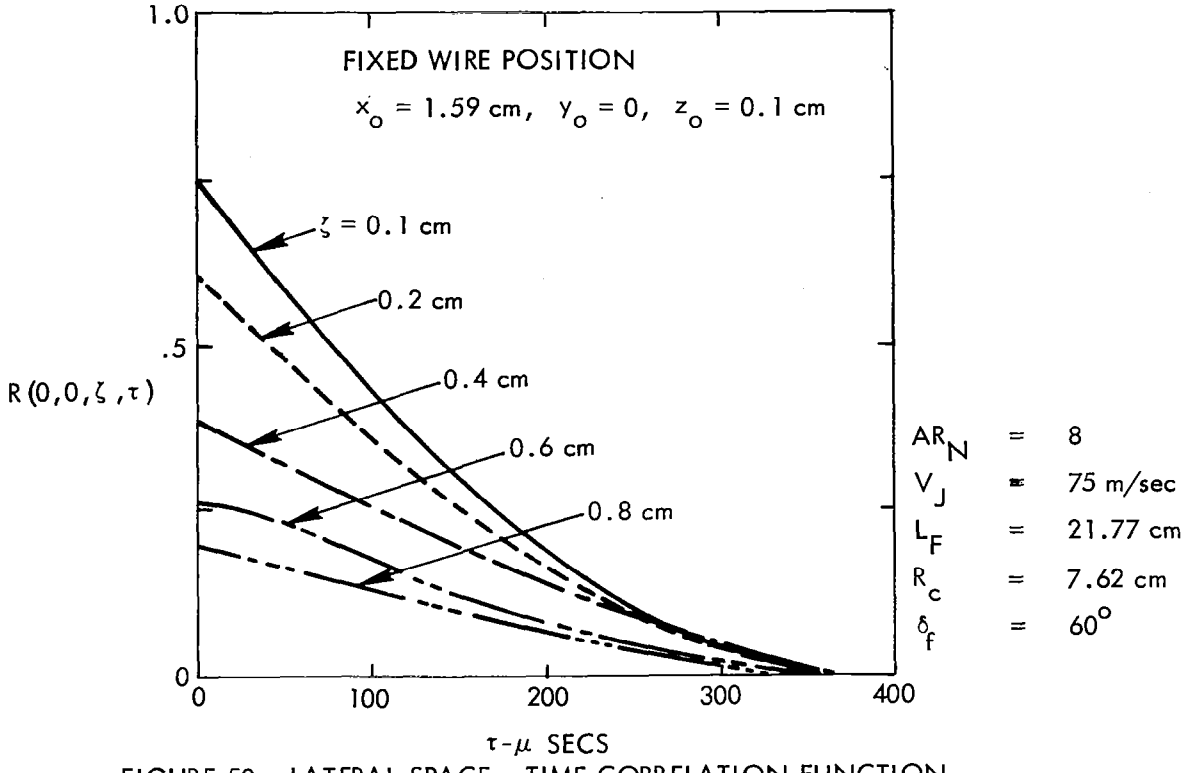

FIGURE 50. LATERAL SPACE - TIME CORRELATION FUNCTION

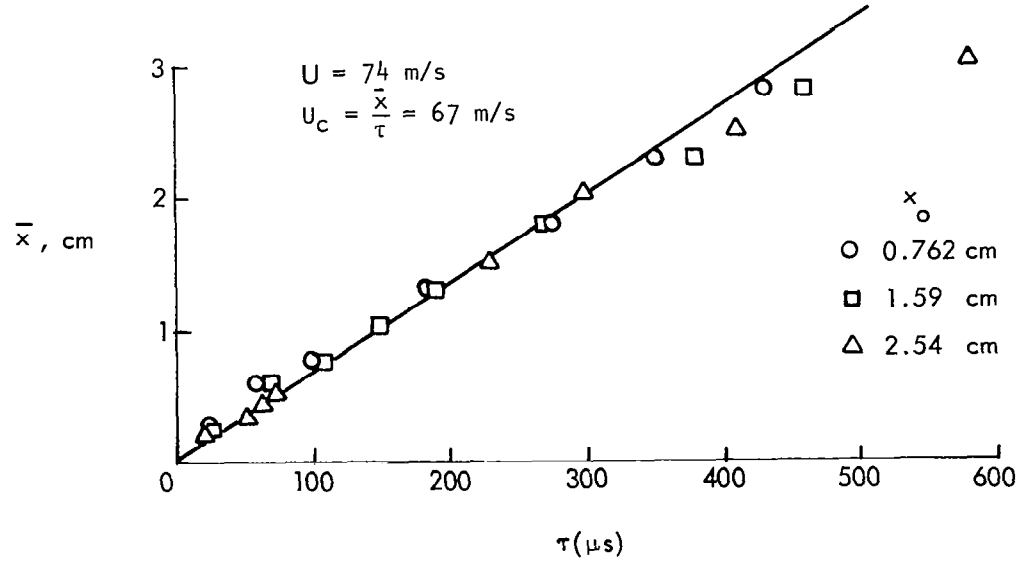

FIGURE 51. DETERMINATION OF CONVECTION VELOCITY

Here the convection velocity is determined by plotting hot-wire separation distances, ξ, against time delay for peak values of correlation function, $R(\xi,0,0,\tau)$ as shown in figure 51 for three fixed hot-wire positions in the trailing edge wake. The convection velocity is given by the slope of the straight line. Here U_c is 67 m/sec, while the maximum mean flow velocity U is found to be 74.4 m/sec. This yields $U_c = 0.9\ U$, which is slightly higher than typical values measured in the shear layer of round jets (e.g. refs. 44 and 45).

Streamwise, Spanwise, and Lateral Length Scales. Figure 52 shows the space correlations $R(\xi,0,0,0)$, $R(0,\eta,0,0)$, and $R(0,0,\zeta,0)$ of velocity fluctuations at zero time delay in the x, y, and z directions, respectively. The fixed wire for these measurements was located at $x_o = 1.59$ cm, $y_o = 0$, and $z_o = 0.2$ cm. These correlations provide a measure of the size of turbulent eddies (or coherent region). The length scales in the streamwise (L_ξ), spanwise (L_η), and lateral (L_ζ) directions are usually defined as

$$L_\xi = \int_0^\infty R(\xi,0,0,0)\ d\xi$$

$$L_\eta = \int_0^\infty R(0,\eta,0,0)\ d\eta$$

$$L_\zeta = \int_0^\infty R(0,0,\zeta,0)\ d\zeta$$

The scale of anisotropy is defined as the ratio of streamwise to spanwise length scales. From Figure 52 it is found that $L_\xi = 0.84$ cm and $L_\eta = L_\zeta = 0.366$ cm. This gives a scale of anisotropy, $\beta = L_\xi/L_\eta = 2.3$. This value is comparable to that measured in the initial mixing layer of turbulent jets (see refs. 44 and 45).

Longitudinal Decay Rate. A turbulent eddy will lose its coherence after traveling a certain distance downstream. This characteristic length can be

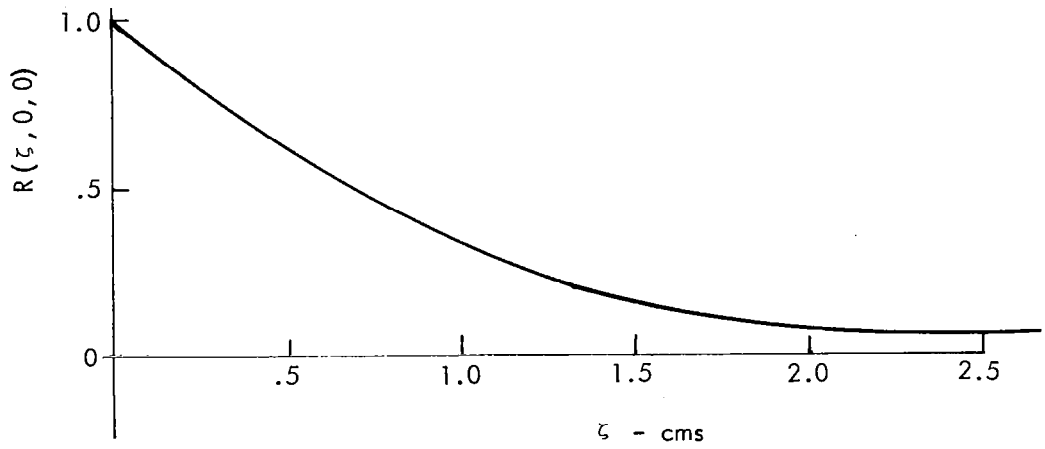

(a) LONGITUDINAL CORRELATION

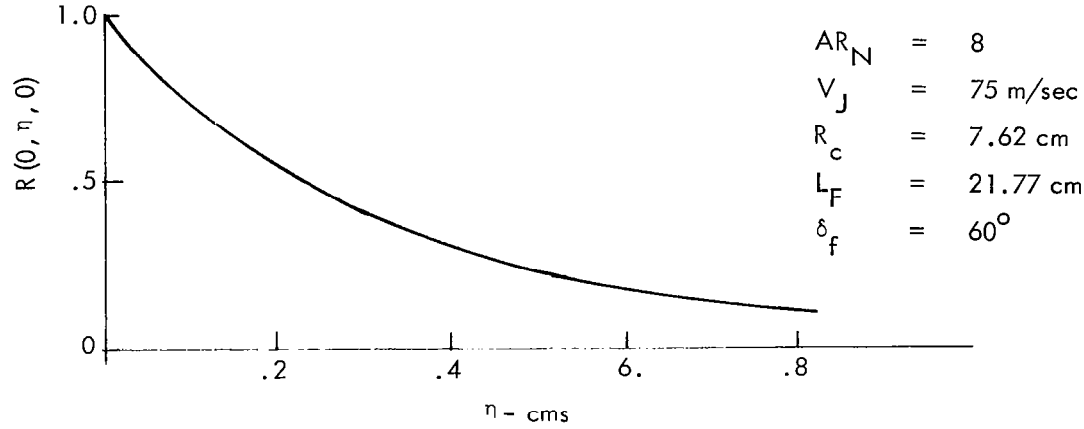

(b) SPANWISE CORRELATION

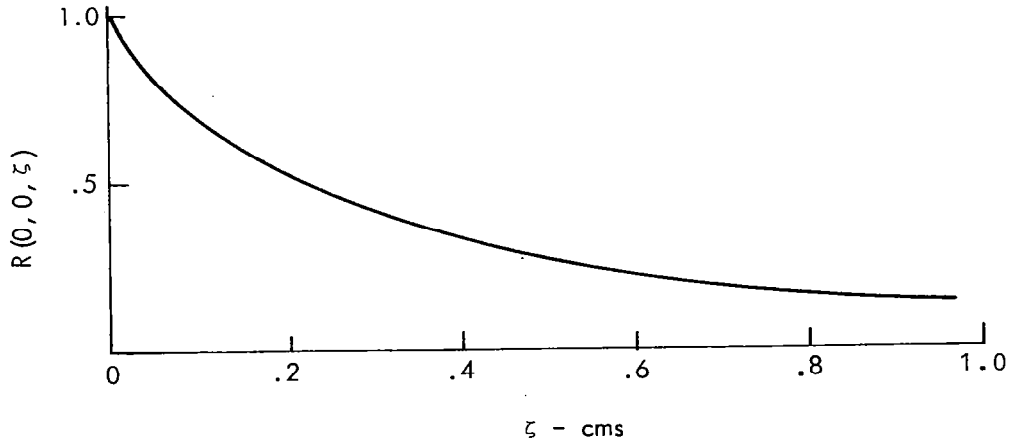

(c) LATERAL CORRELATIONS

FIGURE 52. SPACE CORRELATION FUNCTIONS IN THE TRAILING EDGE WAKE

estimated from the spatial envelope of the space-time correlation function. Figure 53 is a plot of the maximum value of the space-time correlation as a function of the streamwise separation distance and the curve $R(\xi) = \exp(-\xi/.848)$ which approximates the experimental data very well. By means of this fitted curve, the longitudinal decay rate of the space-time correlation function, λ, is found to be $2.848/\delta'$, where δ' is the characteristic thickness of the shear layer in centimeters. It should be noted that the traditional term "decay rate" is used here for convenience; actually in free shear flow a turbulent eddy does not necessarily decay, but it simply loses coherence.

Derivation of Correlation Function. As discussed in the previous section, the correlation function may be approximated using equation (12). By using $G(z')$ to be unity in equations (13) and (14), the auto-correlation function and power spectra of turbulence can be written as

$$R(0,0,z',\tau) = \sum_{i=1}^{n} \frac{\alpha_i A_i}{\alpha_i^2 + \left(\frac{U\tau}{\delta'}\right)^2} \Big/ \sum_{i=1}^{n} \frac{A_i}{\alpha_i} \tag{21}$$

$$P(\omega) = \frac{\delta'}{2U} \frac{\sum_{i=1}^{n} A_i \, e^{-\alpha_i \frac{\omega\delta'}{U}}}{\sum_{i=1}^{n} \alpha_i A_i} \tag{22}$$

The constants α_i and A_i can be determined empirically using either measured auto-correlation or measured powered spectrum of the turbulence in the sheared layer. Use of the auto-correlation function is a little more tedious than the use of power spectra. But the power spectra were not measured in this program, and therefore equation (21) is fitted to the measured auto-correlation function in determining these constants. It is assumed that $n = 3$ will give sufficient accuracy as indicated in reference 39.

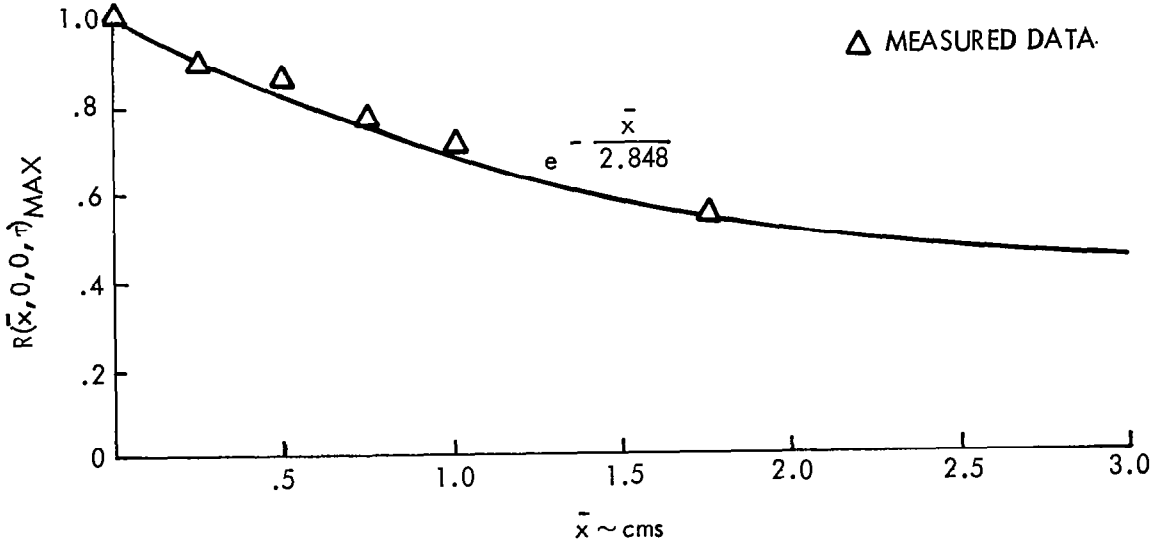

FIGURE 53. SPATIAL ENVELOPE OF THE SPACE-TIME CROSS CORRELATION FUNCTION

The measured auto-correlation function in the trailing edge wake is shown in figure 34. The following values of α_i and A_i were found using equation (21):

$$A_1 = 0.7 \qquad A_2 = 6.3 \qquad A_3 = 3.0$$

$$\alpha_1 = 0.32 \qquad \alpha_2 = 1.4 \qquad \alpha_3 = 20.0$$

It may be seen in figure 54 that equation (21) with these constants approximate the measured curve reasonably well except for large values of delay time τ. This model for turbulence could be improved by obtaining further detailed flow measurements in the trailing edge wake.

The trailing edge wake flow properties determined in this section are used in calculating far-field sound. These calculated values are compared with the experimental results in the next section.

5.3 Experimental Verification of Trailing Edge Wake Noise

USB far-field sound was measured in the anechoic room as described in Section 2 and reference 1. One-third octave band spectra were measured in various directions. The results in two planes, the x-z plane and the plane inclined at an angle of 60° to the x-z plane passing through the jet axis, were used. Measured spectra in various directions and the directivity of sound at a given frequency were compared with the calculated values. The noise levels were calculated using equation (20) and the measured turbulence characteristics in the trailing edge wake.

Noise in Fly-Over Plane. In order to compare the theoretical results developed in Section 5.1 with the measured data, it is convenient to rewrite equation (20) into the following form exhibiting only the dependence on frequency ω, and the directivity angle, ψ.

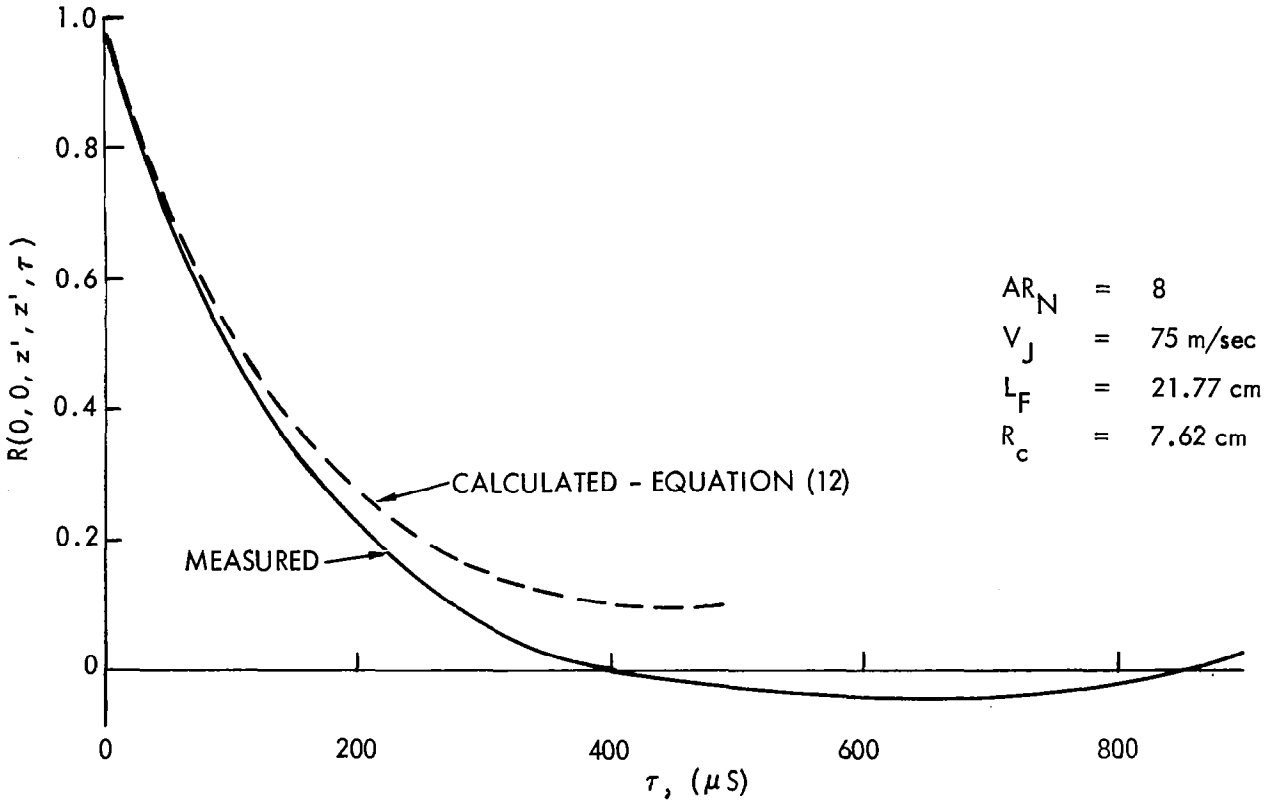

FIGURE 54. AUTOCORRELATION FUNCTION OF FLUCTUATING VELOCITIES

$$D(\psi,\omega) = C\,\omega^2 \sin\psi \frac{\sum_{i=1}^{3} A_i \alpha_i \delta K_o \left(\frac{\alpha_i \delta \omega}{U}\right)}{(\lambda\delta)^{-2} + \left(\frac{\omega}{U}\right)^2 \left(M\cos\psi - \frac{U}{U_c}\right)^2} \tag{23}$$

where $$C = \frac{\rho\, U_c}{2\pi^2\, U^2 a^3 \beta\lambda \sum_{i=1}^{3} \frac{A_i}{\alpha_i}} \iint_{\delta}^{o} \frac{d\bar{u}}{dz'} \frac{d\bar{u}}{dz'} G(z',z'')\, dz',\, dz''$$

C is independent of direction, ψ, and frequency, ω. The unknowns in equation (23), A_i, $\alpha_i\delta$, and U_c/U which describe the flow characteristics in the trailing edge wake are determined from the measured turbulence as described in Section 52. They are:

$A_1 = 0.7$	$A_2 = 6.3$	$A_3 = 3.0$
$\alpha_1\delta = 0.256$ cm	$\alpha_2\delta = 1.12$ cm	$\alpha_3\delta = 16.0$
$U_c/U = 0.9$	$\lambda\delta = 2.84$ cm	

These values can be used in equation (23), and the only unknown is C. Thus, once the value of C is chosen from the experimental data, the sound pressure in any direction and at any frequency can be determined. One-third octave band power spectra calculated from equation (23) in the x-z plane are compared with the measured data in figure 55 in various directions. The directivity pattern of one-third octave band sound pressure levels at center frequencies of 400, 1600, and 6300 Hz in the x-z plane are shown in figure 56. These figures show very favorable agreement over most of the measured frequencies in all the measured directions. The agreement between theory and experiment is best in the middle frequency range (bearing in mind the effect of reflection and refraction from the test rig). In the high frequency range, the measured data are slightly higher than the predicted values, probably because of the contribution of jet noise which is neglected in the theory. On the other hand, in the low frequency range (less than 400 Hz), the theory consistently predicts somewhat higher values. The reason for this

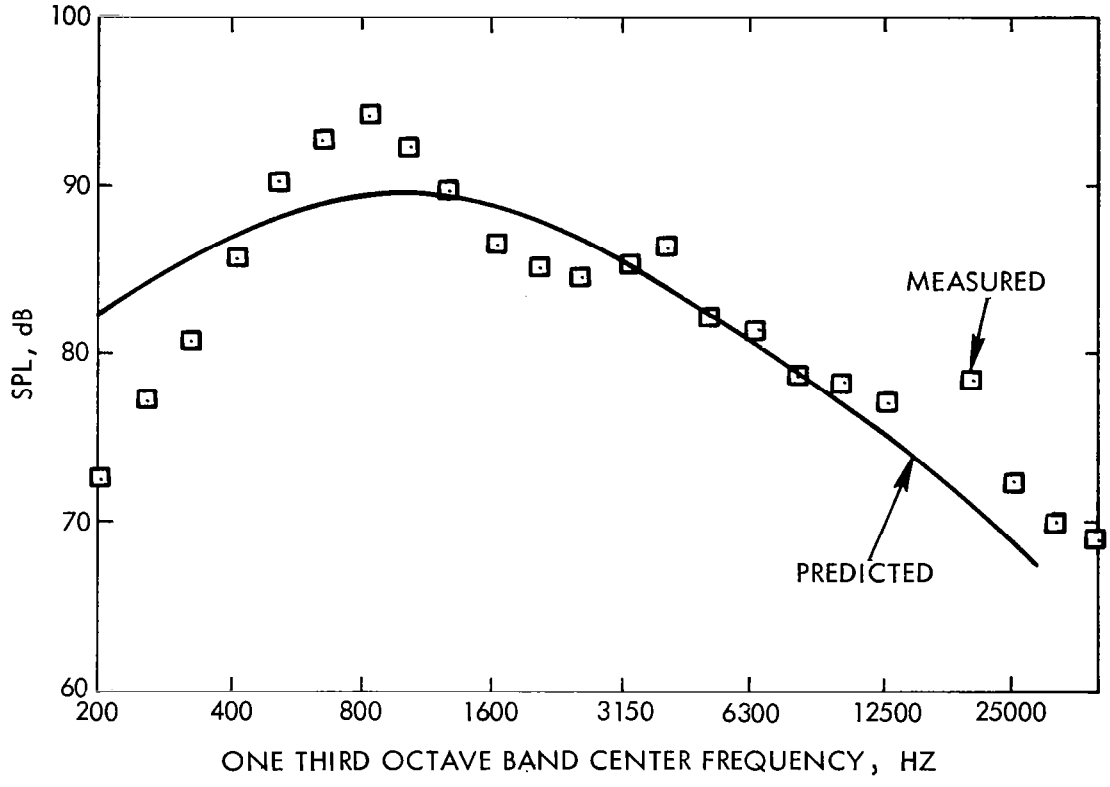

(a) $\psi = 86°$

FIGURE 55. COMPARISON OF MEASURED SPECTRA WITH THE THEORETICAL PREDICTION IN THE x-z PLANE (U = 103 m/s, $\phi = 90^{\circ}$)

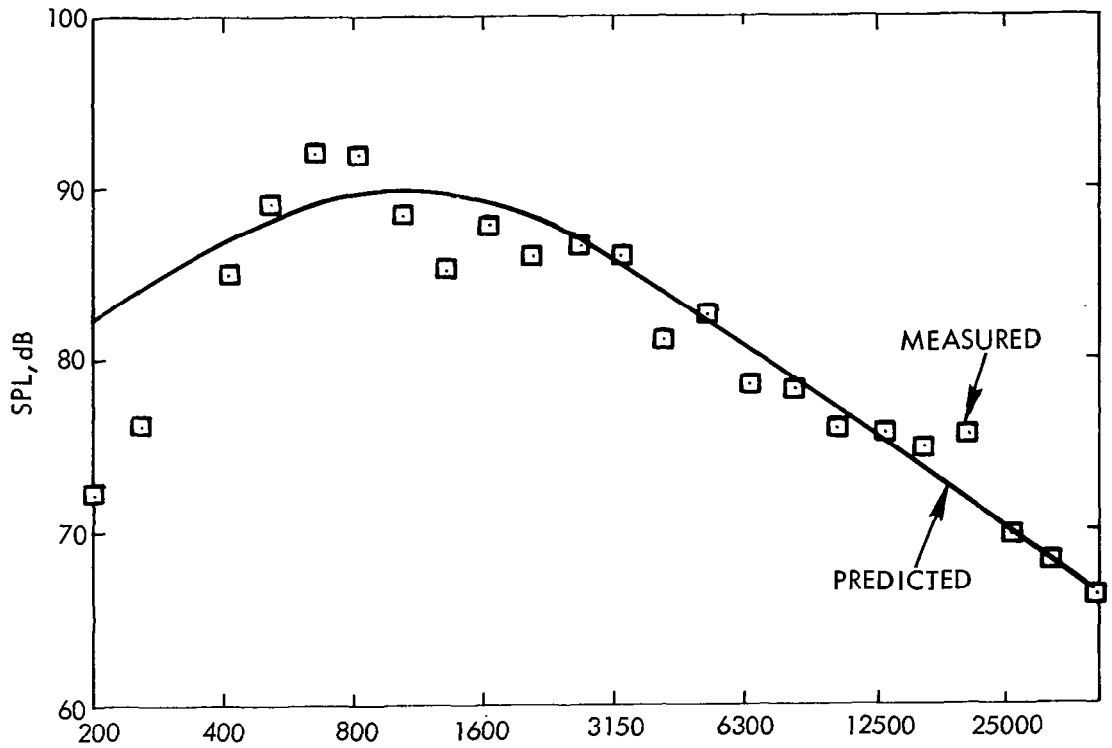

(b) $\psi = 70°$

FIGURE 55. (CONTINUED)

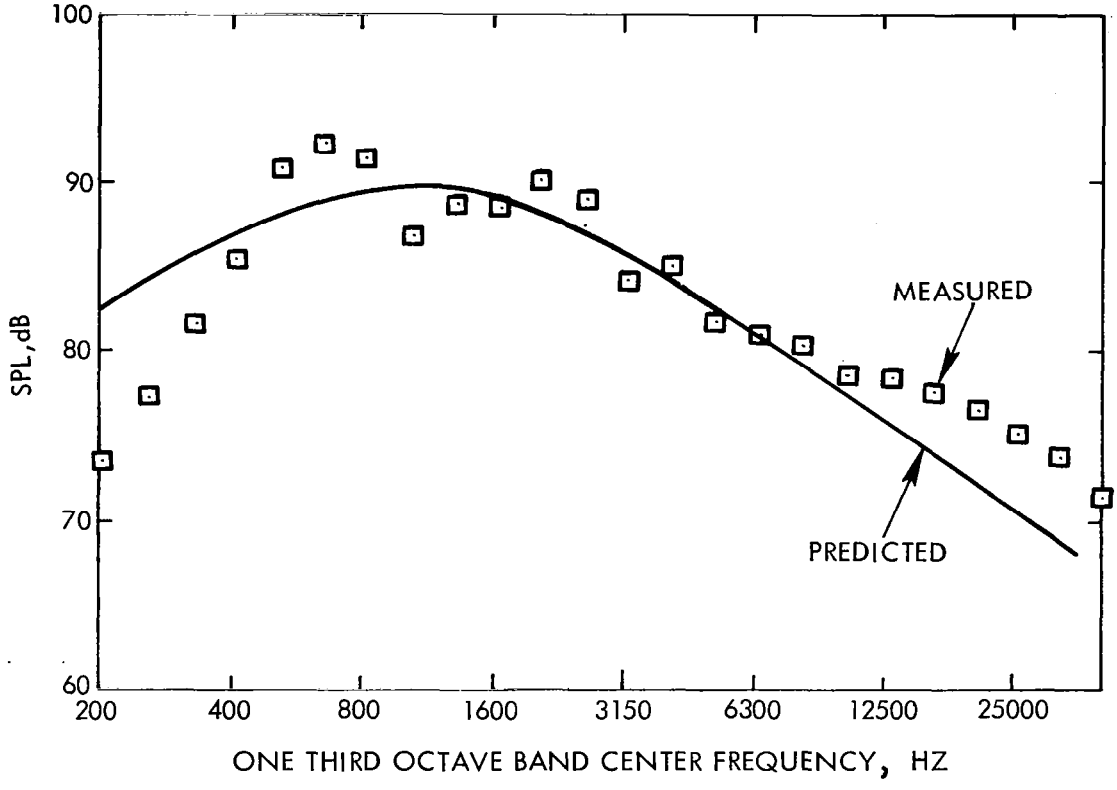

(c) ψ = 64°

FIGURE 55. (CONTINUED)

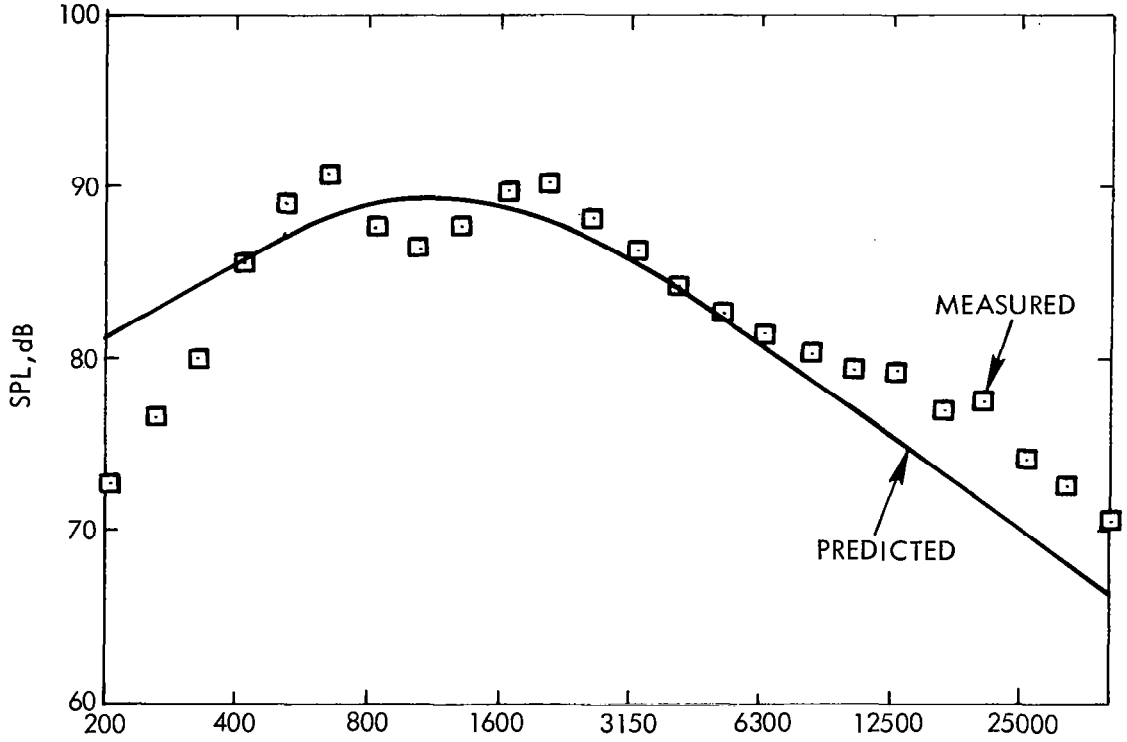

(d) $\psi = 41°$

FIGURE 55. (CONTINUED)

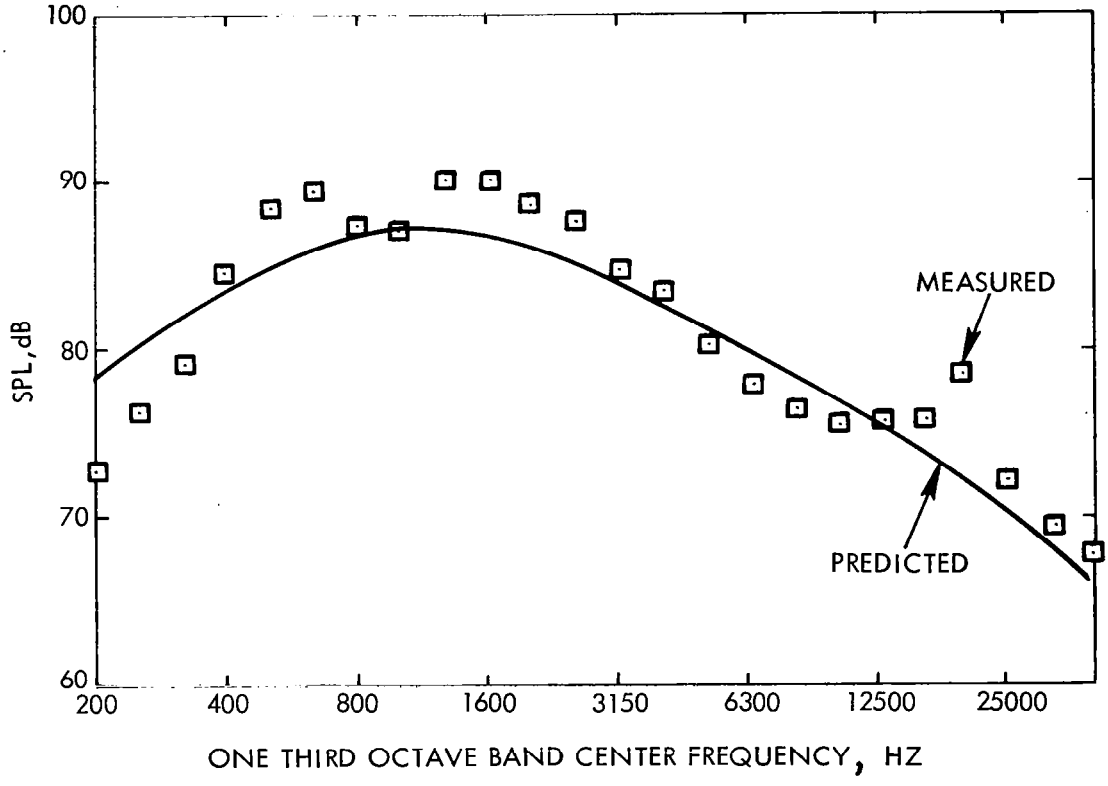

(e) $\psi = 24°$

FIGURE 55. (CONTINUED)

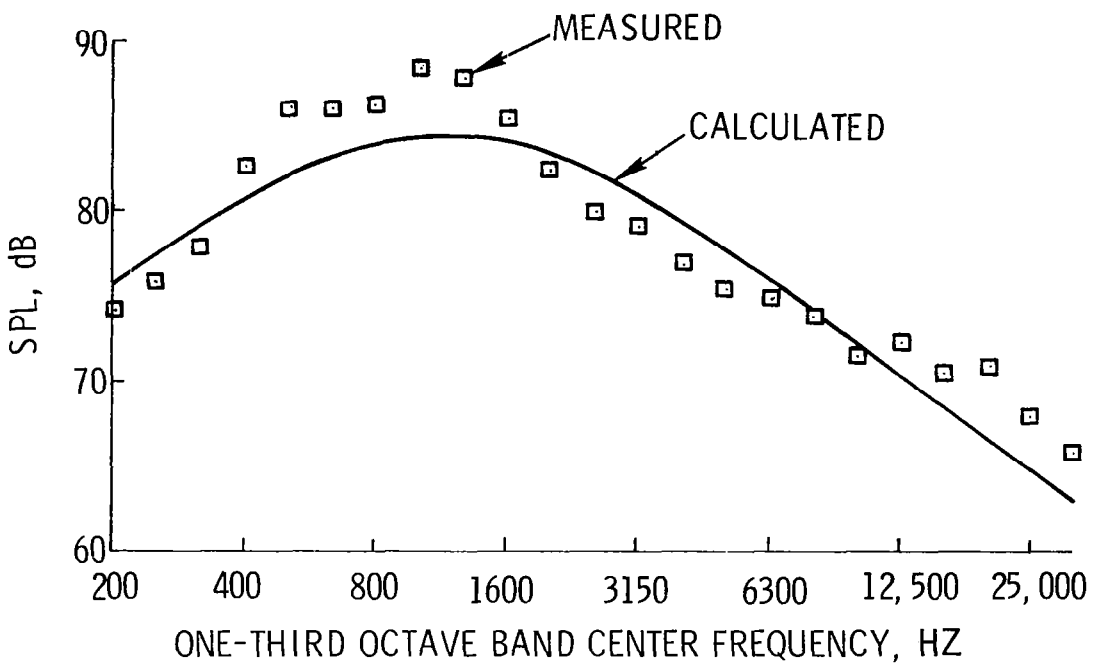

(f) $\psi = 10°$

FIGURE 55. (CONCLUDED)

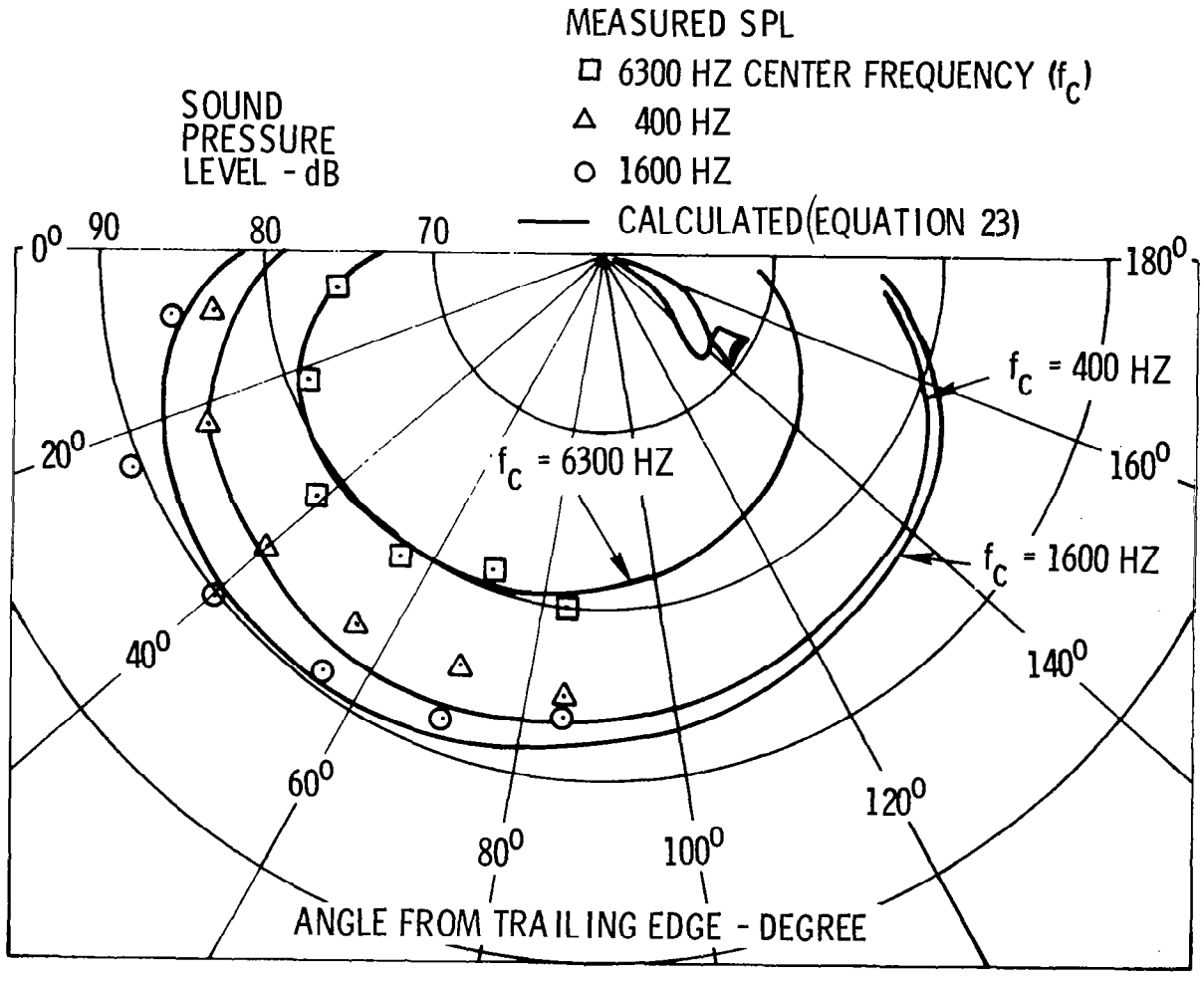

FIGURE 56. COMPARISON BETWEEN CALCULATED AND MEASURED SOUND

can be traced to the fitted curve of the correlation function in figure 54. The empirical curve does not approximate the true auto-correlation function very well for large delay times. More low frequency components than are actually present are included in the prediction of far-field noise. The experimentally observed dual peaks (which is not predicted by theory) may be due to multi-source contribution in addition to scattering problems. However, considering the simplicity of the theoretical model, it is deemed that the agreement is perhaps as good as could be expected.

Noise in Other Planes:

The sound intensity in any other plane containing x-axis and inclined at an angle ϕ to the x-z plane may be derived similarly. Relation between the directivity function, $D(\psi,\phi,\omega)$ and the correlation function of turbulence, $\tilde{R}$, is derived as given in reference 43.

$$D(\psi,\phi,\omega) = \frac{1}{\rho a}\tilde{R}\left(\frac{\omega}{a}\cos\psi,\ \frac{\omega}{a}\sqrt{1-\cos^2\phi\sin^2\psi-\cos^2\psi},\omega\right)\cdot\frac{\omega^2}{a^2}\sin\psi\cos\phi \qquad (24)$$

Substitution of equation (19) in (24) with the assumption of approximating the factor, $k_x^2/(k_x^2+k_y^2)$, to be unity leads to

$$D(\psi,\phi,\omega) = \frac{\rho U_c U^2}{a^3 2\pi^2\beta\lambda}\cdot\omega^2\sin\psi\cos\phi$$

$$\cdot\frac{\sum_{i=1}^{3} A_i\alpha_i K_o\left[\frac{\alpha_i\delta'\omega}{U}\sqrt{1+\frac{U_c}{U}^2\frac{M^2}{\beta^2}(1-\cos^2\phi\sin\psi-\cos^2\psi)}\right]}{\sum_{i=1}^{3} A_i\alpha_i\left[(\lambda'\delta)^{-2}+\left(\frac{\omega}{U}\right)^2\left(M\cos\psi-\frac{U}{U_c}\right)^2\right]}$$

$$\cdot\int_{-\delta}^{o}\int\frac{d\bar{u}}{dz'}\frac{d\bar{u}}{dz''}\cdot G(z',z'')\,dz'\,dz''$$

This equation may be written in the following simplified form to exhibit as a function of only ω, ψ, and ϕ.

$$D(\psi,\phi,\omega) = C\ \omega^2 \sin\psi\ \cos\phi$$

$$\cdot \frac{\sum_{i=1}^{3} A_i \alpha_i \delta' K_o \left[\frac{\alpha_i \delta' \omega}{U} \sqrt{1 + \left(\frac{U_c}{U}\right)^2 \frac{M^2}{\beta^2} (1 - \cos^2\phi\ \sin^2\psi - \cos^2\psi)} \right]}{(\lambda\delta')^{-2} + \left(\frac{\omega}{U}\right)^2 \left(M \cos\psi - \frac{U}{U_c}\right)^2} \qquad (25)$$

The value of C in (25) is the same as in equation (23). Figure 57 shows the comparison of calculated one-third octave band spectra using equation (25) with the measured data in the plane $\phi = 60°$ at angles $\psi = 86°$, 70°, and 64°. In these calculations, $\beta = 2.3$ is used. The agreement between the theoretical values and the measured data is very good in this plane also.

This analysis is developed for the noise generated by the turbulent flow mixing downstream of the trailing edge of a practical upper surface blown flap. The sound field radiated in the direction below the wing is primarily a function of the flow parameters in the trailing edge wake. The flow properties used were derived from the experimentally measured turbulence and mean flow characteristics. Thus, in order to evaluate the effect of geometric and operational parameters of the USB configuration on noise characteristics, it is necessary to know the relationship between the flow parameters in the trailing edge wake and the various geometric and operational parameters. But to do so would require either analytical and/or extensive experimental measurements which are not available at the present time. Therefore, this theory should be treated as a first step in developing a theoretical model to predict the high-lift noise for USB systems.

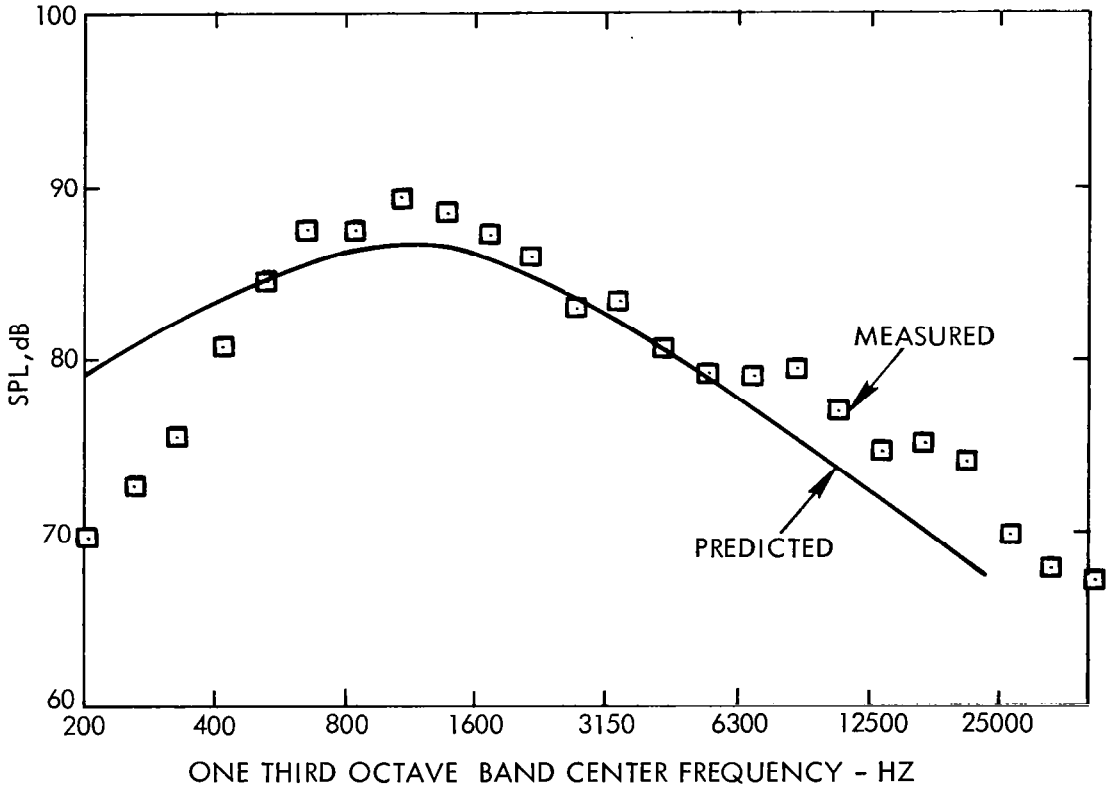

(a) $\psi = 86°$

FIGURE 57. COMPARISON OF MEASURED SPECTRA WITH THE THEORETICAL PREDICTION ($U = 103$ m/s, $\phi = 30°$.)

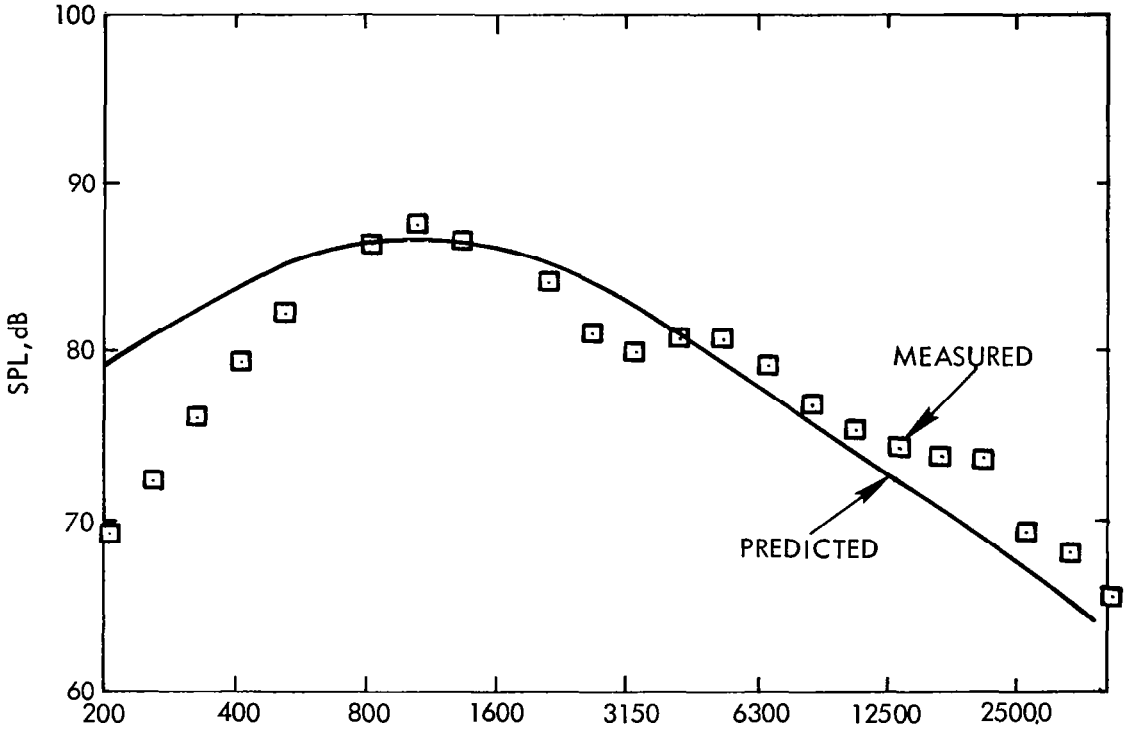

(b) $\psi = 70°$

FIGURE 57. (CONTINUED)

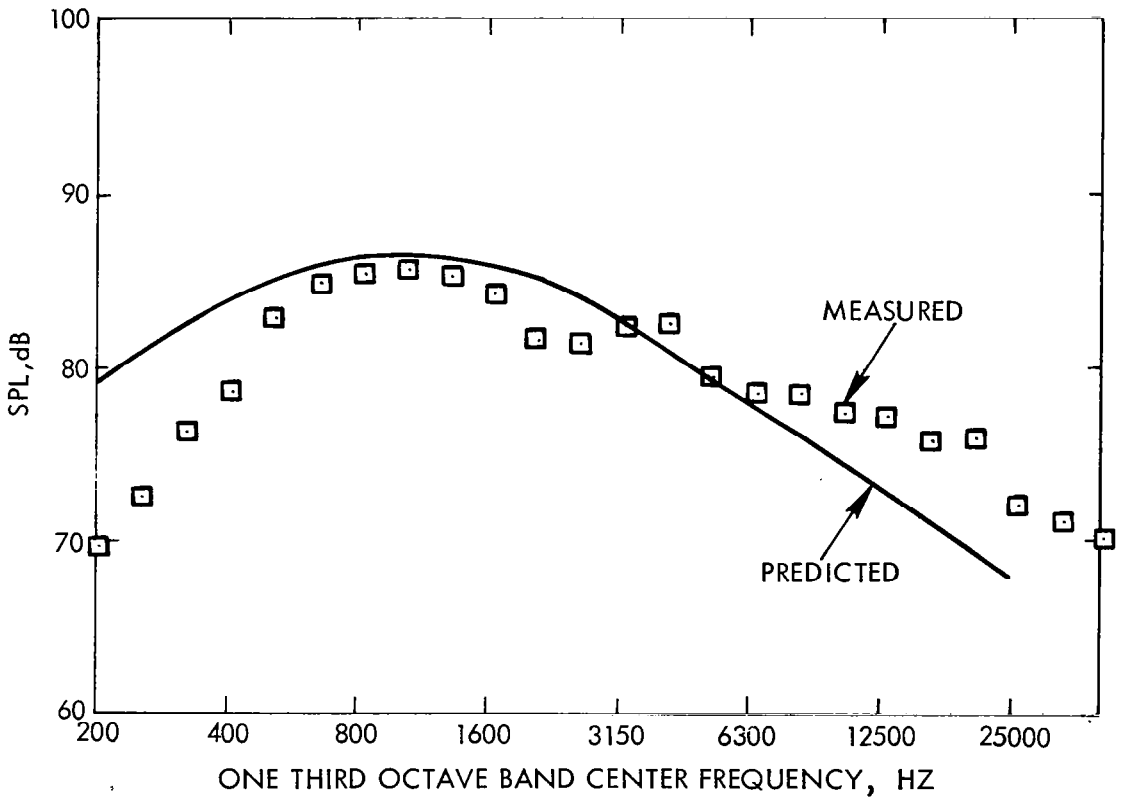

(c) $\psi = 61°$

FIGURE 57. (CONCLUDED)

6. CONCLUSIONS

The main conclusions from the analysis of noise and flow characteristics, the development of the noise prediction model, the compatible studies, and the development of a theory for USB trailing edge noise are as follows:

(1) For a practical upper surface blown flap configuration, the turbulent mixing just downstream of the trailing edge is the dominant noise source from the community noise point of view.

(2) The far-field sound of USB is primarily a function of the flow parameters in the trailing edge wake.

(3) One of the ways of reducing USB noise is to modify the shear layer downstream. Accomplishment of the noise reduction for a practical USB configuration requires a more systematic experimental and theoretical study.

(4) The compatibility study indicates that by incorporating a jet exhaust nozzle with an aspect ratio of 4 or 6 and an extended flap, a USB aircraft can have a 90 EPNdB footprint area as amall as 1.2 km^2. This design is compatible with aero-propulsion performance requirements.

(5) A theoretical model was developed for the noise generated and propagated from a shear layer which is typical of USB trailing edge. The theoretical results were compared favorably with the measured data for a particular configuration. These calculations provides some understanding of basic noise generation of one of the dominant noise sources of the USB configuration.

This page intentionally left blank.

APPENDIX

APU	auxiliary power unit
A, A_i (i=1,2...)	empirical constants to fit the auto-correlation function of fluctuating velocities
A_N	nozzle exit area, m^2 (ft^2)
A_o	nozzle exit reference area, m^2 (ft^2)
AR_N	nozzle aspect ratio = W_N^2/A_N
a	ambient speed of sound, m/sec (ft/sec)
C	see equation (23)
C_D	total drag coefficient
ΔC_{DN}	nacelle drag increment coefficient
$\Delta C_{D_{NIT}}$, ΔC_D	total nacelle interference drag coefficient increment
C_L	total lift coefficient
C_{L_A}	aerodynamic lift coefficient
C_μ	gross thrust coefficient
c	wing chord, m (ft)
DOC	direct operating cost, ¢/seat-S.M.
$D(\psi,\omega)$	directivity function of radiated sound in x-y plane
D_n	nozzle exit diameter, m (ft)
EPNdB	effective perceived noise level, dB
F_N	net thrust, N (lbs)
F_s	frequency shift parameter
f	frequency, Hz
f_c	one-third octave band center frequency, Hz
$G(z',z'')$	lateral space correlation function of fluctuating velocities at zero time delay

H	jet total pressure, N/m^2 (lbs/in^2)
K	constant (equation 1)
$K_o(\ )$	modified Bessel function of zeroth order
k_x, k_x', k_y, k_y'	Fourier transform variables of x,x',y and y'
$k_\perp$	$\sqrt{k_x^2 + k_y^2}$
L_f	flow length (length on the surface from the nozzle exit to the trailing edge), m (ft)
L_s	effective length of the shear layer in the trailing edge wake, m (ft)
L_{TE}	length of the straight portion of the trailing edge, m (ft)
L_ξ, L_η, L_ζ	longitudinal (x), lateral (y), and transverse (z) length scales of turbulence, m (ft)
L/D	lift-to-drag ratio
M	flow Mach number based on ambient speed of sound
M_o	aircraft cruise Mach number
n	velocity exponent of radiated sound
OASPL	overall sound pressure level, dB
OTW	over-the-wing (nacelle)
$P(x,\omega)$	acoustic power spectra per unit solid angle, N^2/radian/unit solid angle/unit area
PNL	perceived noise level, dB
PNLT	tone corrected PNL
P_o	freestream static pressure, N/m^2 (lbs/in^2)
p	turbulent fluctuating pressure, N/m^2 (lbs/in^2)
$\tilde{p}$	Fourier transform of p
$\bar{p}$	mean square value of acoustic pressure, $N^2/m4$ ($lbs^2/in4$)
R	distance of the noise measurement location from aircraft of experimental model, m (ft)

R_c	flap knee radius of curvature, m (ft)
R_o	reference distance to calculate the radiated noise, m (ft)
$R(\ )$	space-time correlation function of turbulence
$R_p(\ )$	correlation function of fluctuating pressures
$R_T(\ )$	correlation function of fluctuating velocity term, T
$R_w(\ )$	correlation function of fluctuating velocity component, W
$\tilde{R},\tilde{R}_p,\tilde{R}_T,\tilde{R}_w$	Fourier transforms of correlation functions
S	Strouhal number, $\omega\delta'/U$
SPL	sound pressure level, dB
S.M.	statute mile
$T(\ )$	description of fluctuating velocities (equations 2)
$\tilde{T}$	Fourier transform of T
U	typical velocity, m/sec (ft/sec)
U_c	eddy convection velocity, m/sec (ft/sec)
u,v,w	longitudinal, lateral and transverse components of fluctuating velocities, m/sec (ft/δ_a)
$\bar{u},\bar{v},\bar{w}$	longitudinal, lateral and transverse components of mean velocities, m/sec (ft/sec)
$u_i(i=1,2,3)$	fluctuating velocity components in x,y,z directions (same as u,v,w)
V	integration volume, m^3 (ft^3)
V_j	jet exit velocity, m/sec (ft/sec)
V_o	reference velocity to calculate the radiated noise, m/sec (ft/sec)
W_N	nozzle exit equivalent width, m (ft)
x,x',x''	longitudinal (streamwise) coordinates
$\bar{x}$	magnitude of hot-wire separation distance in x-direction, cm (in)

x_o	longitudinal location of the fixed hot wire, cm (in)
$X_{N/C}$	chordwise position of the nozzle on the wing, fraction of wing chord
y, y', y''	lateral (spanwise) coordinates
$\bar{y}$	magnitude of hot-wire separation distance in y-direction, cm (in)
y_o	lateral location of the fixed hot wire, cm (in.)
z, z', z''	transverse (vertical) coordinates
Z_N	nozzle transverse (vertical) position, cm (in)
z_o	transverse location of the fixed hot wire, cm (in)
α, $\alpha_i (i=1,2...)$	empirical constants to fit the auto-correlation function of fluctuating velocities
β	scale of anisotropy of turbulence
β'	boattail angle of the nozzle, degrees
$\delta( )$	delta function
δ'	shear layer thickness, m (ft)
δ_f	flap deflection angle, degrees
θ	angle from nozzle forward axis to the observer or microphone location (figure 1), degrees
θ'	angle from the wing chord, forward to the wing, degrees to the observer or microphone location (figure 1), degrees
θ''	ψ - 180° (figure 1), degrees
θ_N	nozzle impingement angle on wing upper surface
λ	longitudinal decay rate of correlation function
ρ	flow density, kg/m^3 ($slugs/ft^3$)
τ	time delay between the two hot-wire signals, secs
ϕ	angle between a plane perpendicular to the wing lateral axis containing the nozzle centerline and any other plane containing the nozzle centerline (see insert in figure 21), degrees

ψ	angle between a line tangent to the flap trailing edge in a plane perpendicular to the wing lateral axis and a line from the aircraft or model to the observer location (figure 1), degrees
Ω	solid angle, degrees
ω	frequency, radians/sec.

This page intentionally left blank.

REFERENCES

1. Brown, W. H.; et al.: Noise Characteristics of Upper Surface Blown Configurations - Experimental Program and Results, NASA CR-145143, 1977.

2. Jones, W. L.; Heidelberg, L. J.; and Goldman, R. G.: Highly Noise Suppressed Bypass 6 Engine for STOL Applications. AIAA Paper 73-1031. Nov. 1973.

3. Samanich, N. E.; Heidelberg, L. J.; and Jones, W. L.: Effect of Exhaust Nozzle Configuration on Aerodynamic and Acoustic Performance of an Externally Blown Flap System with a Quiet 6:1 Bypass Ratio Engine. AIAA Paper 73-1217. Nov. 1973.

4. Dorsch, R. G.; and Reshotko, M.: EBF Noise Tests with Engine Under and Over the Wing Configurations. *STOL Technology*, Washington, D. C., 1973.

5. Dorsch, R. G.; Dreim, W. J.; and Olsen, W. A.: Externally Blown Flap Noise. AIAA Paper 72-129. Jan. 1972.

6. Dorsch, R. G.; Reshotko, M.; and Olsen, W. A.: Flap Noise Measurements for STOL Configurations Using External Upper Surface Blowing. AIAA Paper 72-1203. Nov. 1972.

7. Reshotko, M.; Goodykoontz, J. H.; and Dorsch, R. G.: Engine Over-the-Wing Noise Research. AIAA Paper 73-631. July 1973.

8. Olsen, W. A.; Dorsch, R. G.; and Miles, J. H.: Noise Produced by a Small-Scale Externally Blown Flap. NASA TN D-6636, 1972.

9. Dorsch, R. G.; Lasagna, P. L.; Maglieri, D. J.; and Olsen, W. J.: Flap Noise. *Aircraft Engine Noise Reduction*. NASA SP-311, 1972.

10. Clark, B. J.; Dorsch, R. G.; and Reshotko, M.: Flap Noise Prediction Method for a Powered Lift System. AIAA Paper 73-1028, Oct. 1973.

11. Von Glahn, U.; and Groesbeck, D.: Acoustics of Attached and Partially Attached Flow for Simplified OTW Configurations with 5:1 Slot Nozzle. NASA TM X-71807, 1975.

12. Von Glahn, U.; and Groesbeck, D.: Geometry Effects on STOL Engine-Over-the-Wing Acoustics with 5:1 Slot Nozzles. NASA TM X-71820, 1975.

13. Von Glahn, U.; and Groesbeck, D. E.: Effect of External Jet Flow Deflector Geometry on OTW Aero-Acoustic Characteristics. AIAA Paper 76-499, July 1976.

14. Von Glahn, U.; and Groesbeck, D. E.: OTW Noise Correlation for Variations in Nozzle/Wing Geometry with 5:1 Slot Nozzles. AIAA Paper No. 76-521, July 1976.

15. Reddy, N. N.; and Brown, W. H.: Acoustic Characteristics of an Upper-Surface Blowing Concept of Power-Lift Systems. AIAA Paper 75-204, 1975.

16. Reddy, N. N.; and Yu, J. C.: Radiated Noise from an Externally Blown Flap. NASA TN D-7908, 1975.

17. Reddy, N. N.: Propulsive-Lift Noise on an Upper-Surface Blown Flap Configuration. AIAA Paper 75-470, 1975.

18. Tam, C. K. W.; and Yu, J. C.: Trailing Edge Noise. AIAA Paper 75-489, 1975.

19. Reddy, N. N.; and Gibson, J. S.: Noise Characteristics of Upper Surface Blown Configurations - Summary, NASA CR-2918, 1978.

20. Lilley, G. M.; and Hodgson, T. H.: On Surface Pressure Fluctuations in Turbulent Boundary Layer. AGARD Report No. 276, April 1960.

21. Ffowcs Williams, J. E.; and Hall, L. H.: Aerodynamic Sound Generation by Turbulent Flow in the Vicinity of a Scattering Half Plane. *Journal of Fluid Mechanics*, vol. 40, 1970, pp. 657-670.

22. Powell, A.: On the Aerodynamic Noise of a Rigid Flat Plate Moving at Zero Incidence. *Journal of the Acoustical Society of America*, vol. 31, 1959, pp. 1649-1653.

23. Hayden, R. E.: Noise from Interaction of Flow with Rigid Structures: A Review of Current Status of Prediction Techniques. NASA CR-2126, 1972.

24. Chase, D. M.: Sound Radiated by Turbulent Flow Off a Rigid Half-Plane as Obtained from a Wave Vector Spectrum of Hydrodynamic Pressures. *Journal of the Acoustical Society of America*, vol. 52, 1972, pp. 1011-1023.

25. Chase, D. M.: Noise Radiated from an Edge in Turbulent Flow. *AIAA Journal*, vol. 13, pp. 1041-1047, 1975.

26. Chandiramani, K. L.: Diffraction of Evanescent Waves with Applications to Aerodynamically Scattered Sound and Radiation from Unbaffled Plates. *Journal of the Acoustical Society of America*, vol. 55, 1974, pp. 19-29.

27. Schrecker, G. O.; and Maus, J. R.: Noise Characteristics of Jet Flap Type Exhaust Flows. NASA CR-2342, 1974.

28. Clark, L. R., and Yu, J. C.: Effects of Geometry of Jet Velocity on Noise Associated with an Upper Surface-Blowing Model, NASA TN D-8386, 1977.

29. Heidelberg, L.; Homyak, L.; and Jones, W. L.: Full-Scale Blown Flap Noise." SAE Paper No. 750609, May 1975.

30. Reddy, N. N.; Blakney, D. F.; Tibbetts, J. G.; and Gibson, J. S.: V/STOL Aircraft Noise Prediction (Jet Propulsions), FAA-RD-75-125, June 1975.

31. NASA CR-114612 and 114613. Quiet Turbofan STOL Aircraft for Short-Haul Transportation. Lockheed Aircraft Corporation, June 14, 1973.

32. Higgins, T. T.; Stout, E. G.; and Sweet, H. S.: Study of Quiet Turbofan STOL Aircraft for Short-Haul Transportation. NASA CR-2355, December 1973.

33. NASA CR-137525 and 137526. Evaluation of Advanced Lift Concepts and Fuel-Conservative Short-Haul Aircraft. Lockheed Aircraft Corporation, June 1974.

34. Sweet, H. S.; Renshaw, J. H.; and Bowden, M. K.: Evaluation of Advanced Lift Concepts and Potential Fuel Conservation for Short-Haul Aircraft. NASA CR-2502, September 1974.

35. Braden, J. A.; et al.: Exploratory Studies of the Cruise Performance of Upper Surface Blown Configurations. Lockheed-Georgia Report No. LG77ER0028 (to be published as NASA CR).

36. Hayden, R. E.; Reduction of Noise from Airfoils and Propulsive Lift Systems Using Variable Impedance Systems. AIAA Paper 76-500, July 1976.

37. Kraichnan, R. H.: Field Pressures Within Homogeneous Anisotropic Turbulence. *Journal of the Acoustical Society of America*, vol. 28, 1956, pp. 64-72.

38. Kraichnan, R. H.: Pressure Fluctuations in Turbulent Flow Over a Flat Plate. *Journal of the Acoustical Society of America*, vol. 28, 1956, pp. 378-390.

39. Maestrello, L.: Measurements and Analysis of the Response Field of Turbulent Boundary Layer Excited Panel. *Journal of Sound and Vibration*, vol. 2, 1965, pp. 270-292.

40. Maestrello, L.: Use of Turbulent Model to Calculate the Vibration and Radiation Responses of a Panel with Practical Suggestions for Reducing Sound Level. *Journal of Sound and Vibration*, vol. 5, 1967, pp. 407-448.

41. Lilley, G. M.: On the Noise of Air Jets. Aeronautical Research Council No. 20376, 1958.

42. Panton, R. L.; and Linebarger, J. H.: Wall Pressure Spectra Calculations for Equilibrium Boundary Layers. *Journal of Fluid Mechanics*, vol. 65, pp. 261-287.

43. Tam, C. K. W.: Intensity, Spectrum, and Directivity of Turbulent Boundary Layer Noise. *Journal of the Acoustical Society of America*, vol. 57, 1975, pp. 25-34.

44. Laurence, J. C.: Intensity, Scale and Spectra of Turbulence in Mixing Region of Free Subsonic Jet. NACA Report 1292, 1956.

45. Davies, P.O.A.L.; Fisher, M. J.; and Barrett, M. J.: The Characteristics of Turbulence in Mixing Region of a Round Jet. *Journal of Fluid Mechanics*, vol. 15, 1963, p. 337.